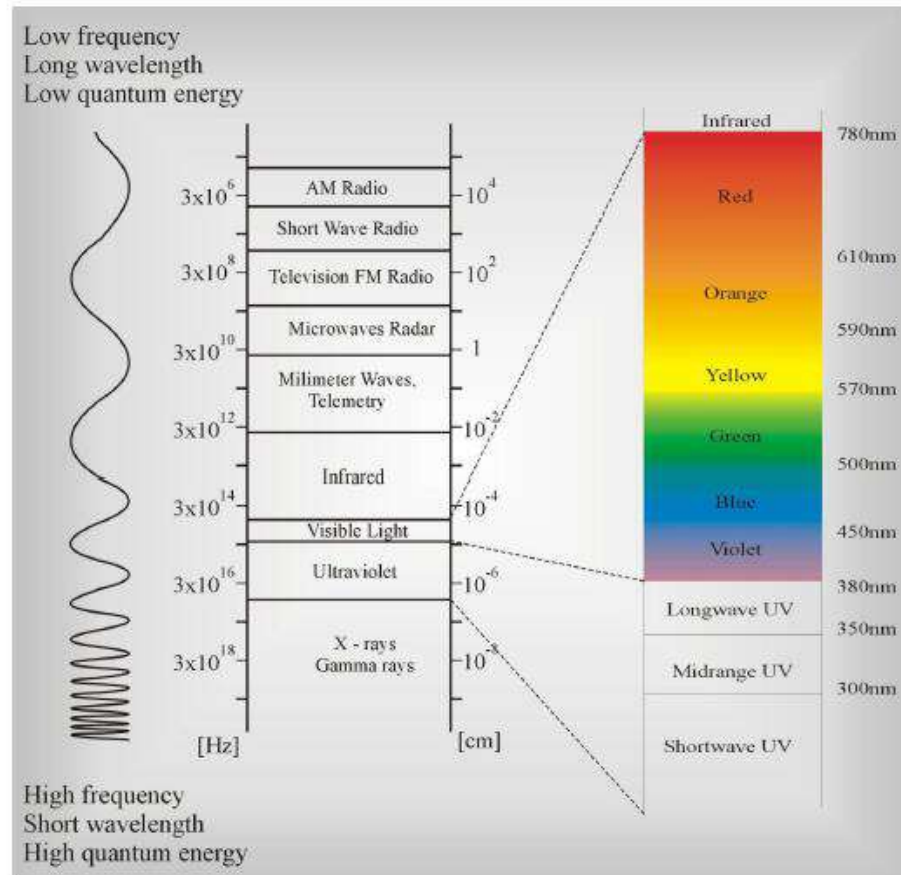


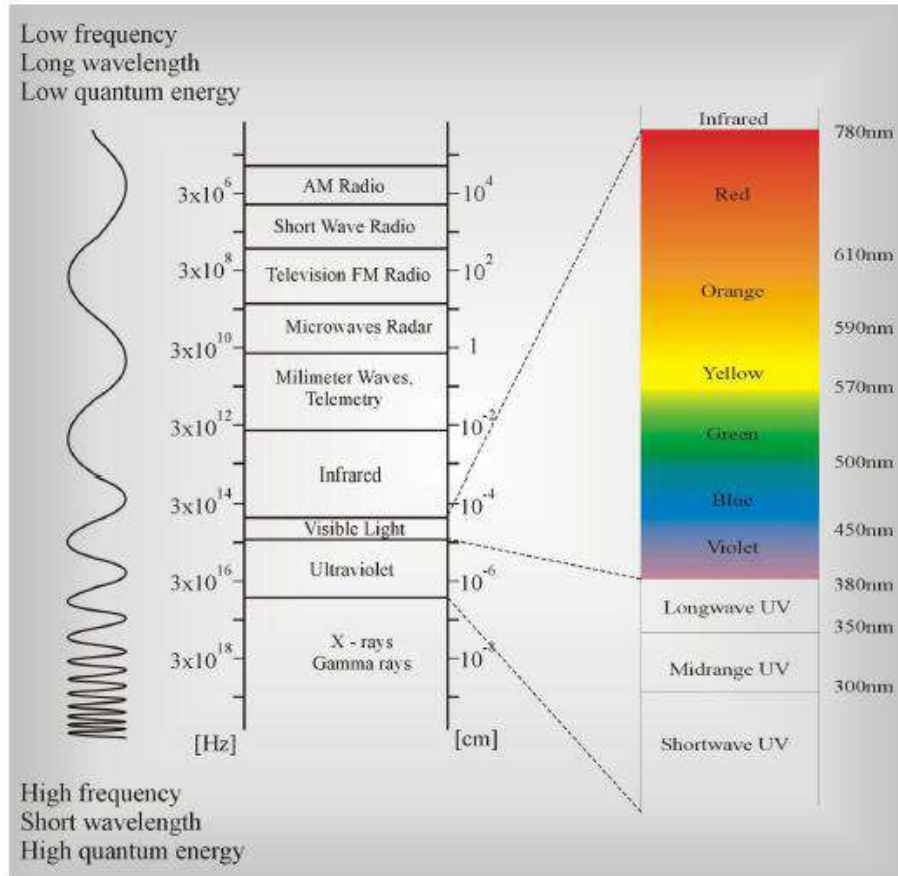
The properties of electromagnetic waves depend on the wavelength. Electromagnetic radiation of various wavelengths include radio waves, microwaves, infrared, light, ultraviolet, X-rays and gamma rays. Each spectral range of radiation is associated with a specific type of spectroscopy.



Frequency SPECTRUM

0 Hertz	Steady direct current
50-60 Hertz (5000Km)	AC power
-----USA-----	
16-16.000 kHz	Audio frequencies
10-30 kHz 30-10Km	v.l.f -very low frequency
30-30000 KHz	Radio Frequencies
30-300 kHz 10-1Km	l.f. low frequency
30-35 kHz	Marine com & navigation, aero nav.
300-3000 kHz 1000-100m	m.f medium frequencies
535-1635 kHz	AM broadcast bands
1800-2000 kHz	160 meter band
-----Football_Field-----	
3-30 MHz 100-10m	h.f. - high frequencies
3.5-4 MHz	80 me1erband
7-7.3 MHz	40 band
14-14.35 MHz	20 meter band
21-21.45 MHz	15meterbend
26.85-27.54 MHz	Industrial, Scientific, medical
28-29.7 MHz	10 meterband
26.86-27.455 MHz	Citizens Band Class D
-----Human-----	
30-300 MHz 10-1m	very high frequencies
44-49 MHz	Analog cordless phone
30-50 MHz	Police,fire,highway,railroad
50-54 MHz	6 meter band
54-72 MHz	TV channels 2 to 4
72-76 MHz	Government, Aero,Marker 75MHz
76-88 MHz	TV channels 5 and 6
88-108 MHz	FM broadcast band
108-118 MHz	Aeronautical navigation
118-136 MHz	Civil Communication Band
148-174 MHz	Government
144-148 MHz	2 meter band
174-216 MHz	TV channels 7 to 13
216-470 MHz	Amateur, government. CB Bend
	non-gov ,fixed or mobile ,aero navigate
220-225 MHz	Amateur band. 1-1/4 meter
225-400 MHz	Military
420-450 MHz	Amateur band, 0.7 meter
462.5-465 MHz	Citizens Band

The properties of electromagnetic waves depend on the wavelength. Electromagnetic radiation of various wavelengths include radio waves, microwaves, infrared, light, ultraviolet, X-rays and gamma rays. Each spectral range of radiation is associated with a specific type of spectroscopy.



-----Book-----

300-3000	MHz	100-10cm	u.h.f. - ultra high frequencies
470-890	MHz		TV channels 14 to 83
890-3000	MHz		Aero nav, amateur, Gov, fixed, mobile
800	MHz		RF wireless modems
806-890	MHz		Cellular Phones
900	MHz		digital cordless phones
900-929	Mhz		Personal Communication services (PCS)
929-932	Mhz		Nation wide pagers
932-940	MHz		two-way pagers
1.61-1.6263	GHz		Satellite phones uplink
1.85-2.20	GHz		Future PCS
2.4835-2.50	GHz		Satellite phones downlink
1.30-1.60	GHz		Radar band

-----Apple-----

3.0-30.00	GHz	10-1cm	s.h.f. - super high frequencies
			Government and non-government, amateur bands, radio navigation
4-6	Ghz		Satellite TV large dish
11.7-12.7	Ghz		Satellite TV small dish
28-29	GHz		Wireless "cable" TV

-----Grain_OF_SAND-----

30.0-300	GHz	1000-100um	Extra-high frequencies (weather radar, experimental, government)
----------	-----	------------	--

-----Bacterium-----

300	TeraHz	0.76-0.4um	Infrared light and heat
			Visiblelight
		6470-7000A	Red light
		5850-6740A	Orange light
		5750-5850A	Yellow light
		5560-5750A	Maximum visibility
		4912-5560A	Green light
		4240-4912A	Blue light
		4000-4240A	Violet light

-----Virus-----

30	petaHz	3900-32A	Ultraviolet light
		3200-1A	X-rays
		1-0.06 A	Gamma rays

-----Atom-----

		0.0005 Angs	Cosmic rays
--	--	-------------	-------------

-----Atomic_Nucleus-----

Spectroscopic techniques are very universal research tool in chemistry, physics, biology, medicine, diagnostics, material engineering, pharmacy and telecommunications. The basic idea of spectroscopy employs the interaction of electromagnetic waves with molecules of chemical compounds to obtain information about the structure of these molecules and processes occurring in them.

[NMR Spectroscopy](#)

[EPR Spectroscopy](#)

[Rotational spectroscopy](#)

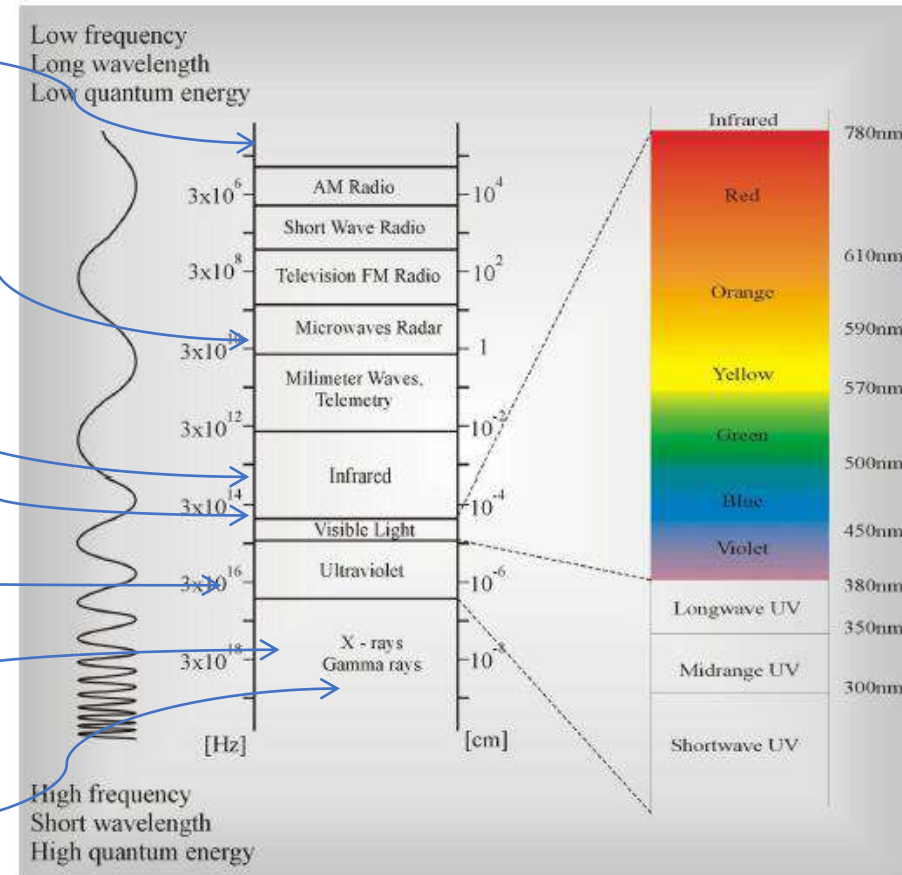
[IR spectroscopy](#)

[Raman spectroscopy](#)

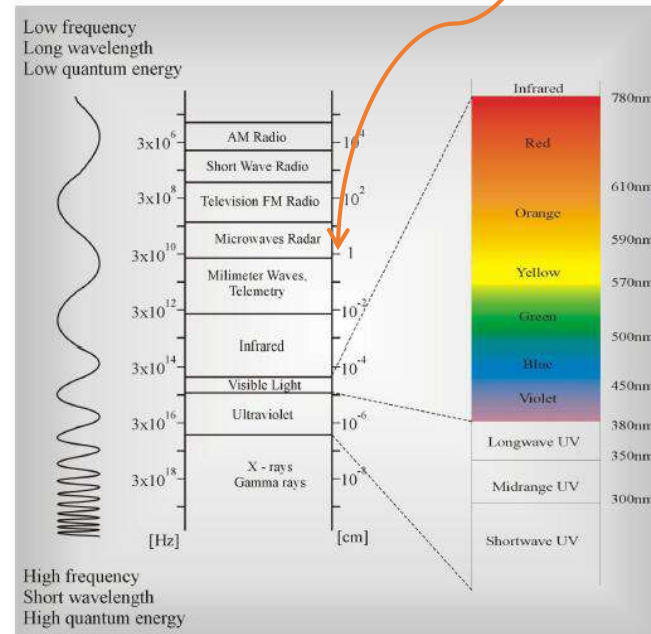
[VIS-UV spectroscopy](#)

[X ray spectroscopy](#)

[Mössbauer spectroscopy](#)



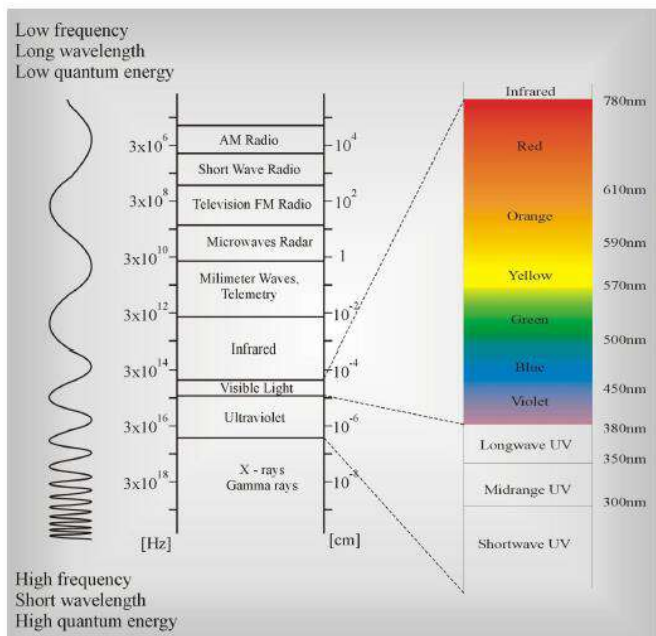
ROTATIONAL SPECTROSCOPY



Cell Phones

Our cell phones operate at 900 and 1800 MHz frequencies (megahertz = 1,000,000 Hertz) that corresponds to microwave spectral region. So why does our brain not boil during the conversation if we employ the same type of waves used to heat food? The answer is simple. The difference between these devices is that they emit radiation of different power.

The power of mobile phones is a fraction of a watt, in turn, while the power of macrowaves is around 1 kW (kilowatt = 1000 watt). Therefore, the radiation emitted by our cell phones, due to the low energy it carries, is not able to heat up our head significantly.



Autor opracowania: Łukasz Koszuk. Wszelkie uwagi i pytania proszę kierować na adres: luk.kosz@gmail.com
Wykonano na zlecenie **Działu Szkolenia i Doradztwa Instytutu Problemów Jądrowych im. Andrzeja Sołtana**
<http://www.ipj.gov.pl> • e-mail: dsid@ipj.gov.pl

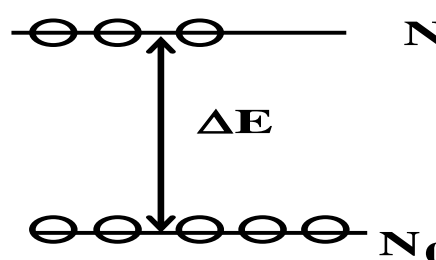
Cell Phones

Regardless of the terminology (Modes) used to characterize cellular technology (PCS, TDMA, CDMA, GSM, GPRS, Cellular, Digital, Analog, etc.), at this time there are only two frequency ranges available to US carriers.

(1) 824 - 896 MHz

(2) 1.85 -1.99 GHz

BOLTZMAN DISTRIBUTION

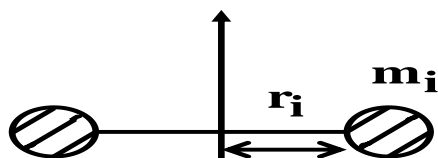
$$P(\mathbf{E}) \propto e^{-\mathbf{E}/kT}$$


$$\frac{N_1}{N_0} = e^{-\Delta E/kT}$$

ROTATIONAL SPECTRUM

Let us remind a rigid macroscopic rotator. The kinetic energy of a rotary motion is expressed by the formula:

kinetyczna energia rotacyjnego wyraża się wzorem



m_i - masa

r_i - odległość od osi obrotu

$$E_{\text{kin}} = \frac{1}{2} \sum m_i v_i^2 = \frac{1}{2} \sum_i m_i r_i^2 \omega^2 = \frac{1}{2} I \omega^2$$

gdzie

$$I = \sum m_i r_i^2$$

Moment of inertia

the kinetic energy of the macroscopic rotator can change continuously, it is

not quantized

w sposób ciągły, czyli jest niekwantowana.

The rotational energy of molecules is quantized (because the angular momentum is quantized)

$$E_k = \frac{1}{2} I \omega^2 = \frac{1}{2} \frac{(I\omega)^2}{I}$$

where $I\omega =$ angular momentum

You can show from the Schrodinger equation that

$$I\omega = \sqrt{J(J+1)}\hbar$$

$$E_k = \frac{1}{2} I \omega^2 = \frac{1}{2} \frac{(I\omega)^2}{I} = \frac{h^2}{8\pi^2 I} J(J+1)$$

where $J =$ Quantum number of rotations

$$J = 0, 1, 2, \dots, n$$

$$B = \frac{h^2}{8\pi^2 I}, \quad \text{where } B \text{ is a rotation constant}$$

if

$$J = 0$$

$$E_0 = 0$$

$$\Delta E_{01} = 2B$$

$$J = 1$$

$$E_1 = 2B$$

$$\Delta E_{12} = 4B$$

$$J = 2$$

$$E_2 = 6B$$

$$\Delta E_{23} = 6B$$

$$J = 3$$

$$E_3 = 12B$$

Distribution of Boltzman in rotational spectroscopy

$$\frac{n_J}{n_0} = \overbrace{(2J+1)}^? e^{-BJ(J+1)/kT}$$

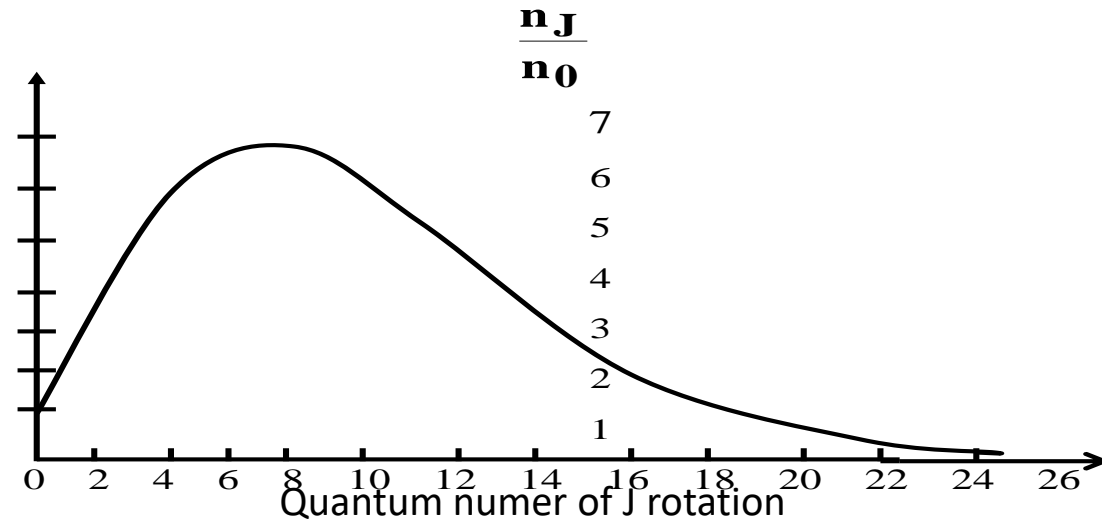
bo $\Delta E = E_J - E_0 = BJ(J+1) - 0 = BJ(J+1)$

because $E_0 = 0$ dla $J = 0$

Why before the exponent is 2J+1?

Because each energy level is characterized by angular momentum J, which is (2J+1) times degenerated.

Remember, we have a similar situation for an electron in a hydrogen atom: the orbital number l corresponds (2l+1) to the magnetic value of the quantum number m=(-1,..0, 1, ...,l)



Distribution of occupancy of rotational molecules at room temperature

SELECTION rules for the rotation of the rotational spectrum

1) $\Delta E = h\nu.$ The foton which is absorbed by the molecule must match the difference in Energy levels

2) $\int \Psi_n \mu \Psi_m d\tau \neq 0$ For the transition n-m

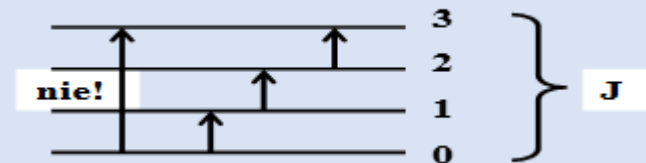
μ -permanent dipole moment of the molecule

Ψ_n, Ψ_m Wave function describing the rotator in the energy state n and m

It means that to observe the absorption spectrum, the molecules must be endowed with a permanent dipole moment

3) $\Delta J = +1$ The molecule can be transferred in one absorption act only to the neighboring level

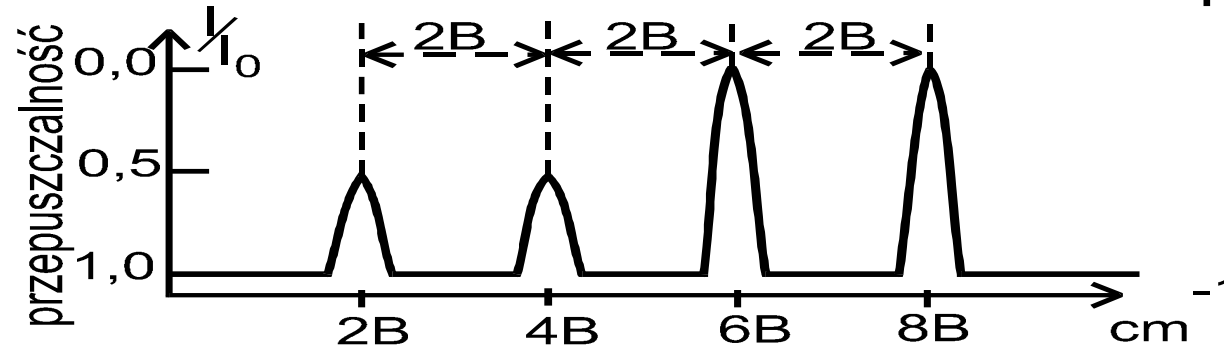
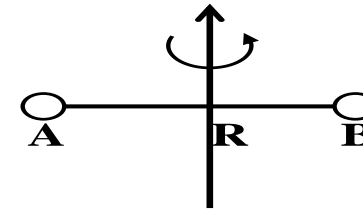
$\Delta J = 2, 3$ They are forbidden



Study of the structure of molecules based on the rotational spectrum

Diagram of absorption transitions and the appearance of rotational spectrum:

a) two-atom molecule



Knowing B from experiment (the distance between the peaks in the spectrum) you can calculate the moment of inertia and hence the distance R between atoms A and B

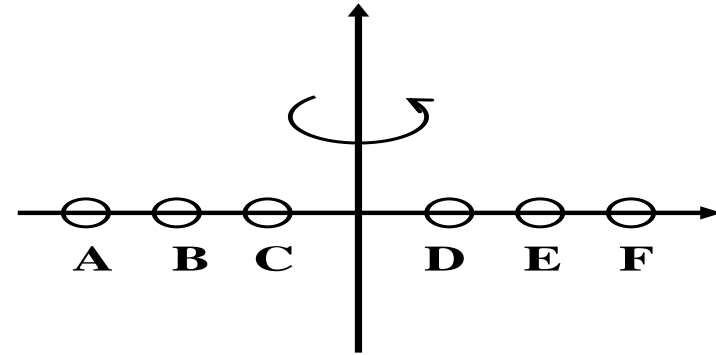
$$B \Rightarrow B = \frac{h}{8\pi^2 c \mathbf{I}} \Rightarrow \mathbf{I} \Rightarrow R$$

Where B is expressed in units $[\text{cm}^{-1}]$

$$\mathbf{I} = m_{\text{red}} \cdot R^2$$

$$m_{\text{red}} = \frac{m_A \cdot m_B}{m_A + m_B}$$

a) Polyatomic linear molecule
 Rotational spectra look similar (distances are equal to 2B), hence I can be determined



But now the moment of inertia I expresses a more complicated pattern:

$$\mathbf{I} = \frac{1}{2} \sum_{\mathbf{i}} \sum_{\mathbf{j}} \mathbf{m}_{\mathbf{i}} \mathbf{m}_{\mathbf{j}} \mathbf{R}_{\mathbf{ij}} / \sum_{\mathbf{i}} \mathbf{m}_{\mathbf{i}}$$

In the n atomic molecule we have (n-1) independent variables R_{ij} (interatomic distances). To determine them you need (n-1) equations. These data are obtained using isotopic substitutions. However, one must remember that the formula for rotational energy:

$$\mathbf{E}_{\mathbf{J}+1} - \mathbf{E}_{\mathbf{J}} = 2\mathbf{B}(\mathbf{J} + 1)$$

is not completely precise. In fact, we assume a rigid rotator model. Moreover, the atoms are vibrating. Therefore the distances between atoms change. Besides, for higher J the rotation is so fast that the centrifugal force starts to play.

Modified pattern that included:

- a) rotation coupling with vibration
- b) centrifugal force has the form

$$E_{J+1} - E_J = 2B_v(J+1) - 4D(J+1)^3$$

where

$$B_v = B - \sum_{i=1}^{3n-5} \alpha_i \left(v_i + \frac{d_i}{2} \right)$$

← correction for centrifugal force

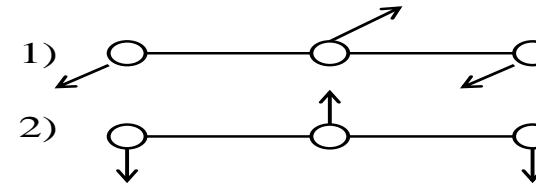
← correction for coupling with vibrations

α_i - coupling factor

v_i - oscillating quantum number

d_i - degree of degeneration of oscillations

c) polyatomic nonlinear molecules



c1) $I_A = I_B = I_C$ - spherical rotator

uninteresting case for rotational spectroscopy, because $\mu = 0$

c2) $I_A \neq I_B = I_C$ - symmetrical rotator has two rotational constants

$$A = \frac{h^2}{8\pi^2 c I_A}; \quad B = \frac{h^2}{8\pi^2 c I_B}$$

rotational energy of the symmetrical rotor is expressed by the formula

$$E_{JK} = BJ(J+1) + (A-B)K^2$$

$$K = 0, \pm 1, \dots, \pm J$$

Selection rules for a symmetrical rotator

$$\Delta J = +1$$

$$\Delta K = 0$$

It means that

$$\Delta E_{JK} = 2B(J+1) \quad \text{the same as for linear molecules}$$

but after adjusting the centrifugal force the pattern is different:

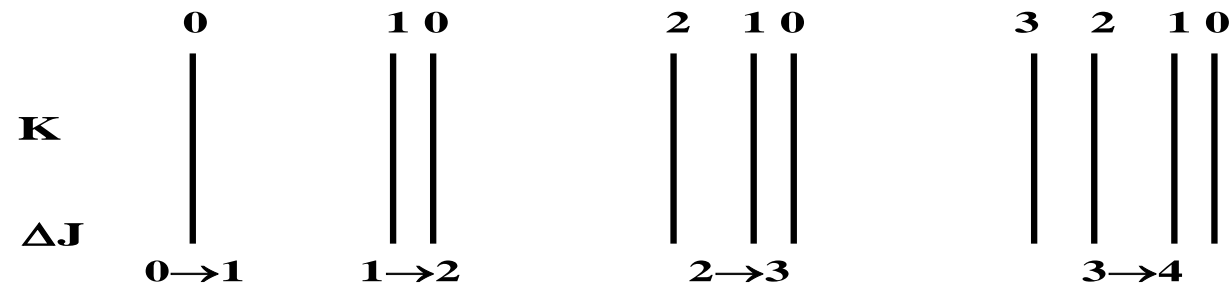
$$\Delta E_{JK} = 2(J+1)(B - D_{JK}K^2) - 4D_J(J+1)^3$$

dla $K =$ the pattern assumes the same form as for linear molecules

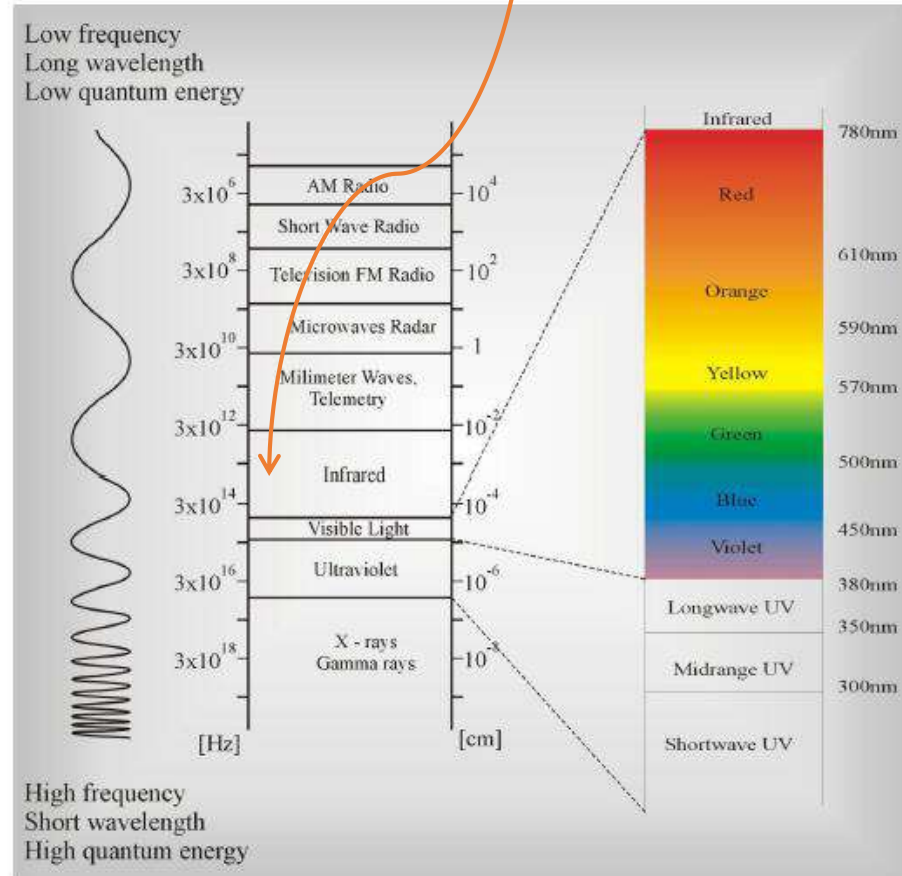
for transitions $0 \rightarrow 1$

$$\Delta E_{JK} = 2(J+1)B - 4D(J+1)^3$$

but for higher rotational levels $J > 0$. K can have values of $0, +1, \dots, +J$, which means that each transition band $J \rightarrow J+1$ splits into $J+1$



IR spectroscopy



The term IR spectroscopy covers the range of electromagnetic radiation in the range 0.78-1000 μm . We distinguish near, middle and far IR. The region 4000-500 cm^{-1} is the most useful.

IR spectroscopy provides information on vibrations of molecules.

Region	Wavelength range (μm)	Wavenumber range (cm^{-1})
Near	0.78 - 2.5	12800 - 4000
Middle	2.5 - 50	4000 - 200
Far	50 -1000	200 - 10

POMOC

<http://www.spectroscopynow.com/coi/cda/detail.cda?id=18427&type=EducationFeature&chId=2&page=1>

The atoms in the molecule vibrate around the equilibrium position. A molecule consisting of N atoms has $3N$ degrees of freedom. 3 degrees of freedom are needed to describe the translation of the molecule (x , y , center of mass) and 3 (2 for a linear molecule) degrees to describe the rotation. Thus, $3N-6$ ($3N-5$) degrees of freedom describes the vibration of the molecule.

Harmonic oscillator model

- The vibrations of molecules can be described using mechanical models using the laws of classical mechanics.
- Most often we imagine the vibrations of molecules using a harmonic oscillator, where two masses m_1 and m_2 are connected by a spring, with the elasticity characterized by the force constant f [N / m]
- A harmonic oscillator is an oscillator that meets Hooke's law

$$F = -fq$$

- which says that the force F that is needed to stretch the spring is proportional to the deflection q and directed opposite to the inclination



let's count the frequency of the harmonic oscillator

$$\mathbf{F} = -f\mathbf{q}$$

$$\mathbf{q} = \mathbf{r} - \mathbf{r}_e$$

f – spring constant

r – the distance between atoms

r_e – balance distance

$$\mathbf{q} = \mathbf{Q} \cos 2\pi\nu t$$

Q – amplitude

ν – frequency of vibrations

$$[\mathbf{Hz}] = \left[\frac{1}{s} \right]$$

potential energy of the oscillator

work done on the system

$$dU = (-F)dq$$

$$dU = fq dq$$

$$\frac{dU}{dq} = fq$$

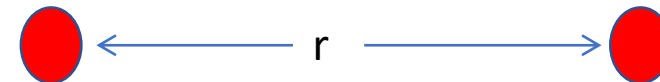
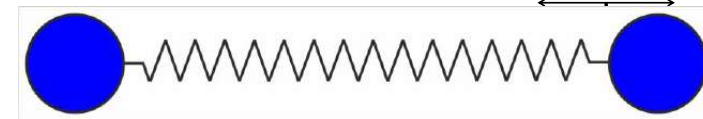
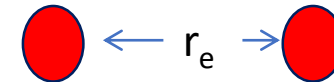
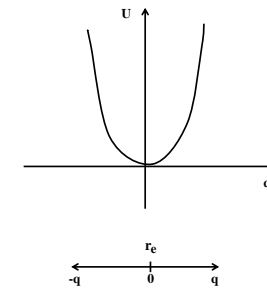
$$\frac{d^2U}{dq^2} = f$$

a) oscylator klasyczny

$$U = \frac{fq^2}{2} \quad E_k = \frac{mv^2}{2} = \frac{mq^2}{2}$$

energia calkowita:

$$E = E_k + U$$



$$U = \int (-F) dq = \int f q dq = \frac{1}{2} f q^2$$

$$U = \frac{1}{2} f q^2$$

$$m \cdot a = F$$

$$m \cdot \frac{d^2 q}{dt^2} = -f q$$

summarizing

$$q = Q \cos 2\pi \nu t$$

receive

$$m(2\pi \nu)^2 = f \Rightarrow$$

$$\nu = \frac{1}{2\pi} \sqrt{\frac{f}{m}}$$

$$m_{red} = \frac{m_1 \times m_2}{m_1 + m_2} \quad [kg]$$

We have obtained that the frequency of the harmonic oscillator depends on the force constant f and on the reduced mass m of the oscillator, where $m = m_1 m_2 / (m_1 + m_2)$

a) A quantum oscillator

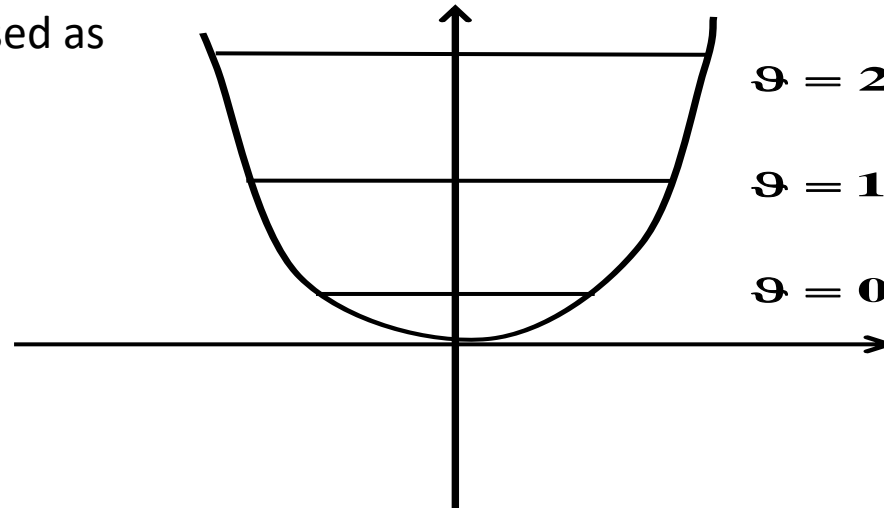
for the quantum oscillator, the Schrödinger equation should be solved

$$-\frac{\hbar^2}{2m} \frac{\partial^2 \Psi}{\partial q^2} + \frac{fq^2}{2} \Psi = E\Psi \quad \Rightarrow$$

In case of using quantum-mechanical methods, the harmonic Energy of the harmonic oscillator in the state described by the quantum oscillating number ν is expressed as follows:

$$E = h\nu\left(\nu + \frac{1}{2}\right)$$

$$\nu = 0, 1, 2, \dots$$



POMOC – CHEMIA
KWANTOWA-WYKŁAD
1 | 2

$$E_2 = \frac{5}{2} h\nu$$

$$E_1 = \frac{3}{2} h\nu$$

$$E_0 = \frac{h\nu}{2}$$

That is $\nu = 0$ for energy it is not equal to zero. This energy is called zero point energy.

The harmonic oscillator model, whose energy curve is a parabola, does not properly describe the energy of the molecule, because it does not allow binding dissociation. In real situations, molecular oscillators are anharmonic. The energy of transitions decreases with the increase of the quantum oscillatory number, until the dissociation of the molecules.

a) anharmonic oscillator

$$-\frac{\hbar^2}{2m} \frac{\partial^2 \Psi}{\partial q^2} + U\Psi = E\Psi \quad (1)$$

ale $U \neq \frac{f q^2}{2}$

and it expressed more complicated dependence

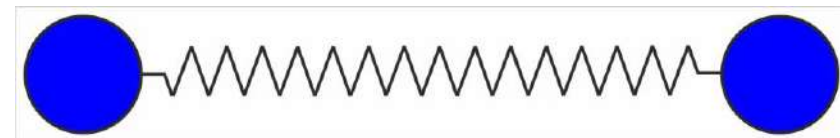
$$U(q) = U(0) + \left(\frac{\partial U}{\partial q} \right) q + \frac{1}{2!} \underbrace{\frac{\partial^2 U}{\partial q^2}}_f q^2 + \frac{1}{3!} \underbrace{\frac{\partial^3 U}{\partial q^3}}_k q^3 + \dots$$

$$U(q) = \frac{f q^2}{2} + \frac{1}{6} k q^3 \quad (2) \Rightarrow (1) + (2)$$

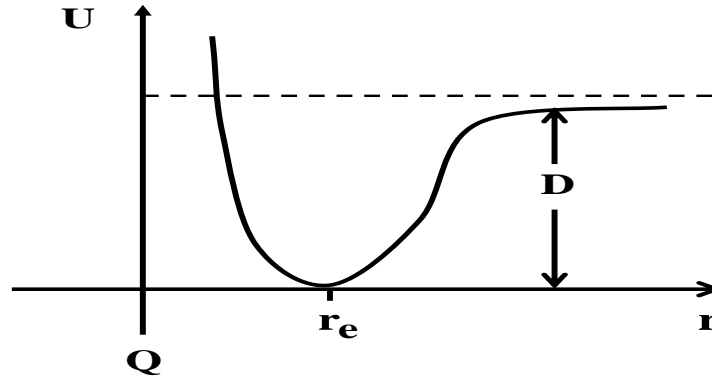
$$E = h\nu \left(\vartheta + \frac{1}{2} \right) - h\nu x \left(\vartheta + \frac{1}{2} \right)^2$$

$$\Delta E = h\nu [1 - 2x(\vartheta + 1)]$$

where x is the so-called anharmonicity constant.



The energy curve of the anharmonic oscillator is approximated by the Morse function presented below:



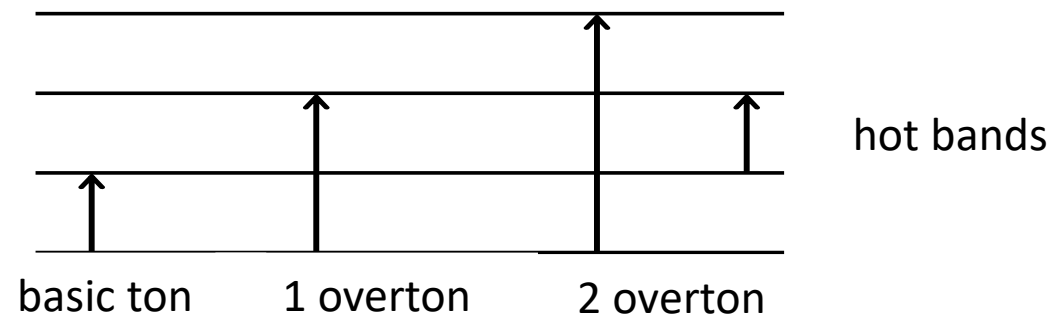
$$U(q) = D(1 - e^{-\beta q})^2$$

$$\Delta \nu = \pm 1$$

for a harmonic oscillator

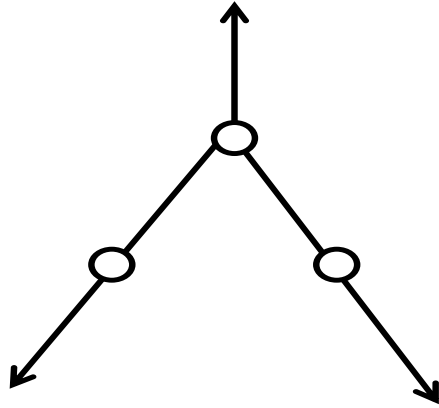
$$\Delta \nu = \pm 1, \pm 2, \pm 3$$

for a anharmonic oscillator

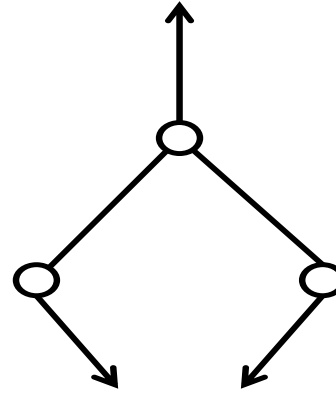


Types of vibrations

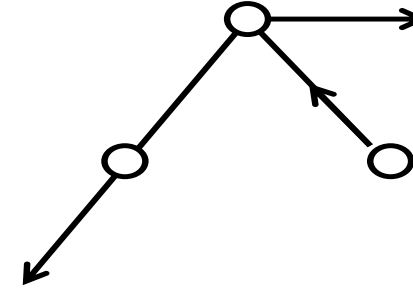
$3N-6$



ν_1
Symmetric
vibrations



ν_2
bending
vibrations



ν_3
asymmetric
stretching
vibrations

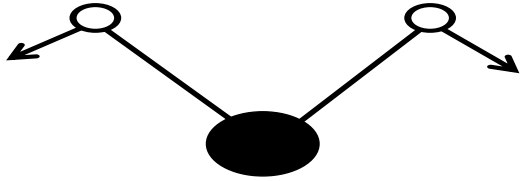
- a) symmetric
- b) asymmetric

- a) bending
- b) stretching

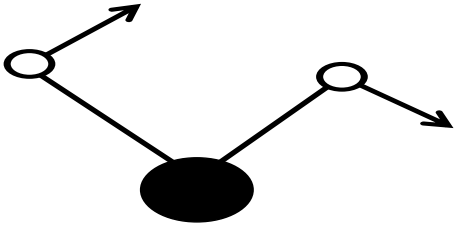
- a) vibrations in plane
- b) vibration outside the plane

XYZ

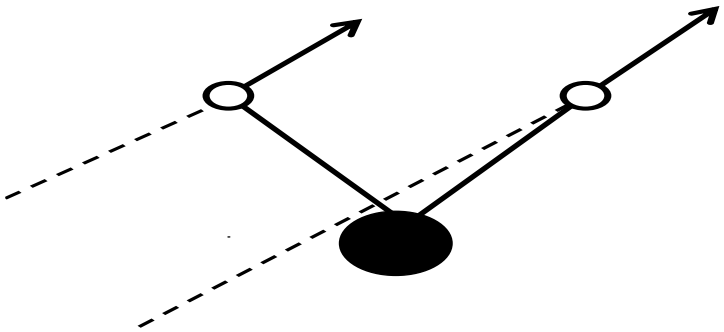
X – heavy atom



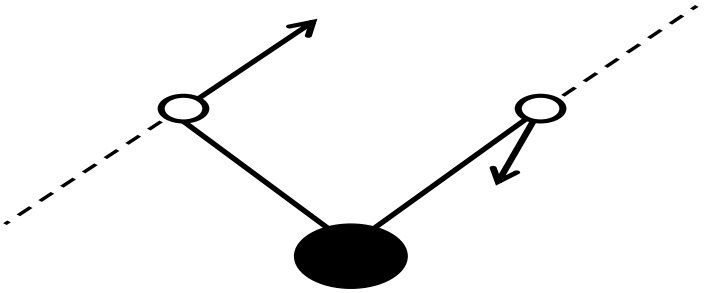
(scissoring)



(rocking)



(wagging)



(twisting)

Selection rules for transitions in IR spectroscopy (infrared)

1) Radiation photons must have energy equal to the difference in energy of vibrational energy levels

$$h\nu = \Delta E$$

2) The transition occurs only when the quantum number of oscillations changes by 1,2,3

$$\Delta \nu = +1$$

for a harmonic oscillator

$$\Delta \nu = +1, +2, +3$$

for the anharmonic oscillator

3) Transitions between quantum states l to m are visible in IR spectroscopy only for those oscillators in which the dipole moment of the molecule changes during the oscillation $\frac{\partial \mu}{\partial q} \neq 0$

$l \rightarrow m$

$$\mu_{lm} = \int_{-\infty}^{\infty} \Psi_l \mu \Psi_m dq = \int_{-\infty}^{\infty} \Psi_l \frac{\partial \mu}{\partial q} \Psi_m dq \neq 0$$

gdzie

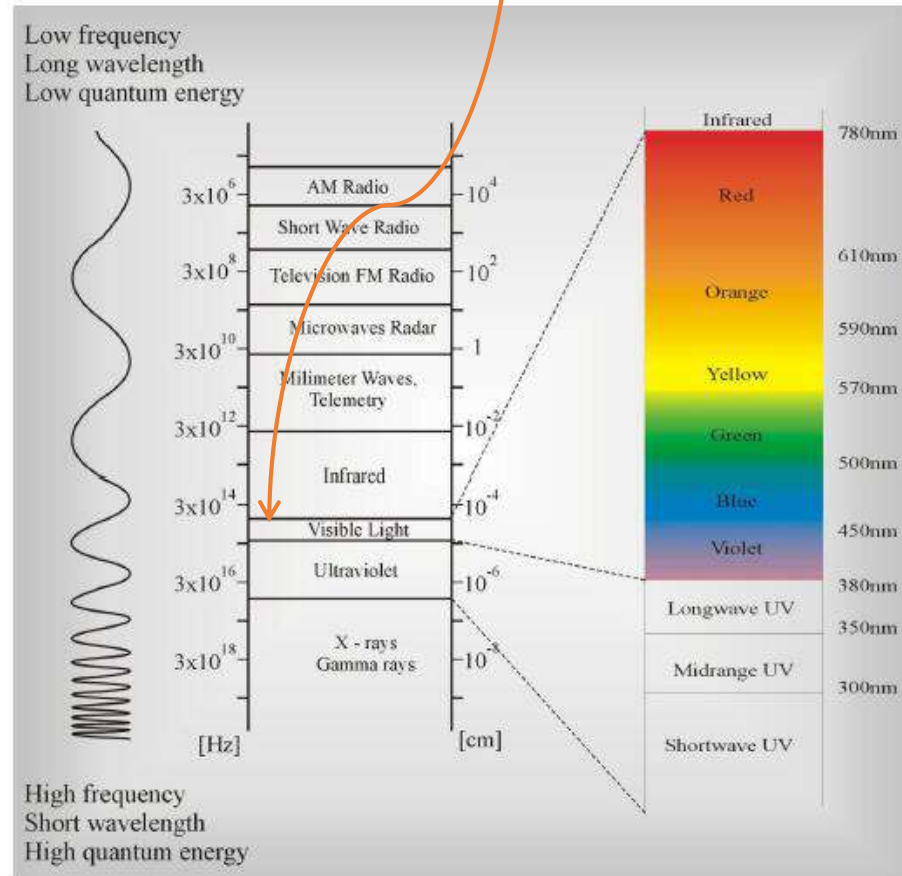
$$\left. \begin{array}{l} \Psi_l \\ \Psi_m \end{array} \right\}$$

wavenumber functions of the harmonic oscillator in the state of l and m

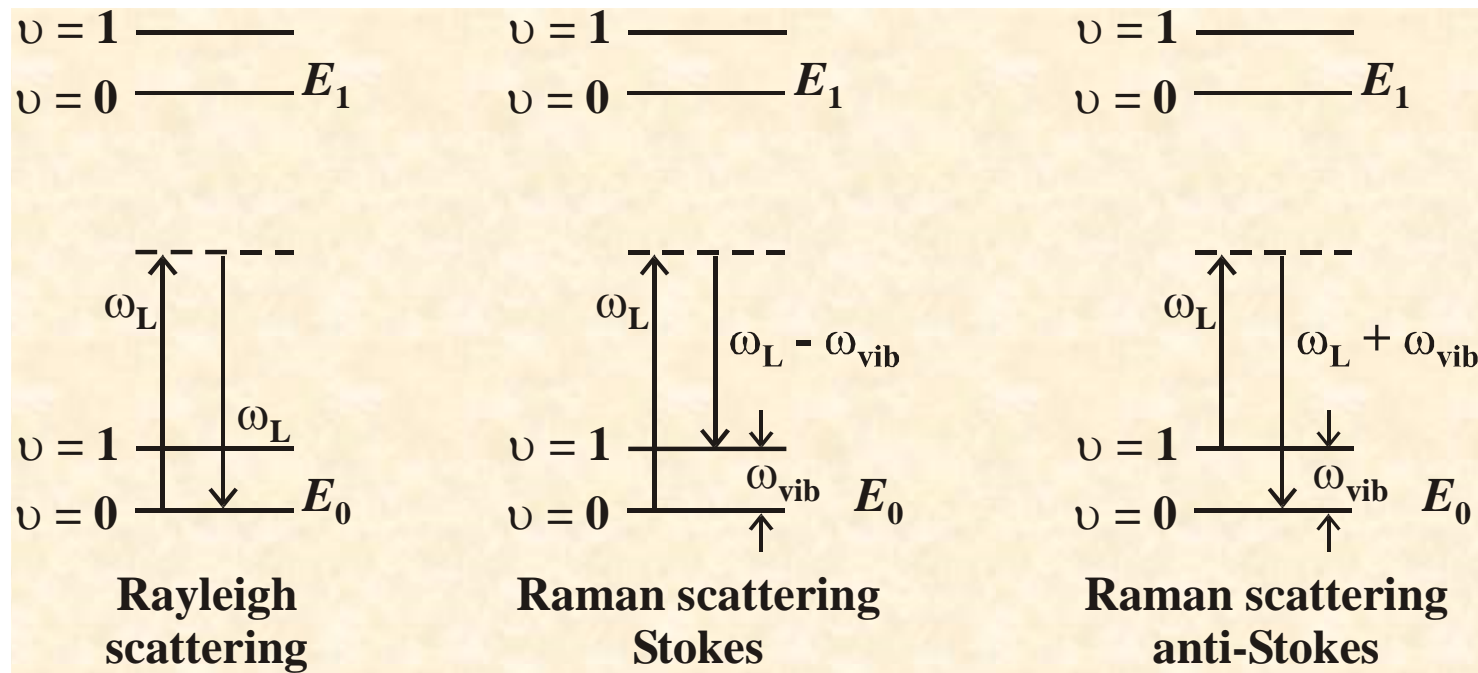
Raman spectroscopy



Raman spectroscopy

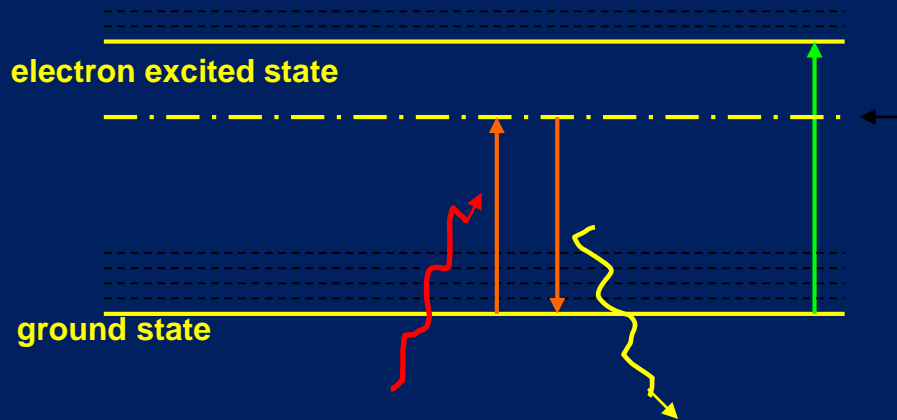
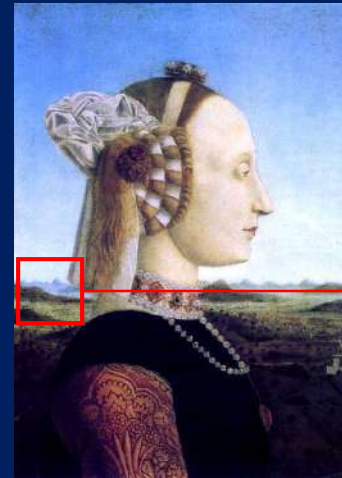


RAMAN SPECTROSCOPY AND RAMAN IMAGING

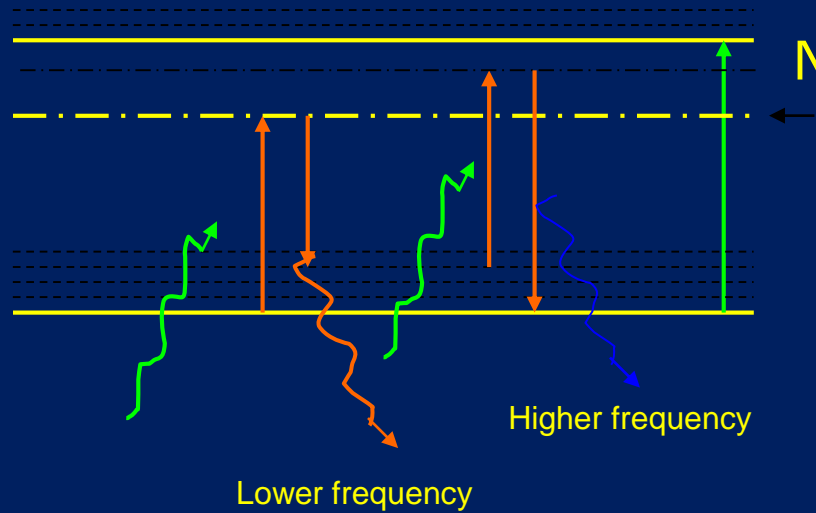




ELASTIC SCATTERING

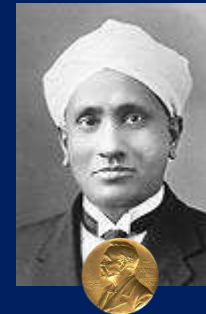


But light can be scattered in another way- Raman scattering



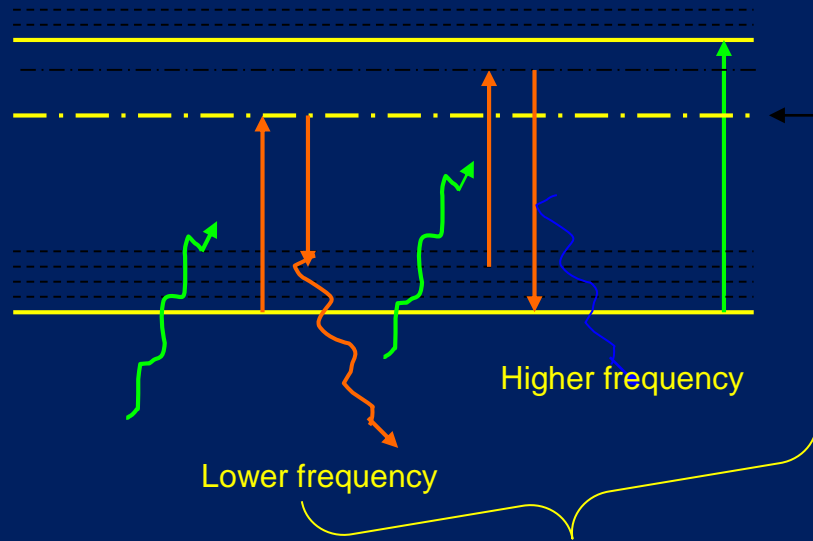
Non-elastic scattering

In the scattered light I have found the frequencies different from the frequencies of the incident excitation light



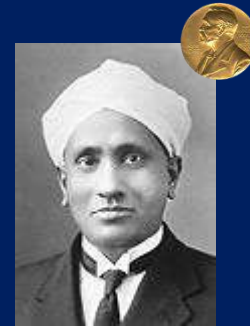
Chandrasekhara
Venkata Raman

But light can be scattered in another way- Raman scattering

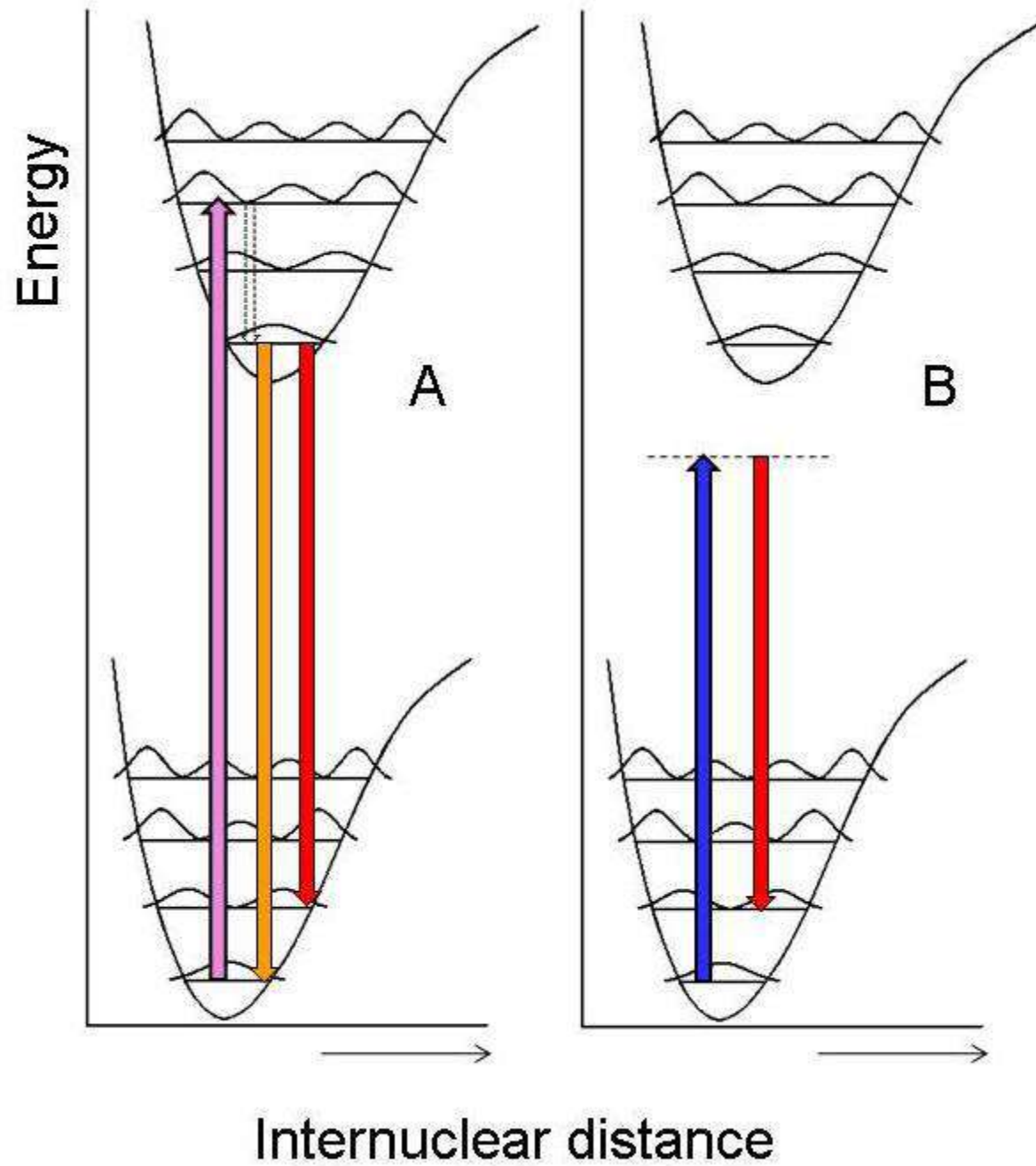


In the scattered light I have found the frequencies different from the frequencies of the incident excitation light

Measuring the energy difference between incident and scattered light we get information about vibrations of molecules.



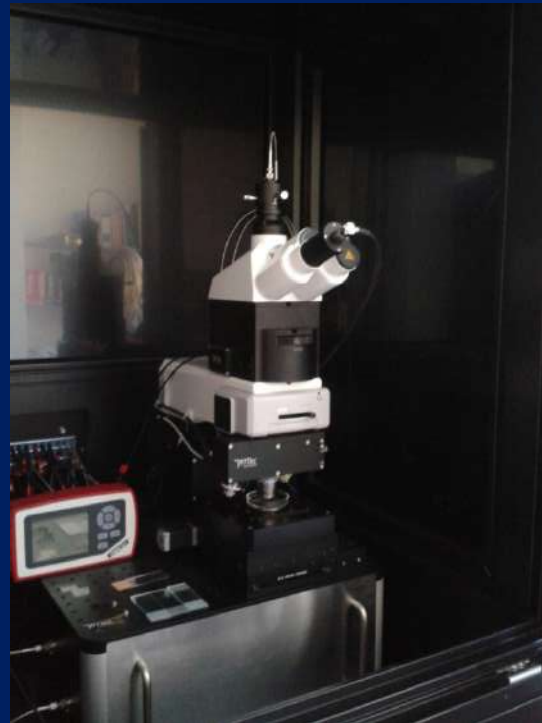
Chandrasekhara
Venkata Raman



Biomedical applications



- High spatial resolution RAMAN IMAGING
- SNOM microscopy (far below the diffraction limit, SNOM)



Alpha 300 RSA+ (WITec), 355, 532, 785 nm

CONFOCAL RAMAN MICROSCOPY

diffraction limited

$$\delta_{lat} = 0.61 \lambda / NA$$



Laser

Lustra skanujace

$$\delta_{ax} = 2 \lambda n / (NA)^2$$



Skaner w osi Z

**3D imaging and deep profiling
due to confocal configuration**

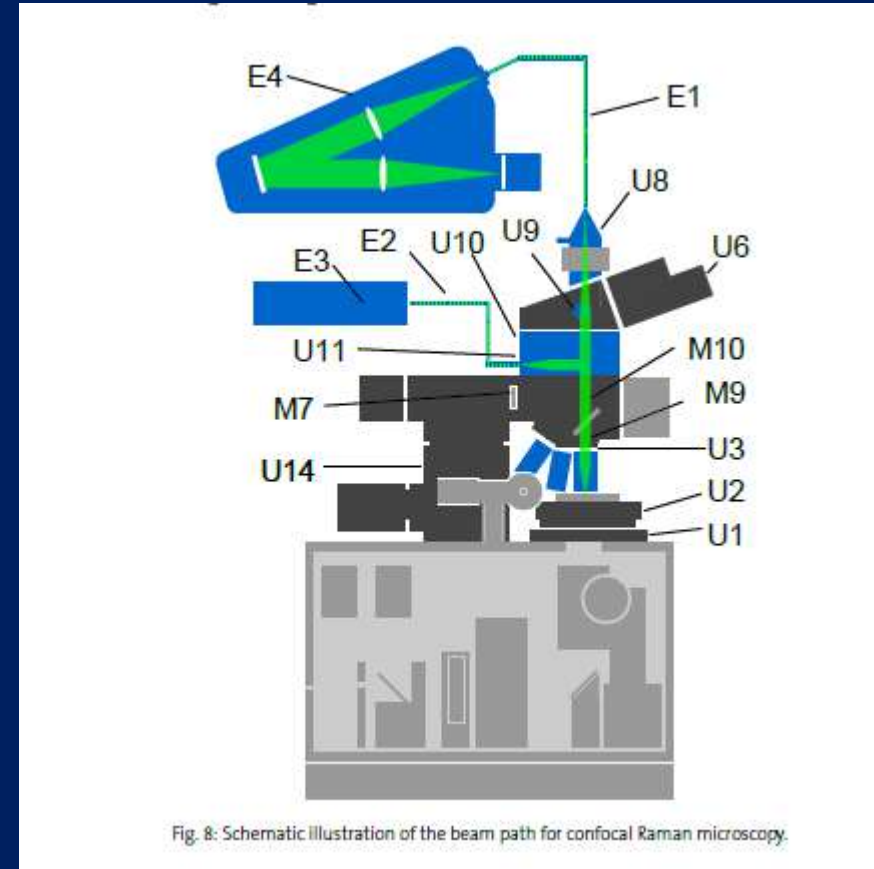
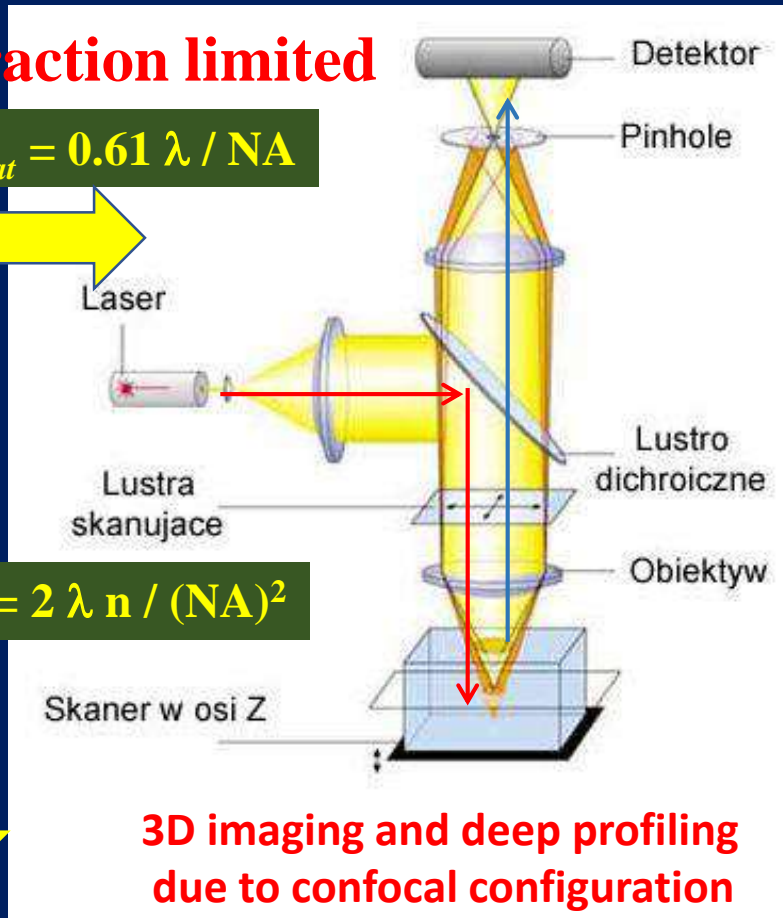
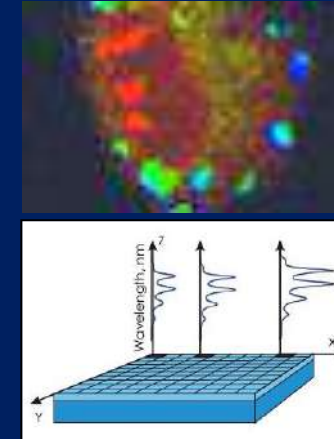


Fig. 8: Schematic illustration of the beam path for confocal Raman microscopy.

1.5 Confocal Raman Microscopy

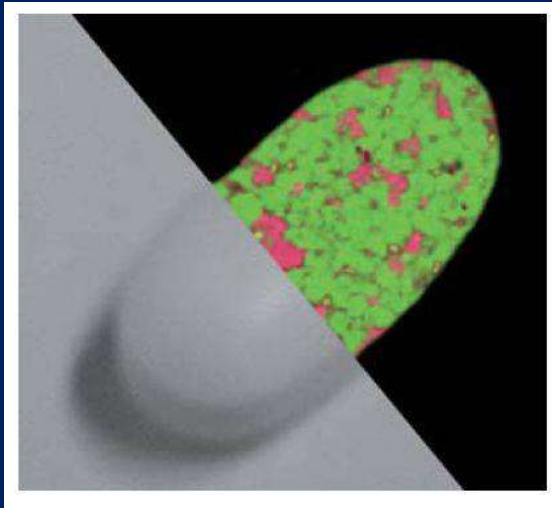
Confocal microscopy requires a point source (usually a laser), which is focused onto the sample. The reflected light (Raman, fluorescence) is collected with the same objective and focused through a pinhole at the front of the detector (Fig. 3). This ensures that only light from the image focal plane can reach the detector, which greatly increases image contrast and with the proper selection of pinhole size, slightly increases resolution (max. gain in resolution: factor $\sqrt{2}$).

Raman imaging



- Raman microscopy
- Confocal raman microscopy
- Collection of spacially resolved spectroscopic data by raster-scanning the focused laser beam over the sample, or by moving the sample through the laser focus in a raster pattern via a high resolution microscope stage
- The resulting spectral data can be converted into spectral images
- Improvement of spectral images with different statistical methods, Principal Component analysis (PCA), Vertex Component Analysis (VCA), Hierarchical Cluster Analysis (HCA)

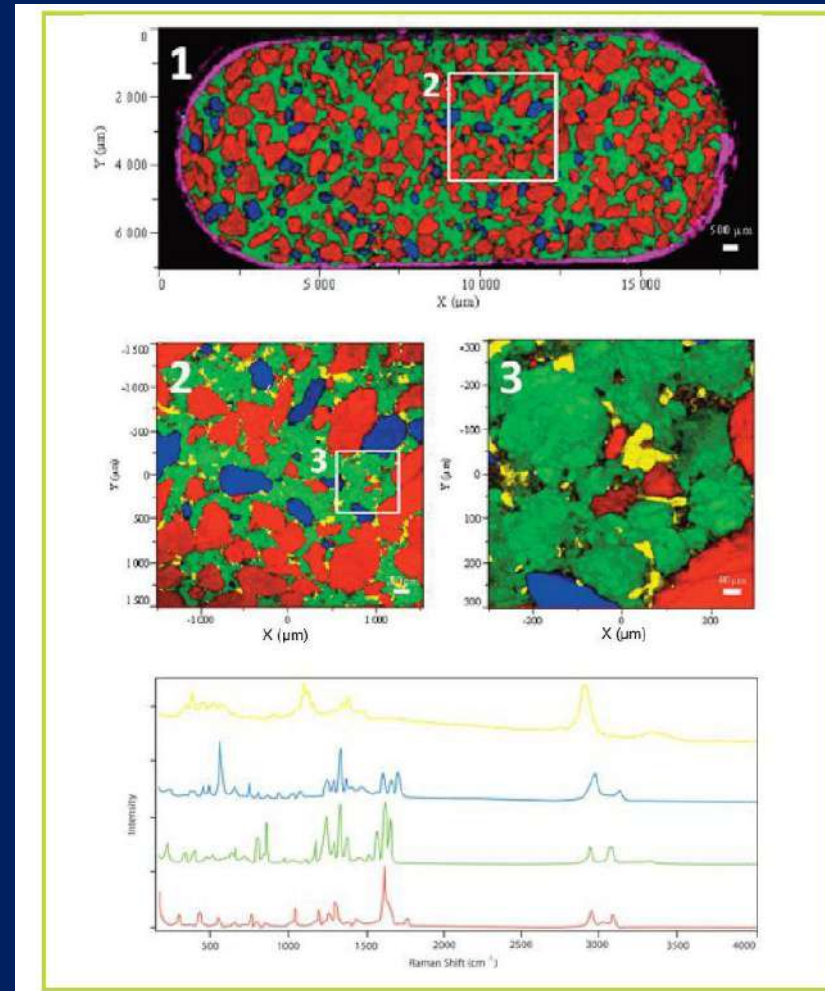
6. Analizy farmaceutyczne



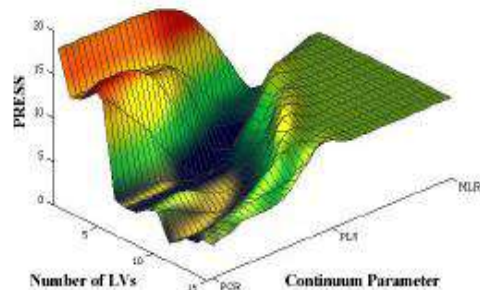
kofeina
kwasy acetylosalicylowy
**paracetamol- *N*-(4-
hydroksyfenylo)acetamid**

widma Ramana
składników tabletki

<http://www.horiba.com>



PRINCIPAL COMPONENT ANALYSIS (PCA)



PLS_Toolbox 4.0

for use with MATLAB™

Barry M. Wise
Neal B. Gallagher
Rasmus Bro

Jeremy M. Shaver
Willem Windig
R. Scott Koch



PLS_Toolbox Version 4.0
for use with MATLAB™

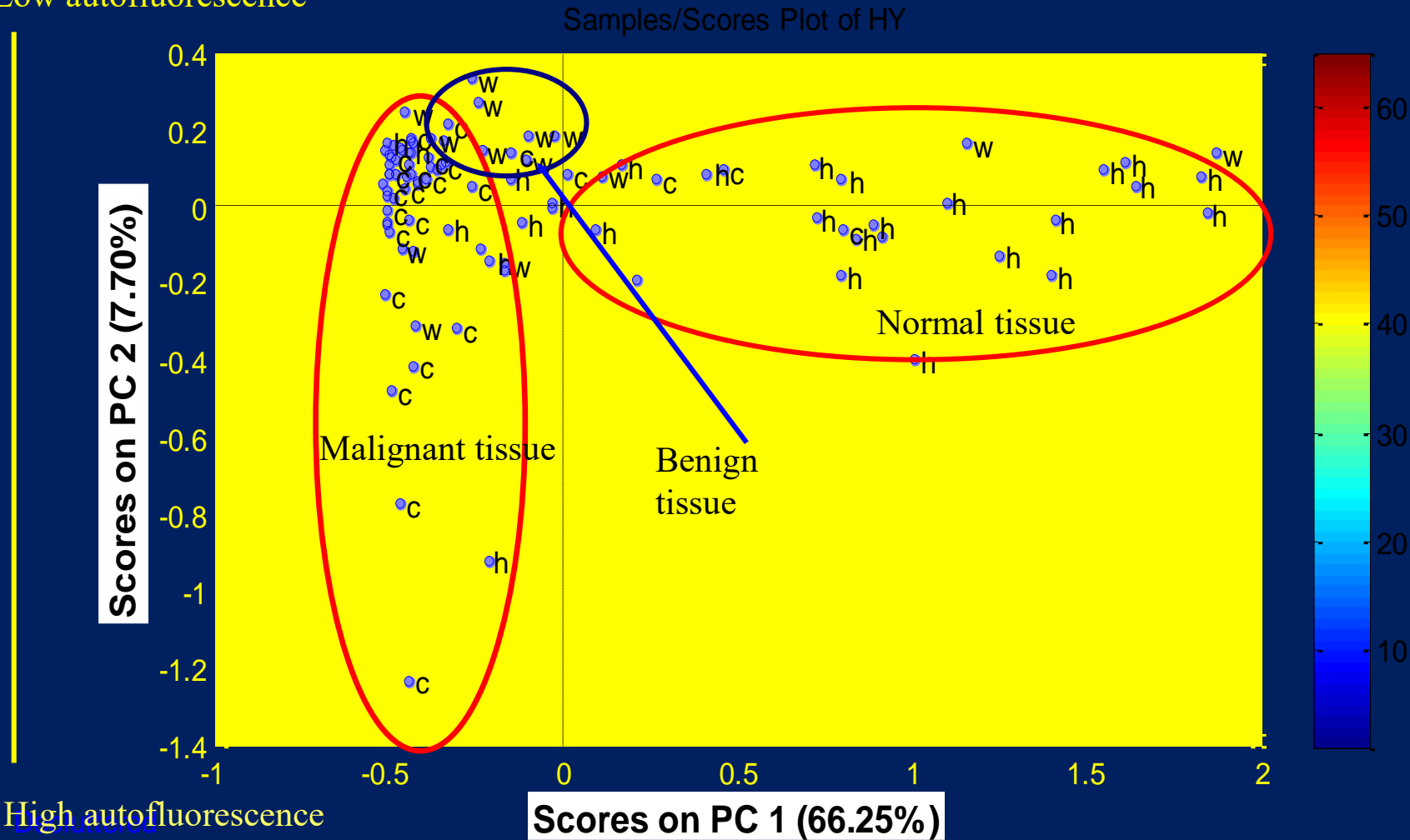
Barry M. Wise
Neal B. Gallagher
Rasmus Bro
Jeremy M. Shaver
Willem Windig
R. Scott Koch

Eigenvector Research, Inc.
3905 West Eaglerock Drive
Wenatchee, WA 98801

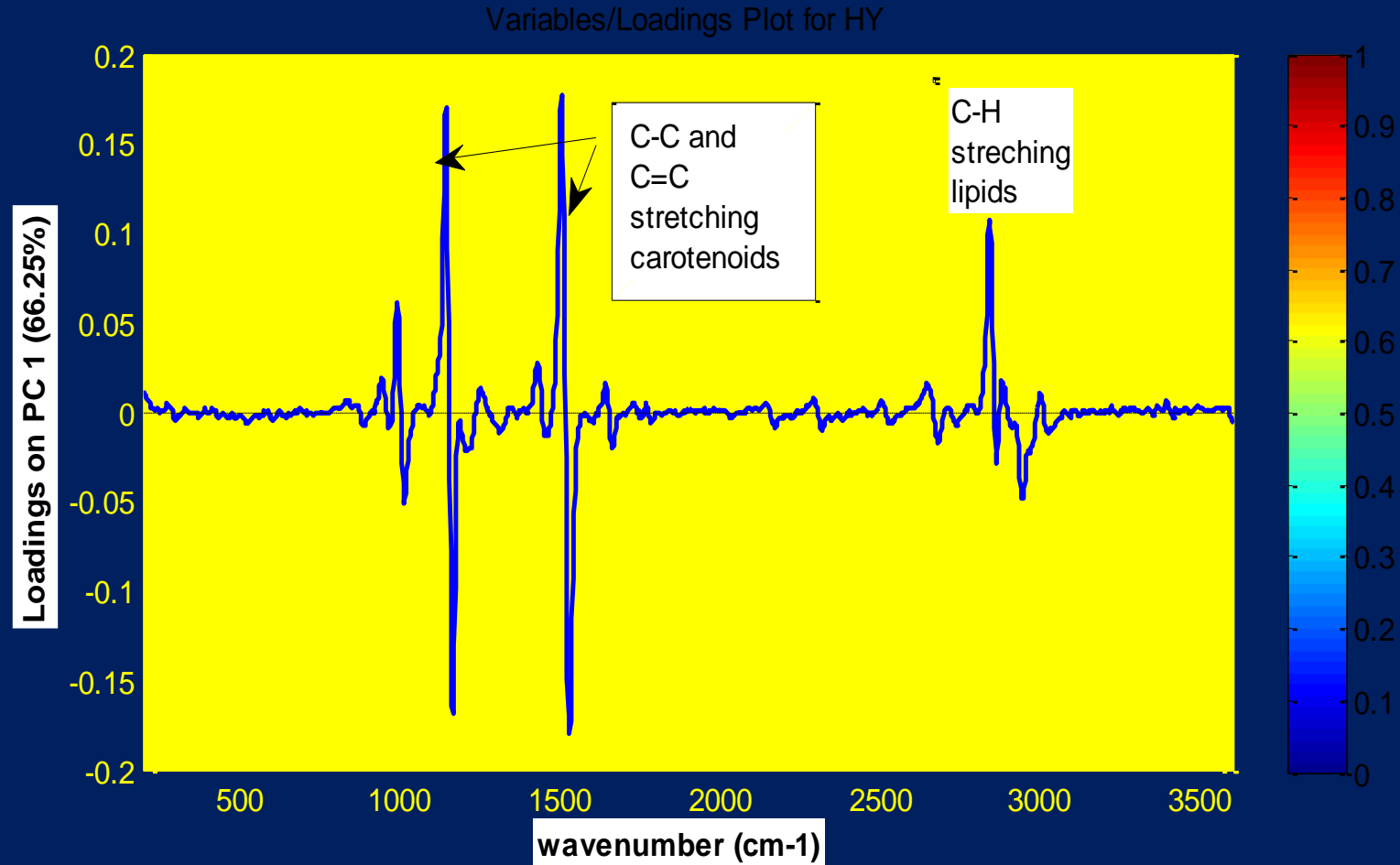
helpdesk@eigenvector.com
www.eigenvector.com

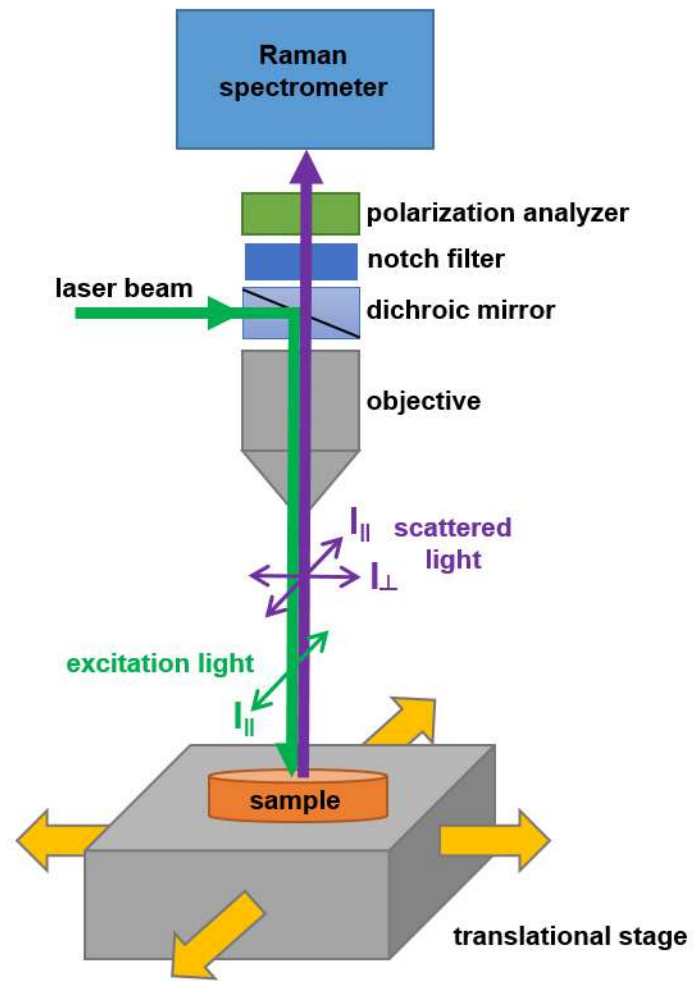
PCA score plot – mean center, SNV, 1-st derivative

Low autofluorescence



PCA loading plot – mean center, SNV, 1-st derivative





Nanooncology: Raman imaging and atomic force microscopy as a tool for proteomic, lipidomic, glycomic, epigenetic studies .

The biochemical, nanomechanical and chemometric signatures of brain, breast and intestine cancers.

Halina Abramczyk

**Lodz University of Technology, Laboratory of
Laser Molecular Spectroscopy, Lodz, Poland**

Kraków 2018



Lodz University of Technology, Faculty of Chemistry , Laboratory of Laser Molecular Spectroscopy, Lodz, Poland



**Jacek Musiał² Radzislaw Kordek²
Alina Morawiec-Sztandera² Krystyna Fabianowska²
Eric Freysz³ Lech Polis⁴ Bartosz Polis⁴**

**²Medical University of Lodz, Department of
Pathology, Chair of Oncology, Paderewskiego 4, 93-
509 Lodz, Poland**

**³Laboratoire Ondes et Matière d'Aquitaine (LOMA),
UMR 5798 Université Bordeaux 1, France**

**⁴Polish Mother's Memorial Hospital Research
Institute, Department of Neurosurgery and
Neurotraumatology, 3-338 Lodz, Poland**



dr hab. inż. Beata Brożek-Płuska

brozek@mitr.p.lodz.pl

pok. 303

website



dr inż. Jakub Surmacki

jsurmacki@mitr.p.lodz.pl

pok. 303

website



dr Rafał Kania

rkania@mitr.p.lodz.pl

pok. 309

website



dr inż. Arkadiusz Jarota

ajarota@mitr.p.lodz.pl

pok. 309

website



mgr inż. Monika Kopeć

mkopec@mitr.p.lodz.pl

pok. 303

website



mgr Anna Imiela

anna.imiela@p.lodz.pl

pok. 303

Lodz University of Technology, Faculty of Chemistry,
Laboratory of Laser Molecular Spectroscopy, Lodz, Poland

COOPERATION WITH MEDICAL CENTERS

Uniwersytet Medyczny w Łodzi

Katedra Onkologii

Prof. dr hab. n. med. Radziław Kordek

Dr n. med. Jacek Musiał

WSS i M. Kopernika w Łodzi

Prof. dr hab. n. med. Z. Morawiec

Lekarz med. Marek Tazbir



mitr.p.lodz.pl/raman

Uniwersytecki Szpital Kliniczny im. WAM –
Centralny Szpital Weteranów

Prof. dr hab. n. med. Adam Dziki

Uniwersytet Medyczny w Łodzi

Klinika Chirurgii Nowotworów Głowy i Szyi

Oddział Laryngologii Onkologicznej –

Regionalny Ośrodek Onkologiczny

Wojewódzkiego Szpitala Specjalistycznego i
m. Kopernika

Prof. dr hab. n. med. Alina Morawiec-Sztandera

Dr n. med. Izabela Niedźwiecka

Instytut Centrum Zdrowia Matki Polki w Łodzi

Prof. dr hab. n. med. Lech Polis

Dr n. med. Bartosz Polis

GOAL

- **Are we winning the war on cancer? We have been informed that modern anti-cancer treatments are beneficial in terms of increasing overall survival.**
- **However, the overall survival among patients with late-stage cancer has remained steady for more than 40 years.**
- **We agree that the best chance for cancer survival depends on an early diagnosis followed by early surgical removal.**

GOAL

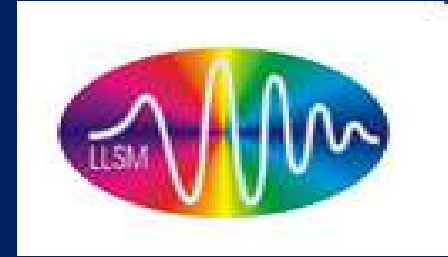


There is an urgent need to improve the conventional methods of cancer diagnostics as it has in fact been found that 70–90% of mammographically detected lesions are found to be benign upon needle biopsy.

Current imaging methods are often limited by inadequate sensitivity, specificity, spatial and spectral resolutions. MRI- limited spatial resolution
FLUORESCENCE- limited spectral resolution

RAMAN-AFM-SNOM- fluorescence imaging and femtosecond spectroscopy

Goal



- We will demonstrate that Raman imaging combined with other methods used in our lab (AFM, SNOM fluorescence microscopy, ultrafast, femtosecond spectroscopy) give new hope for cancer diagnosis. This combination offers unsurpassed spatio-temporal resolution, sensitivity and multiplexing capabilities. We have already begun to translate Raman imaging into a novel clinical diagnostic tool using various endoscopic strategies.

Biomedical applications

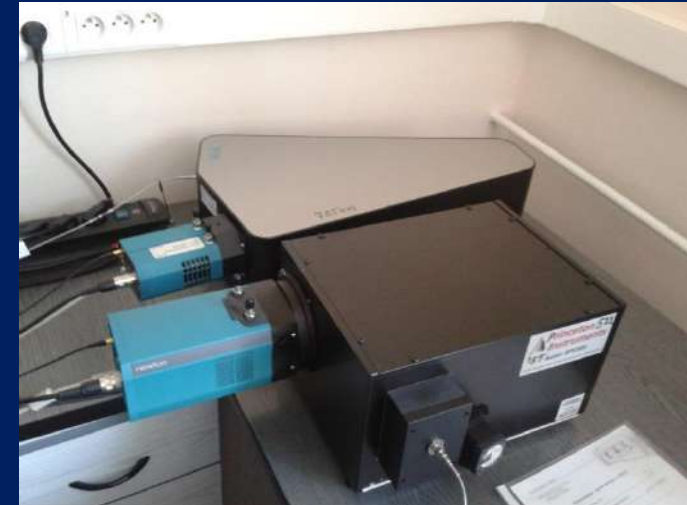
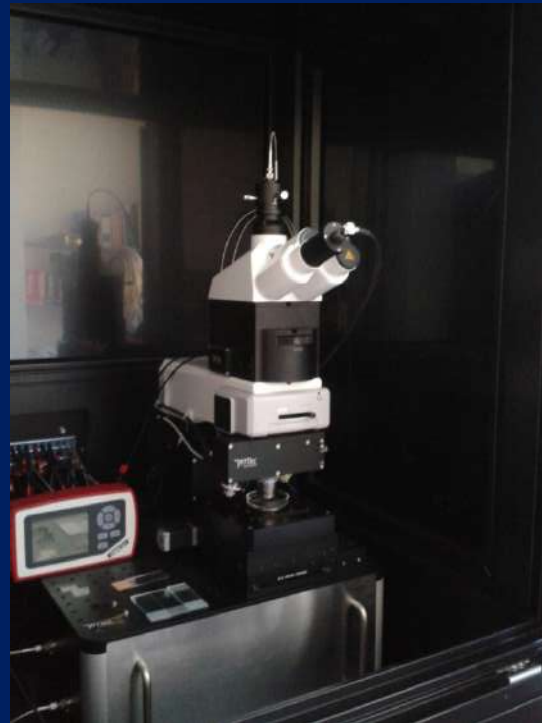


- **High spatial resolution RAMAN IMAGING**
- **SNOM microscopy (far below the diffraction limit, SNOM)**
- **Strong signal enhancement enabling monitoring the genetic and immunological responses in biological systems (SERS COMBINED WITH NANOPARTICLES)**
- **Specificity of interactions (BIOCONJUGATES)**
- **AFM topography, stiffness, adhesion, Young modulus (AFM)**
- **High temporal resolution (FEMTOSECOND PUMP-PROBE SPECTROSCOPY)**

Biomedical applications



- High spatial resolution RAMAN IMAGING
- SNOM microscopy (far below the diffraction limit, SNOM)



Alpha 300 RSA+ (WITec), 355, 532, 785 nm

CONFOCAL RAMAN MICROSCOPY

diffraction limited

$$\delta_{lat} = 0.61 \lambda / NA$$



Laser

Lustra skanujace

$$\delta_{ax} = 2 \lambda n / (NA)^2$$



Skaner w osi Z

**3D imaging and deep profiling
due to confocal configuration**

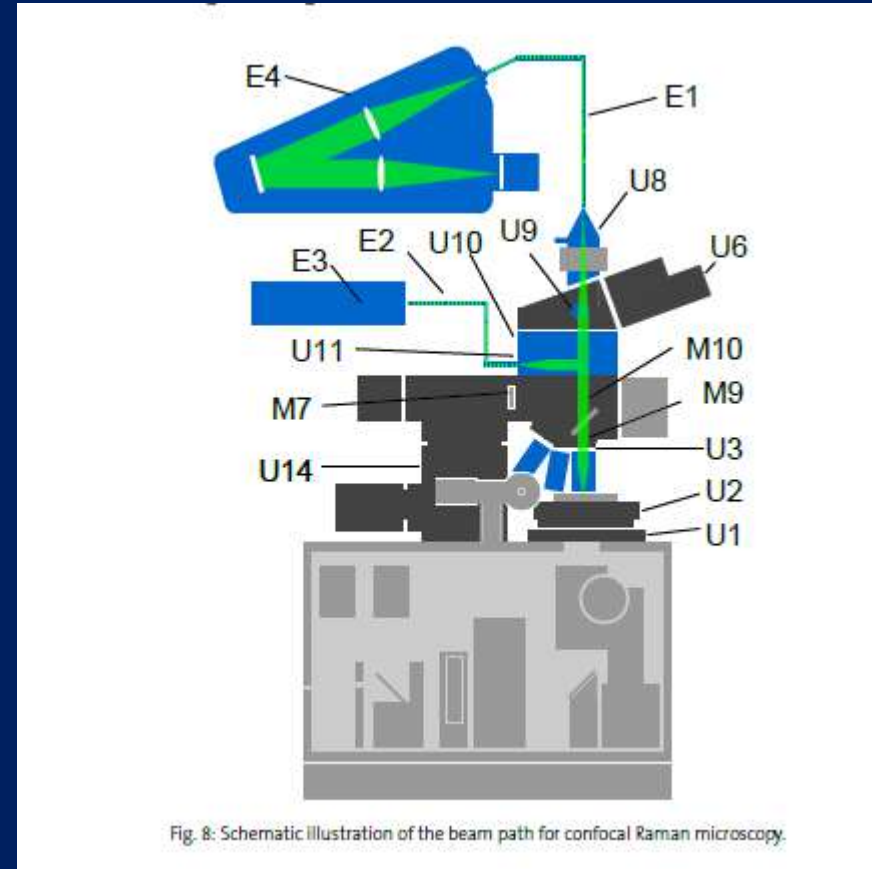
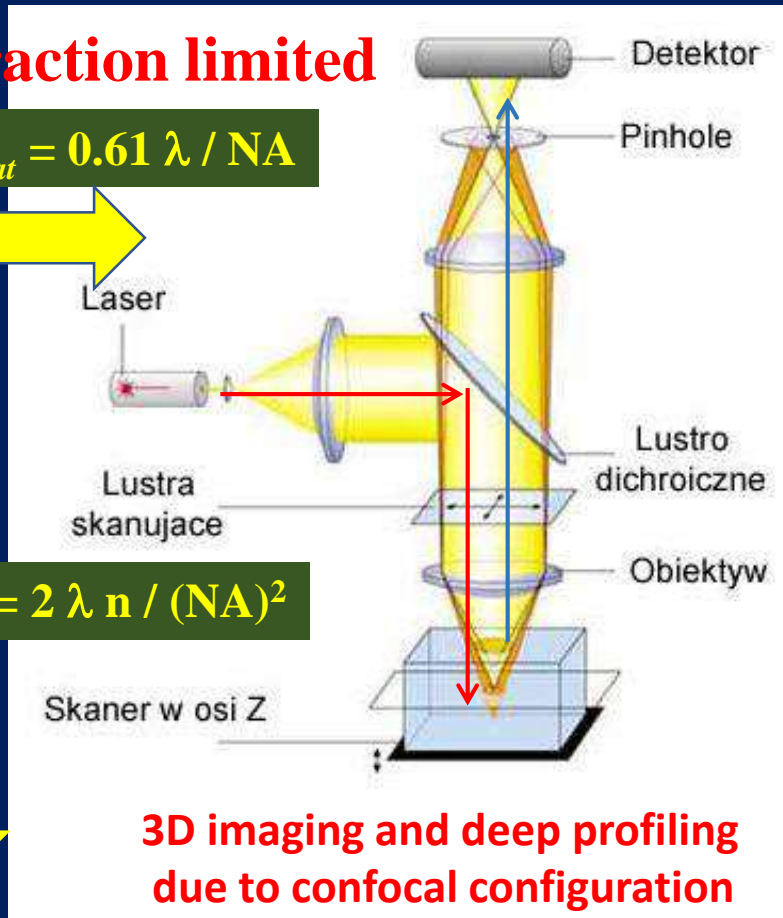


Fig. 8: Schematic illustration of the beam path for confocal Raman microscopy.

1.5 Confocal Raman Microscopy

Confocal microscopy requires a point source (usually a laser), which is focused onto the sample. The reflected light (Raman, fluorescence) is collected with the same objective and focused through a pinhole at the front of the detector (Fig. 3). This ensures that only light from the image focal plane can reach the detector, which greatly increases image contrast and with the proper selection of pinhole size, slightly increases resolution (max. gain in resolution: factor $\sqrt{2}$).

SNOM

Near field microscopy is far below the diffraction limit

3.1 SNOM AC in transmission configuration

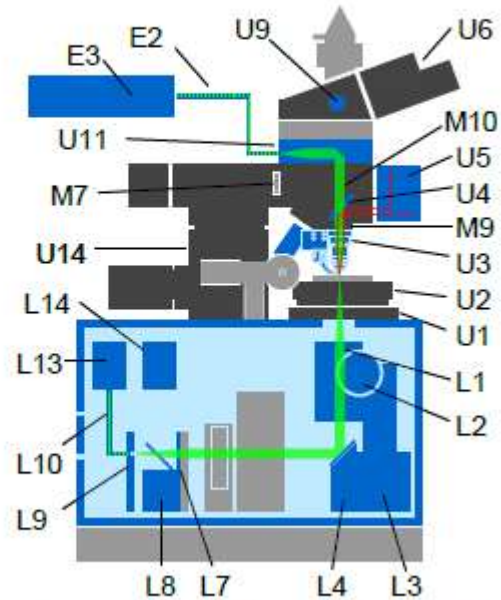
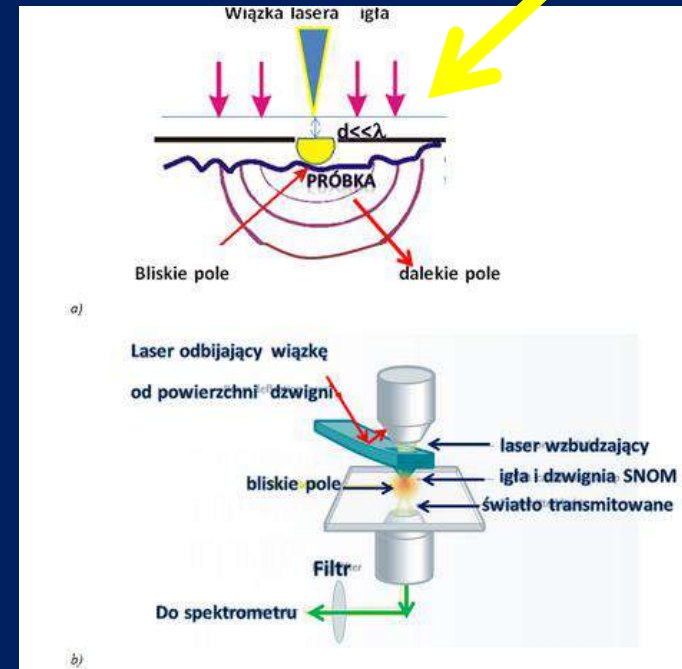


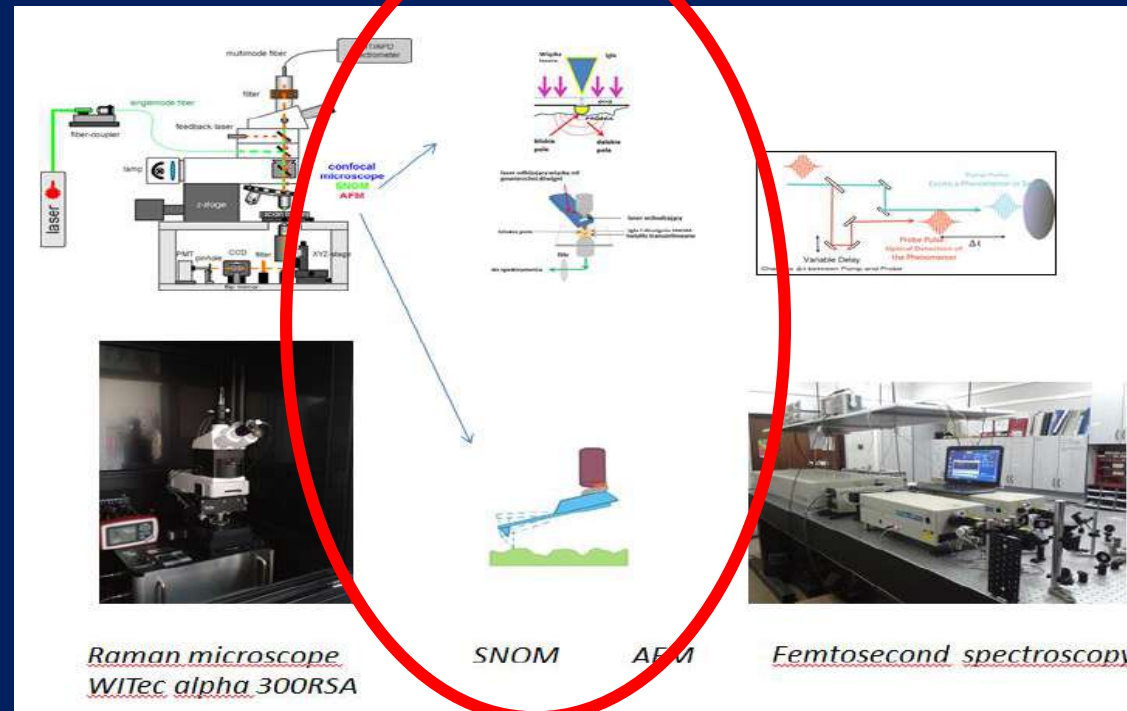
Fig. 5: Schematic illustration of the beam path for Scanning Near-field Optical Microscopy in AC transmission mode.



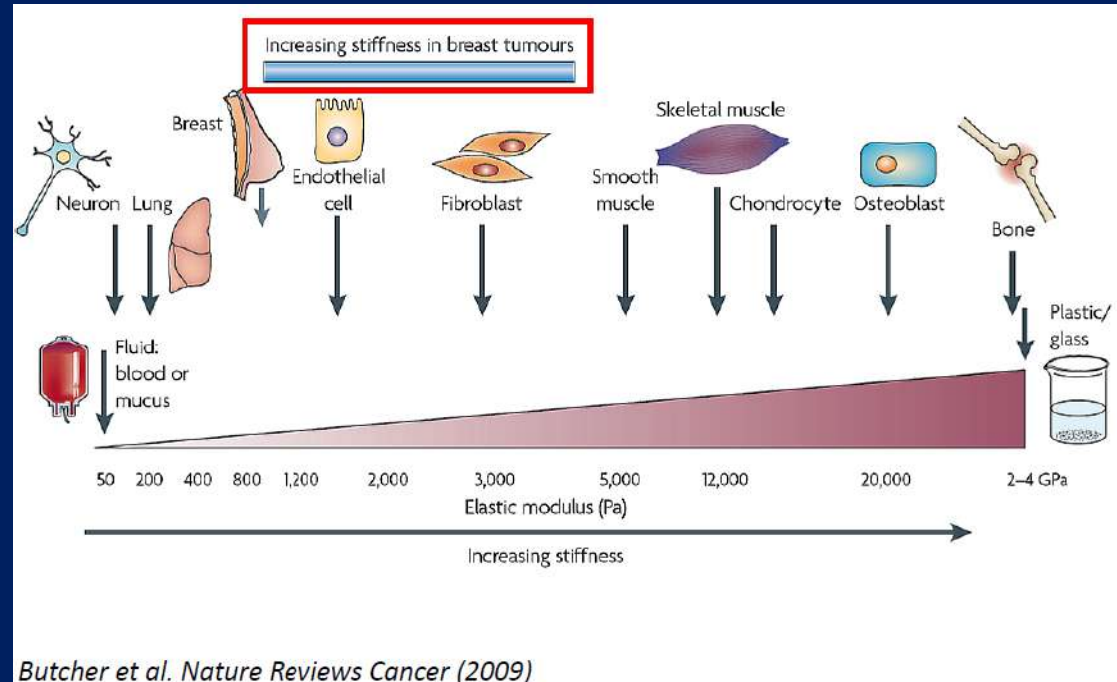
Rys. 3 Ilustracja idei pomiarów SNOM (a) i zasada działania na podstawie instrukcji Witec near-field-Raman imaging, Ulm, Germany (b).

Stiffness and Adhesion of cancer cells

- The biochemistry of cancer is related to second important feature of cells – stiffness and adhesion



How rigid, how sticky, how adherent

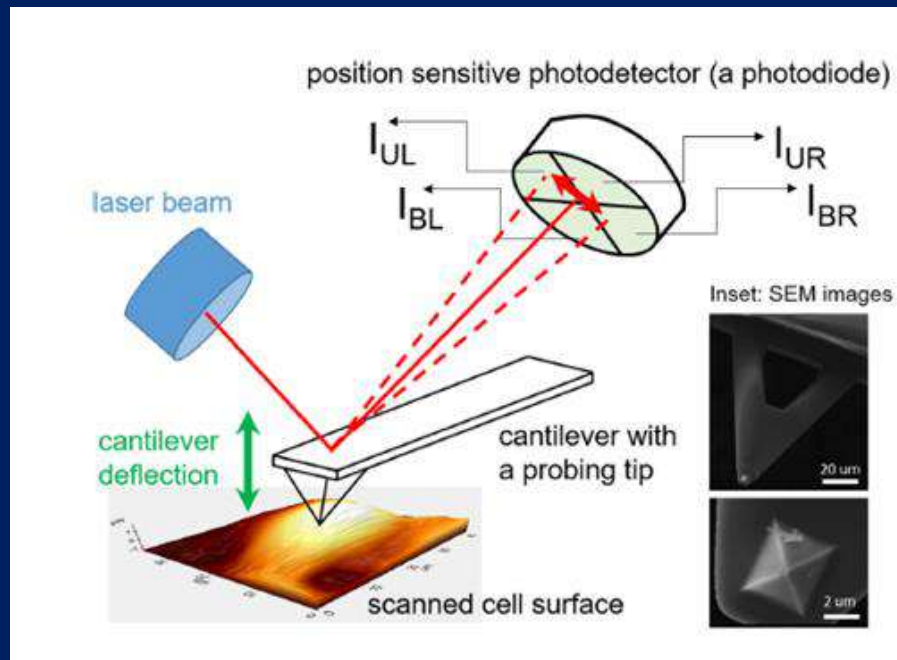


- The AFM technique is much more than just simply microscopy. One can think about AFM tip as a microscopic “finger” with a nanosize apex. Following this analogy, one can use such a finger to touch the surface to feel how rigid
- it is (rigidity force microscope or nanoindenter); one can feel how sticky a surface is (chemical force microscopy);

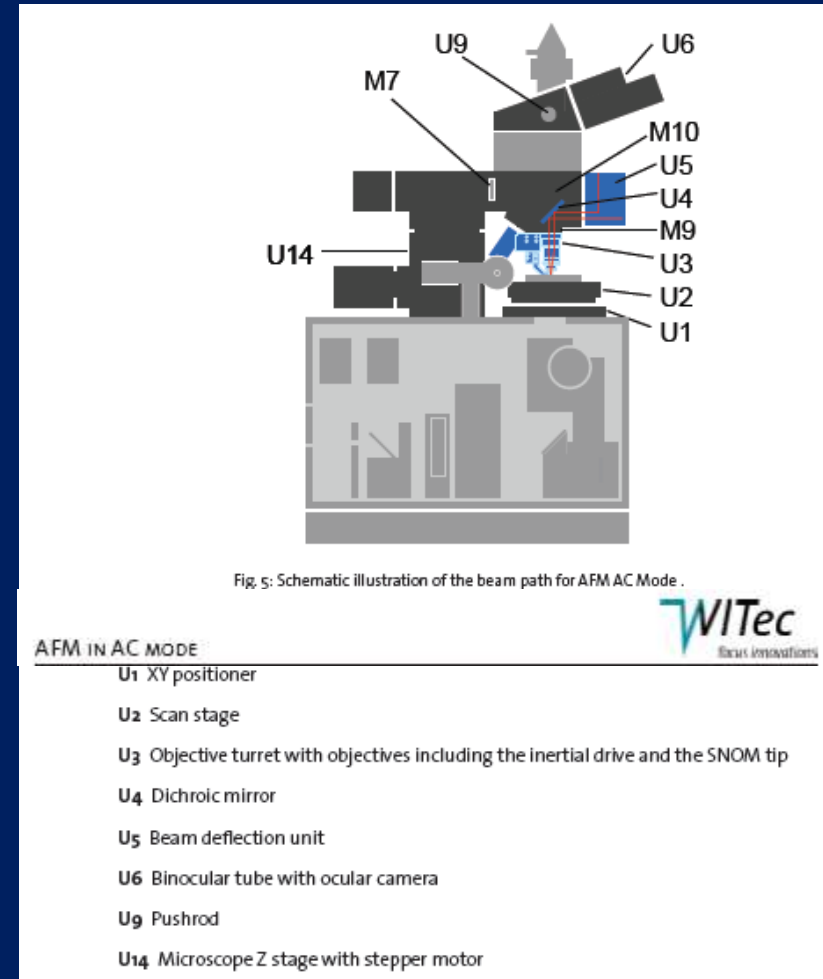
AFM (Atomic force microscopy)

AFM is not based on spatial resolution limited by diffraction. The spatial resolution depends on the tip size, and is far below the diffraction limit.

AFM is a very-high-resolution type of scanning probe microscopy (SPM), with demonstrated resolution on the order of fractions of a nanometer, more than 1000 times better than the optical diffraction limit.



Light-lever detection based on laser and photodiode array



• measures deflection of cantilever

AFM topography for obtaining surface profiles

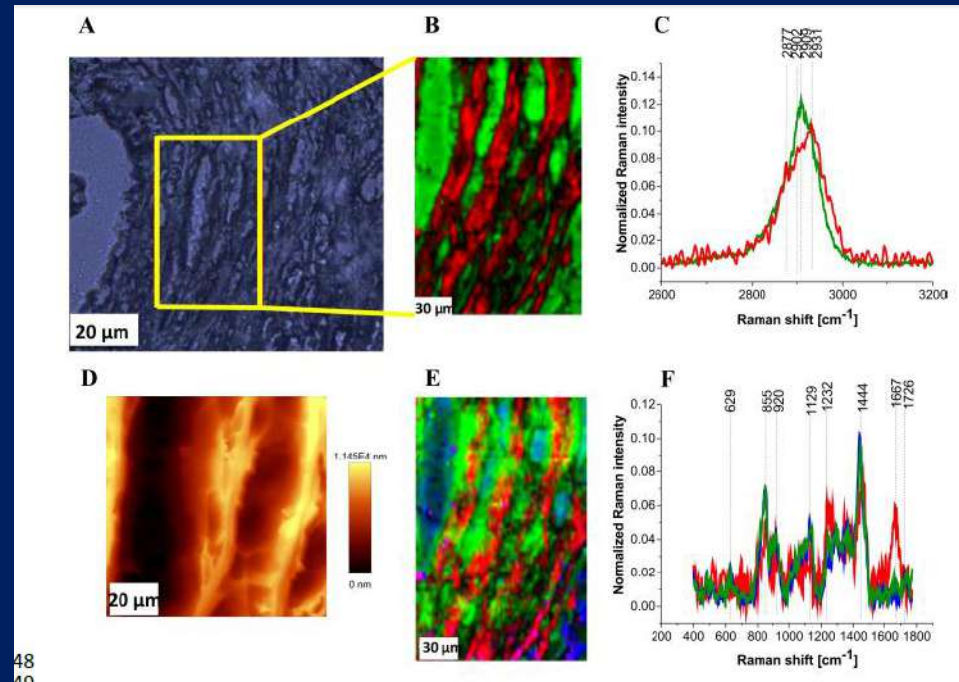
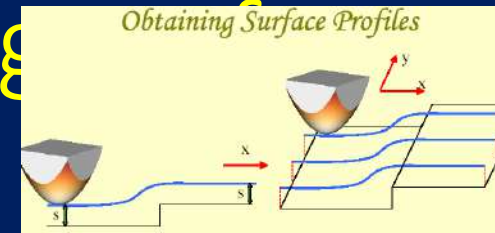


Fig. 6 Distribution of the glycans (green), lipids (blue) and protein (red) in the human breast tumor tissue, the white light microscopy image (A), Raman image (150 μm x 230 μm) obtained from the basis analysis (B) and Raman spectra (C) in the high frequency spectral region. AFM image (D), Raman image obtained from the basis analysis (E) and Raman spectra (F) in the fingerprint region of the tumor breast tissue (Patient P155, Infiltrating adenocarcinoma grade WHO according to Elston and Ellis modification G2), integration time for Raman images 0.5 s in the high frequency region and 1 s in the low frequency region, resolution step 0.5 μm, laser excitation power 10 mW. The line colors of the spectra correspond to the colors of the Raman maps.

Force Mode

- Force mode not an imaging mode; it is used to measure
- forces acting between AFM tip and the surface of interest
- at a specific point. In contrast to the previous modes, the
- cantilever does not move in lateral direction. The scanner
- goes up and down, elevating and approaching the cantilever
- to the surface. As a result, the image shown in Figure 2 is
- a typical example of what is recorded. The force F of the
- bending of the cantilever (vertical axis) is plotted against
- the vertical position z of the sample. When the tip is far
- away from the surface, there is no deflection, and consequently,
- the force is equal to zero . When the z position of the sample
- increases (the sample is moved up by the scanner, Fig. 1),
- the tip-sample distance decreases. At some point, the tip
- touches the sample (position of contact). After that, the tip
- and sample move up together. This part of the force curve
- is called the *approaching curve*. At some point,
- which can be controlled by AFM operator, the sample stops
- and retracts down. The force curve recorded when the sample
- is known as the *retracting curve*. During retraction the surface
- viscous and elastic properties. This typically results in hysteresis
- between the approaching and retracting curves, as
- shown in Figure 2.

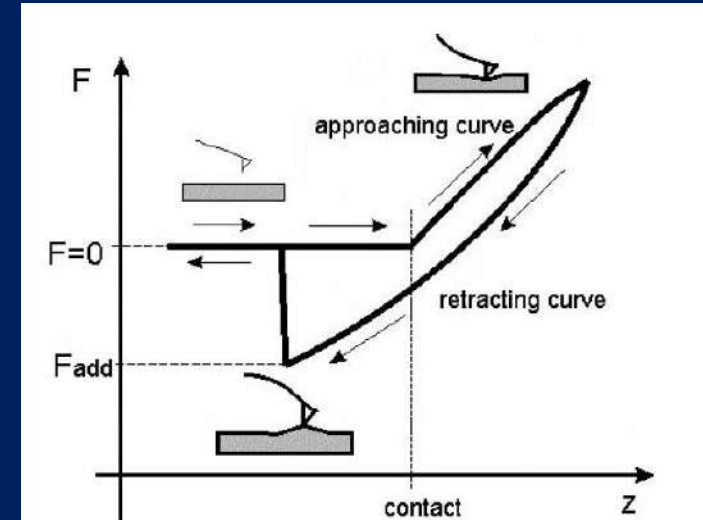
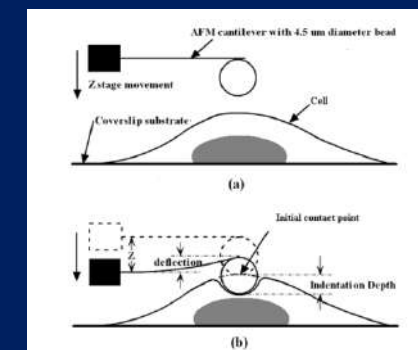
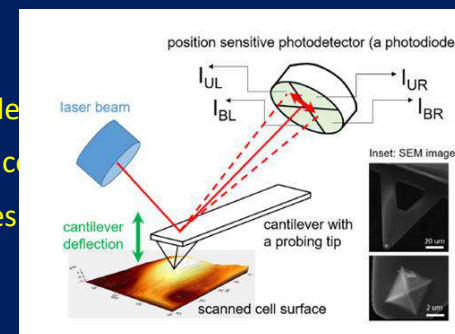


Figure 2. A typical force–distance curve recorded by AFM in force mode. Both the approaching and retracting curves are shown.



ADHESION

- One more interesting feature of the retracting curve is the non-zero force required to disconnect the tip from the surface. This is the so-called *adhesion force*. It appears due to weak forces (such as van der Waals forces) acting between the tip and surface while in contact.
- DPFM , WITEC , ULM GERMANY

Int. J. Mol. Sci. 2015, 16

To calculate the stiffness of the sample the information on the slope of the rising part of the DPFM curve is needed. Fig. II. presents the force-distance curve recorded by DPFM mode, the fitting range (in light blue) and the fitting curve (in dark blue).

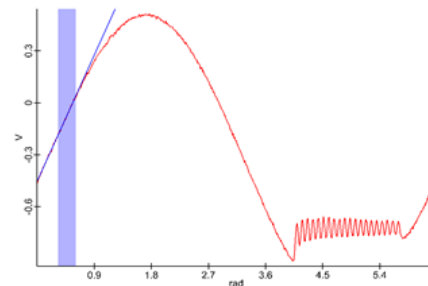


Fig. II. The force-distance curve recorded by DPFM, the selected range of interest with the fitting curve.

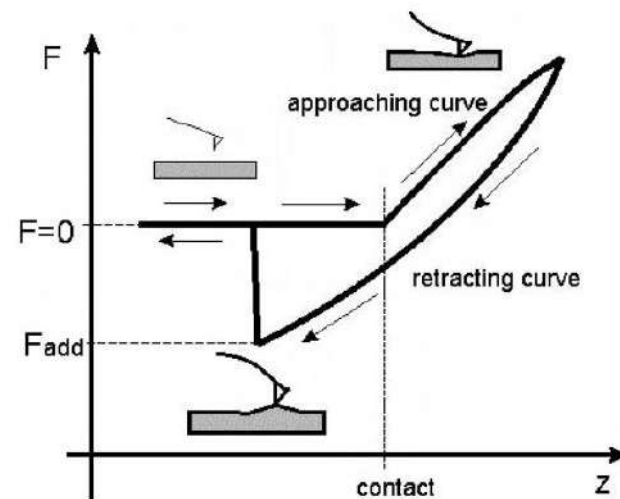


Figure 2. A typical force-distance curve recorded by AFM in force mode. Both the approaching and retracting curves are shown.

AFM stiffness and adhesion of cells and tissue by DPFM

DPFM (digital pulsed Force Mode) is a non-resonant, intermediate contact mode. During DPFM measurement the cantilever oscillates at frequency far below the resonance, typically in the range of 0.01-10kHz. The amplitude of the cantilever oscillation is also adjustable in the range 50-500nm. As a result of the measurement one can obtain a set of force-distance curves characterizing nanomechanical properties of the sample.

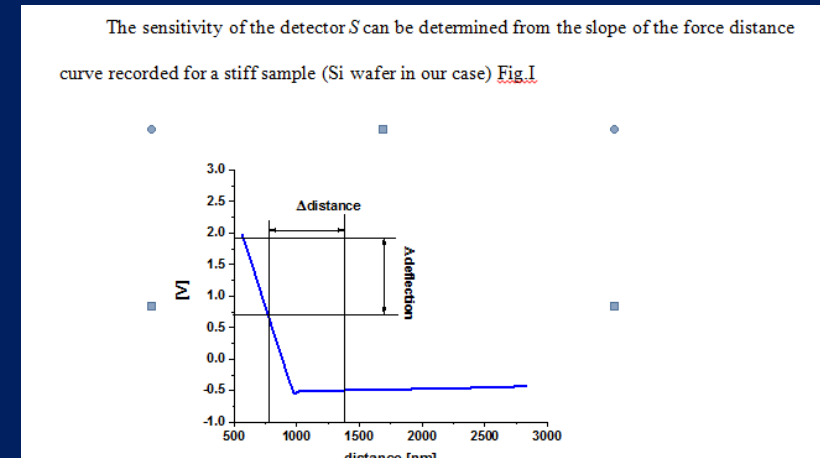


Fig 6 Typical deflection curve for the normal breast tissue in volts vs relative position z between the tip and the sample. Typical load force- versus-displacement curves measured for the normal breast tissue (c) the tumor mass tissue (d), and CaF_2 support that deliver the relation between load force F and the indentation, calculated as a difference between these curves for normal breast tissue (e) and from the tumor mass (f).

AFM stiffness and adhesion of cells and tissue by DPFM

To calculate the stiffness of the sample the information on the slope of the rising part of the DPFM curve is needed. Fig. II. presents the force-distance curve recorded by DPFM mode, the fitting range (in light blue) and the fitting curve (in dark blue).

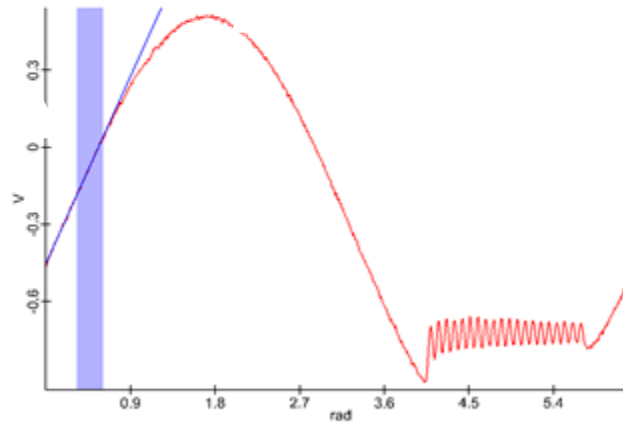
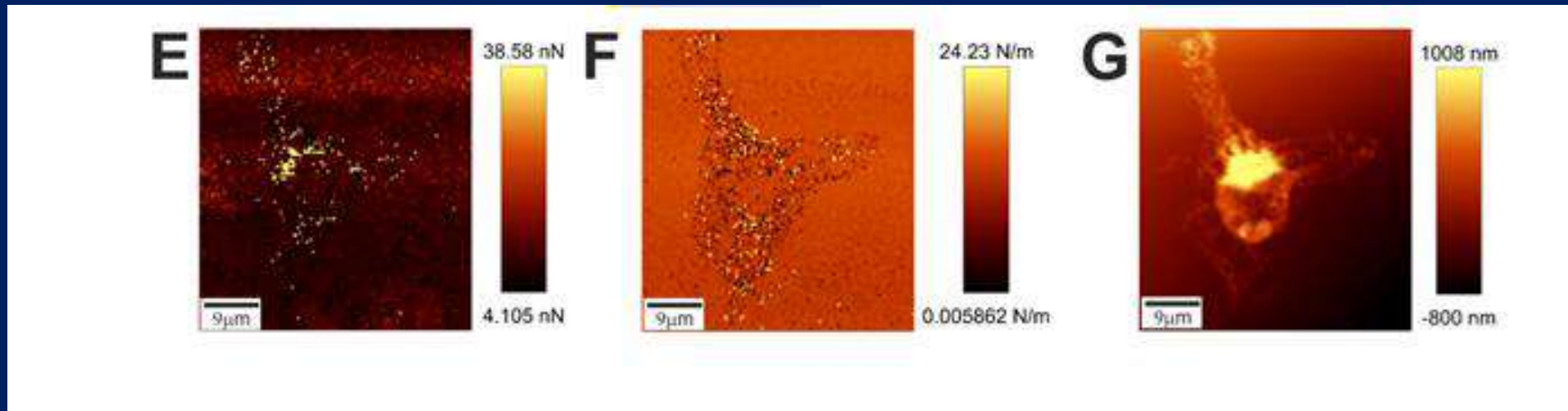


Fig. II. The force-distance curve recorded by DPFM, the selected range of interest with the fitting curve.

Using these force curves (sometime called *indentation curves*), one can easily calculate the *stiffness*, which is defined as a derivative of force F with respect to penetration z (indentation), dF/dz .

AFM stiffness and adhesion of cells and tissue by DPFM

U-87 MG cell (glioblastoma - brain)



adhesion image (E), stiffness image (F) and topography image (G) of air-dried cell.

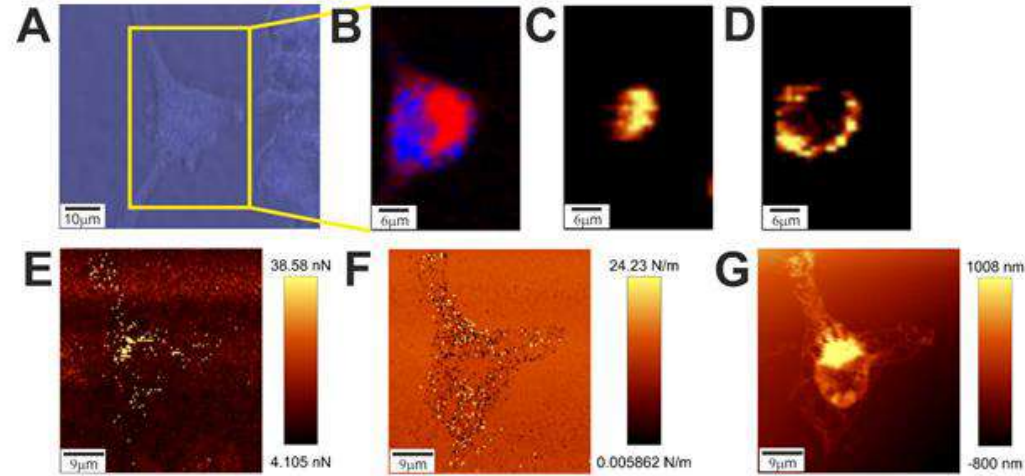


Fig 4. Microscopy image (A), Raman image (red-proteins, blue-lipids) (B), fluorescence images of Hoechst 33342 (C) and Oil Red O (D) of a living U-87 MG cell, adhesion image (E), stiffness image (F) and topography image (G) of air-dried cell.

Microscopy image (A), Raman image (red-proteins, blue-lipids) (B), fluorescence images of Hoechst 33342 (C) and Oil Red O (D) of a living U-87 MG cell, adhesion image (E), stiffness image (F) and topography image (G) of air-dried cell.

The Young's modulus

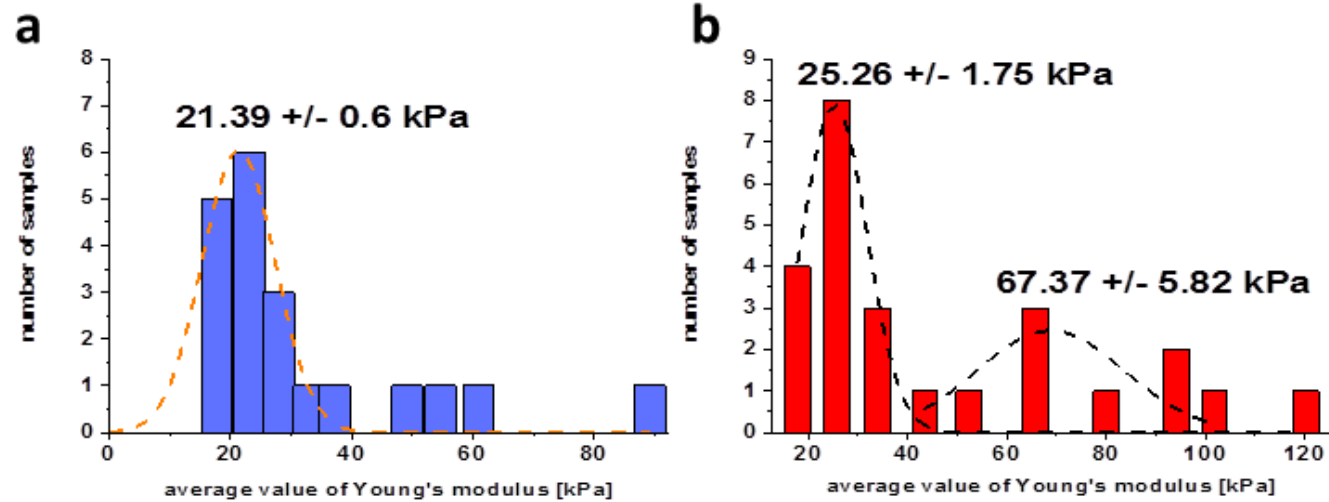


Fig. 7 Young's moduli (kPa) for a normal (a) and cancerous (b) human breast tissue.

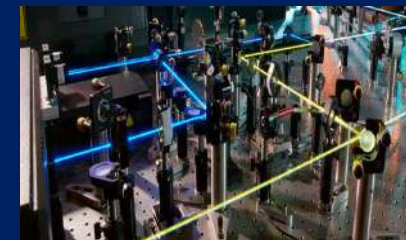
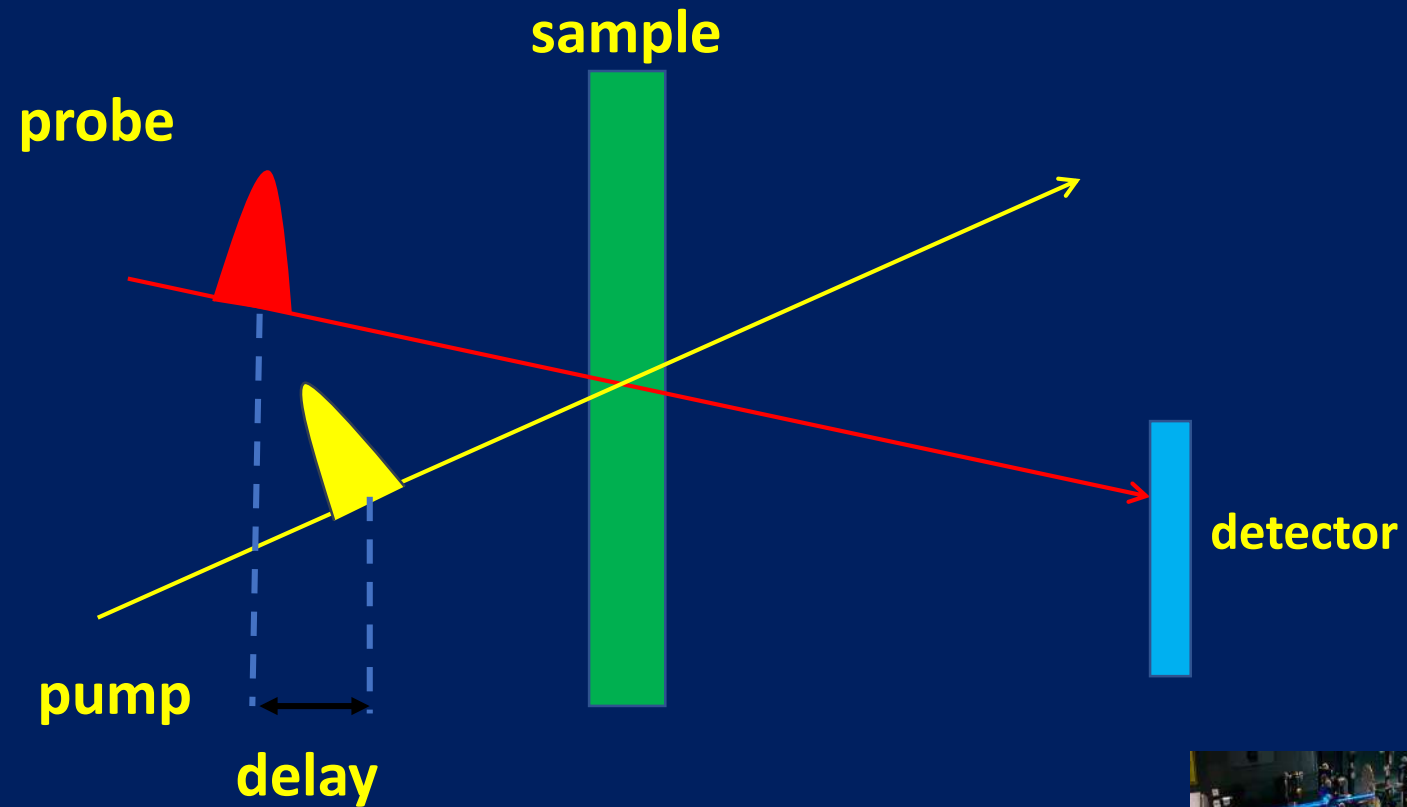
Biomedical applications

- **High spatial resolution (far below the diffraction limit, SNOM)
RAMAN IMAGING**
- **High temporal resolution (FEMTOSECOND PUMP-PROBE
SPECTROSCOPY)**





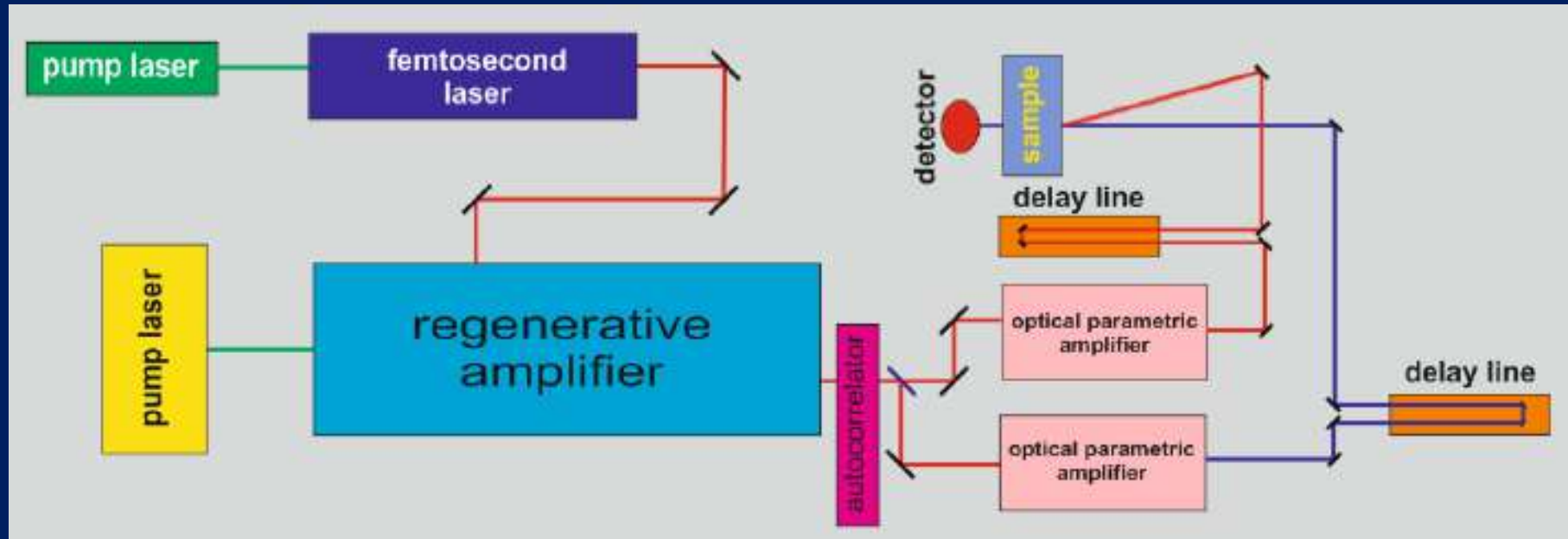
Pump-probe measurements



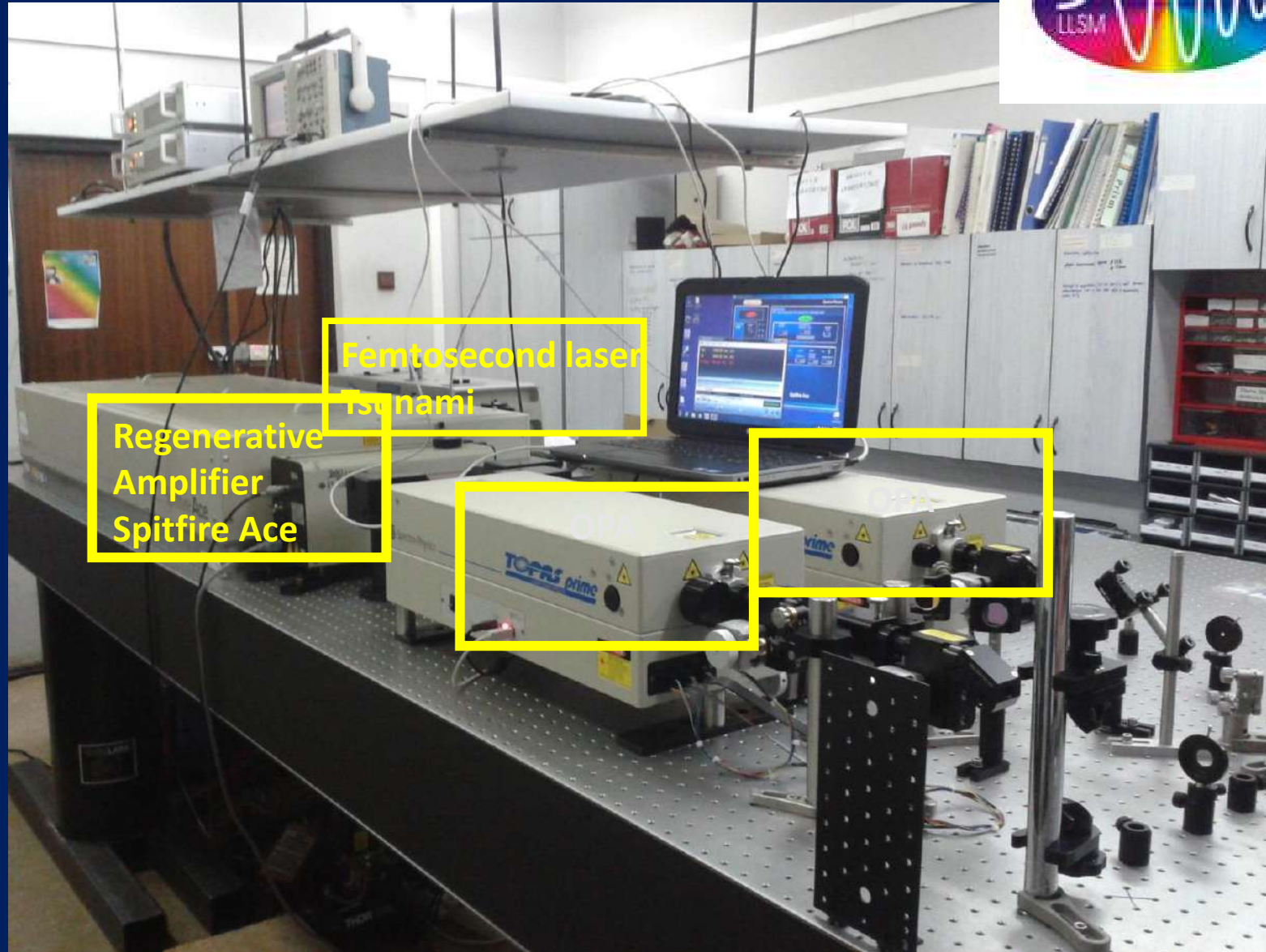
unsurpassed temporal resolution

femto

DYNAMICS



Recently developed techniques of ultrafast nonlinear vibrational spectroscopy allow a much more effective attack on this problem of dynamics in biological systems.



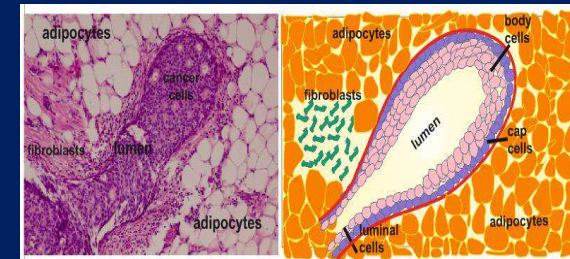
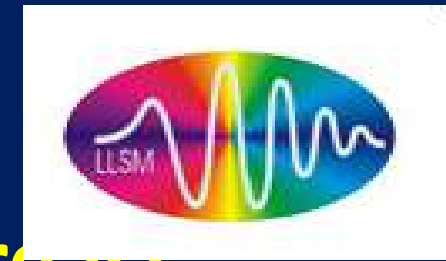
Femtosecond laser
Tsunami

Regenerative
Amplifier
Spitfire Ace

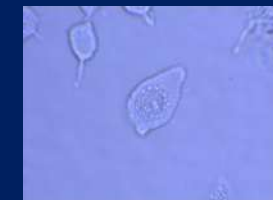
OPA
TOPAS prime

What?

Human normal and cancerous breast tissue, brain, neck and head , intestine tissues



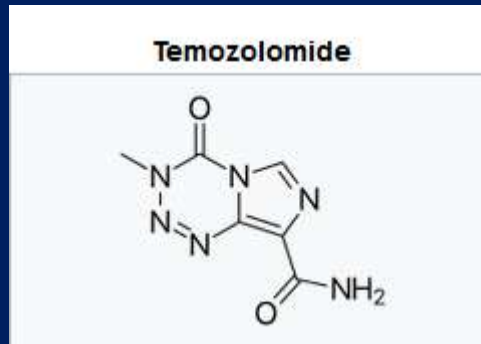
Cell human Lines: breast and brain normal (MCF-10A,) and cancerous epithelial and glial cells (MCF-7, MDA-MB-231, NHA Astrocytes CC2565) and glioblastoma (U87MG)



Drugs (temodal,erlotinib) and Photosensitizers in cancer therapy

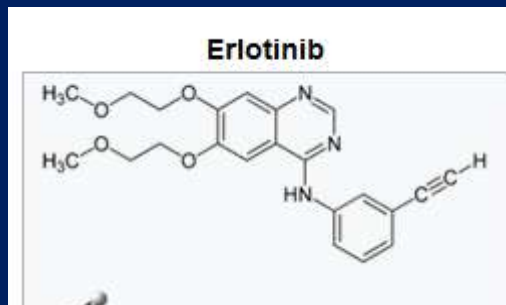


Agents used as a treatment of some brain cancers; as a second-line treatment for astrocytoma and a first-line treatment for glioblastoma multiforme



Mechanism of action

The therapeutic benefit of temozolomide depends on its ability to alkylate/methylate DNA, which most often occurs at the N-7 or O-6 positions of guanine residues. This methylation damages the DNA and triggers the death of tumor cells. However, some tumor cells are able to repair this type of DNA damage, and therefore diminish the therapeutic efficacy of temozolomide,



Mechanism

Erlotinib is an epidermal growth factor receptor inhibitor (EGFR inhibitor). Erlotinib specifically targets the epidermal growth factor receptor (EGFR) tyrosine kinase, which is highly expressed and occasionally mutated in various forms of cancer. It binds in a reversible fashion to the adenosine triphosphate (ATP) binding site of the receptor.[[]

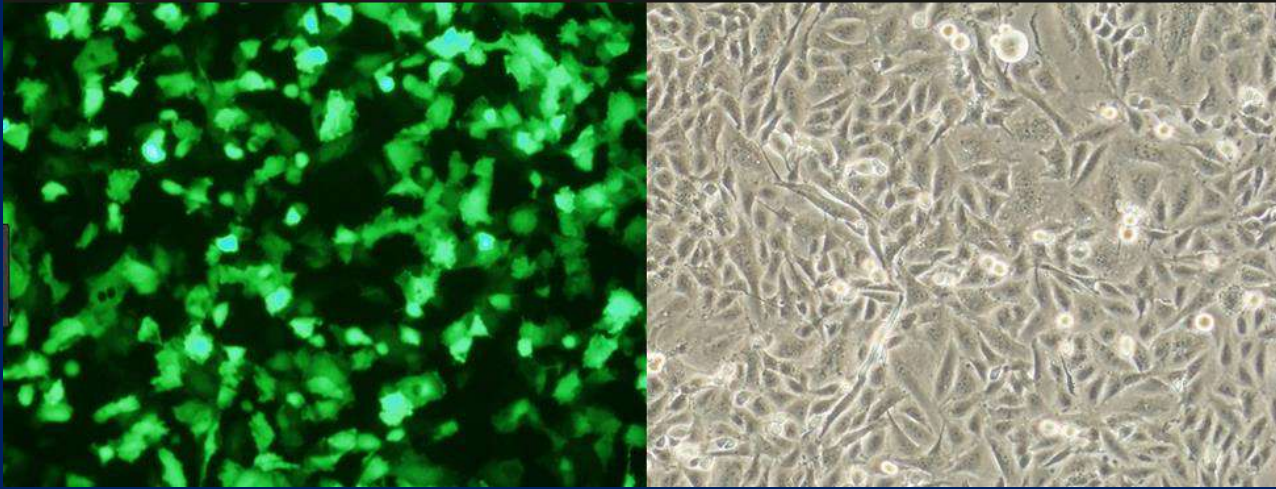
Brain cell lines



Normal Human Astrocytes (NHA) can be used to study the function of the central nervous system and how neural cells interact. Astrocytes are glial cells found in the brain and spinal cord that play a critical role in maintenance, support, and repair of nervous tissue

- **Applications:**
 - Astrocyte-mediated neurotoxicity
 - Neurogenesis research
 - Injury
 - Drug development
 - Parkinson's disease
 - Alzheimer's disease

glioblastoma (U87MG)



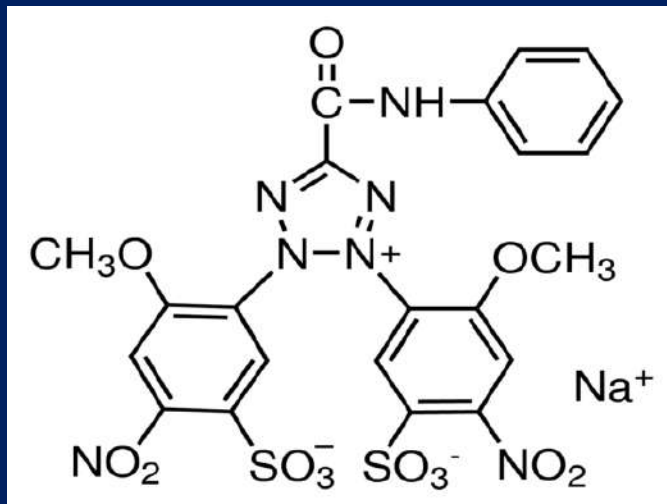
In cell biology, *U87* is a human primary *glioblastoma* cell line formally known as *U-87 MG*. It has epithelial morphology.

Culture Medium

EMEM (EBSS) + 2mM Glutamine + 1% Non Essential Amino Acids (NEAA) + 1mM Sodium Pyruvate (NaP) + 10% Foetal Bovine Serum (FBS).

Cell viability

Cell viability was estimated by Cell Proliferation Kit (XTT based, no. 20-300-1000) following manufacture's instruction (Biological Industries Israel Beit Haemek Ltd.). Briefly seeded cells were mixed with prepared XTT working solution for 3 and 5 hours at 37°C under 5% CO₂ and absorbance value obtained at 450 nm with a reference correction at 690 nm using Synergy HT Multi-Mode Microplate Reader (BioTek).



XTT (sodium 3'-[1-[(phenylamino)-carbony]-3,4-tetrazolium]-bis(4-methoxy-6-nitro)benzene-sulfonic acid hydrate)

Principle

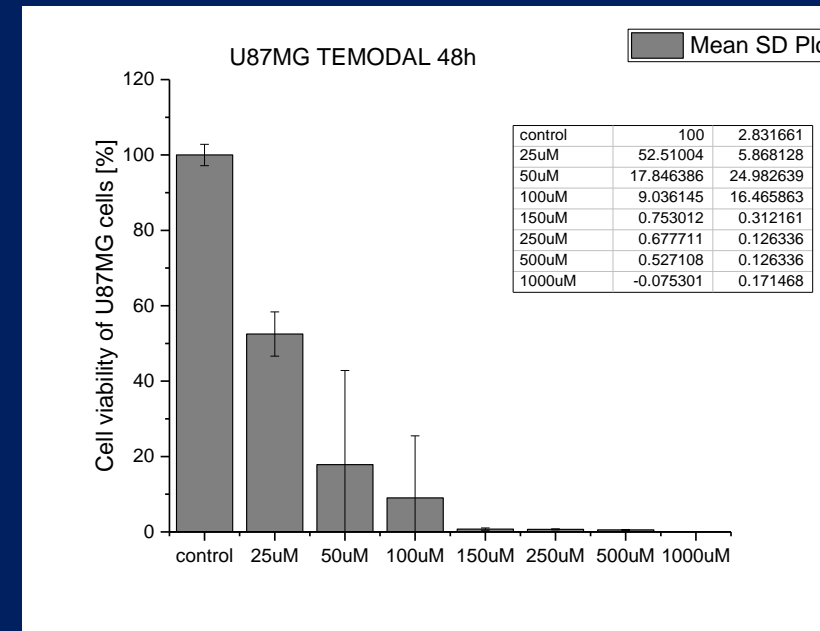
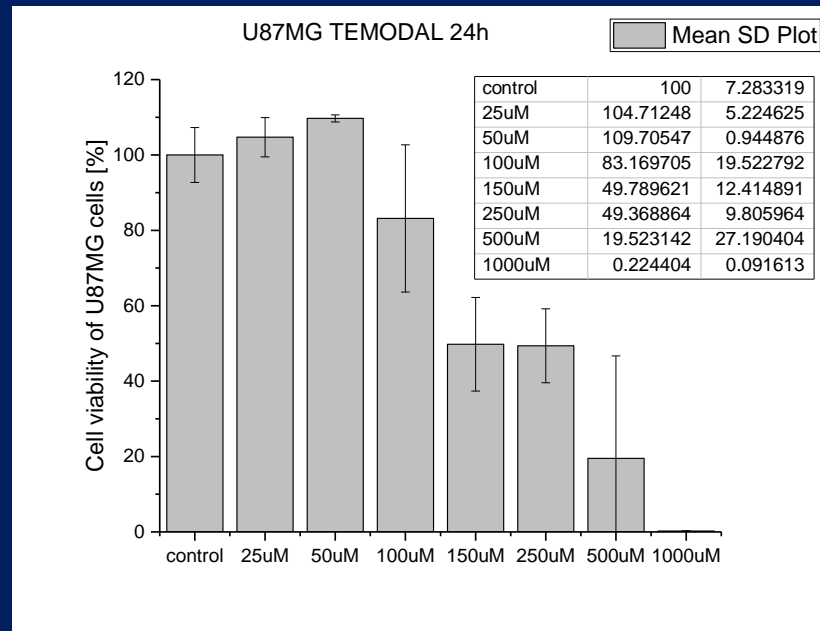
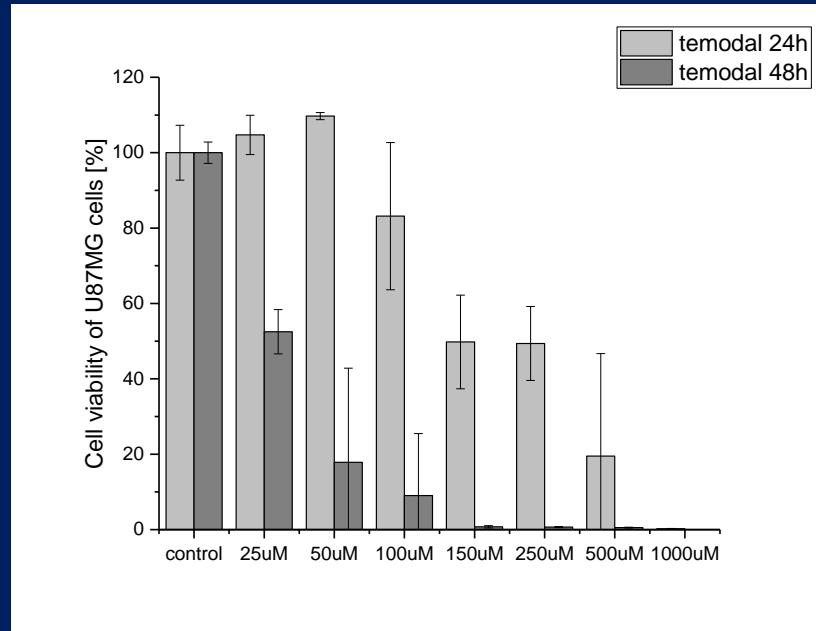
In living cells, XTT is metabolically reduced to produce a colorimetric, water-soluble formazan product.

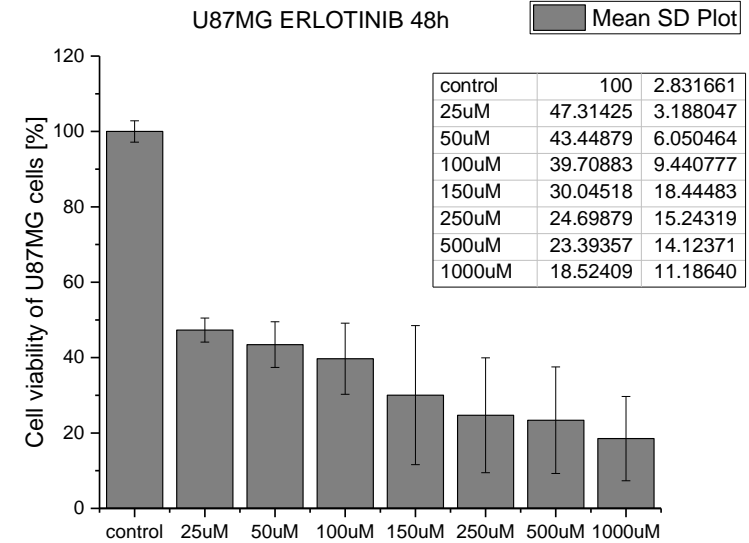
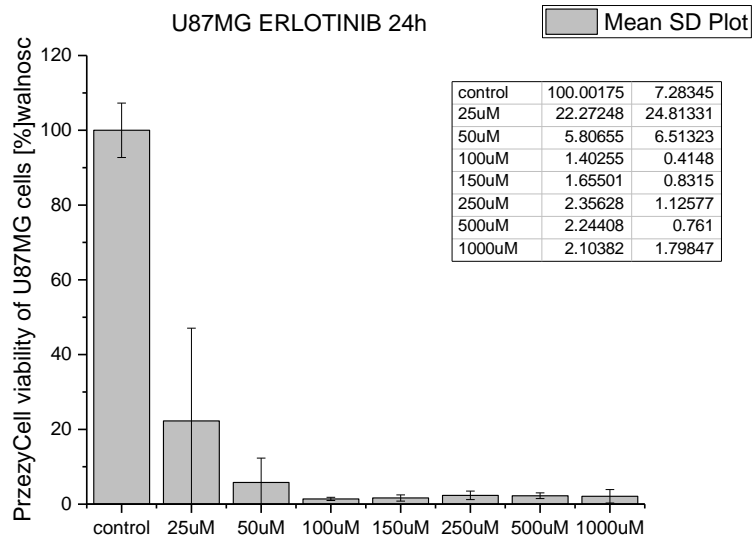
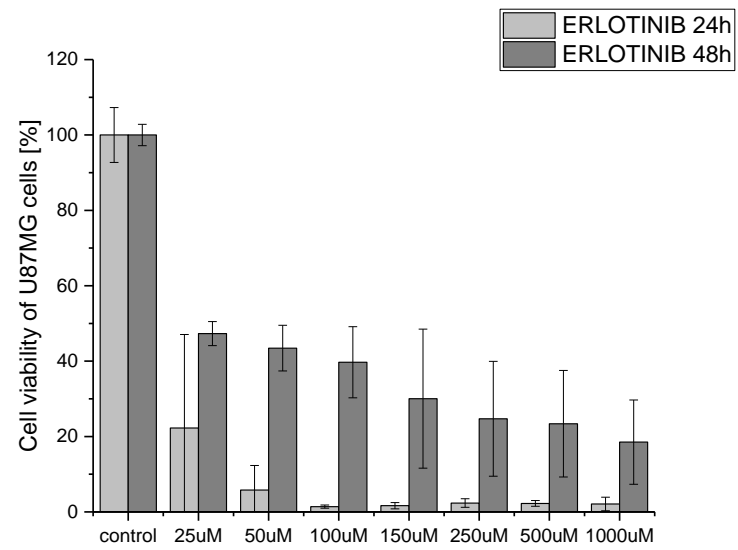
Biochem/physiol Actions

XTT (sodium 3'-[1-[(phenylamino)-carbony]-3,4-tetrazolium]-bis(4-methoxy-6-nitro)benzene-sulfonic acid hydrate) is acted upon by dehydrogenases present in metabolically active cells. This produces water soluble formazan, which is a highly colored product. Thus, it offers an advantage in colorimetric proliferation assays, as opposed to MTT, as the product is already soluble and no formazan crystals are formed.^[1]

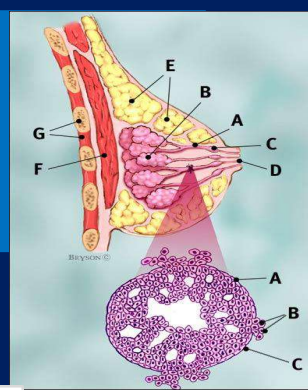
General description

XTT (sodium 3'-[1-[(phenylamino)-carbony]-3,4-tetrazolium]-bis(4-methoxy-6-nitro)benzene-sulfonic acid hydrate) is a tetrazolium salt, which forms water-soluble formazan on bio-reduction



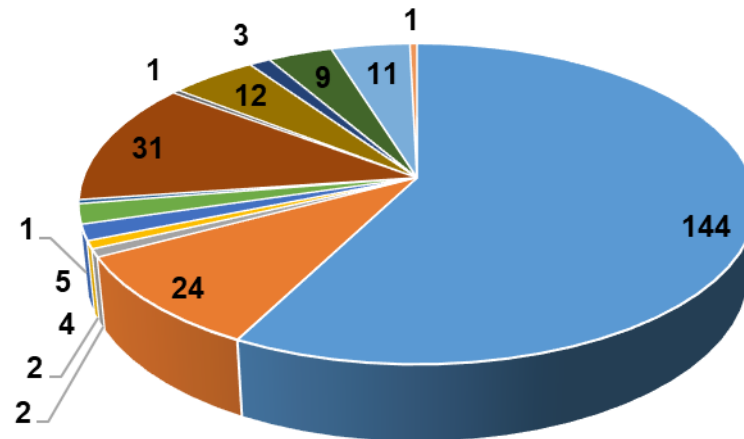


Patients Statistics- breast



❖ 250 patients

Types of breast tumors n=250



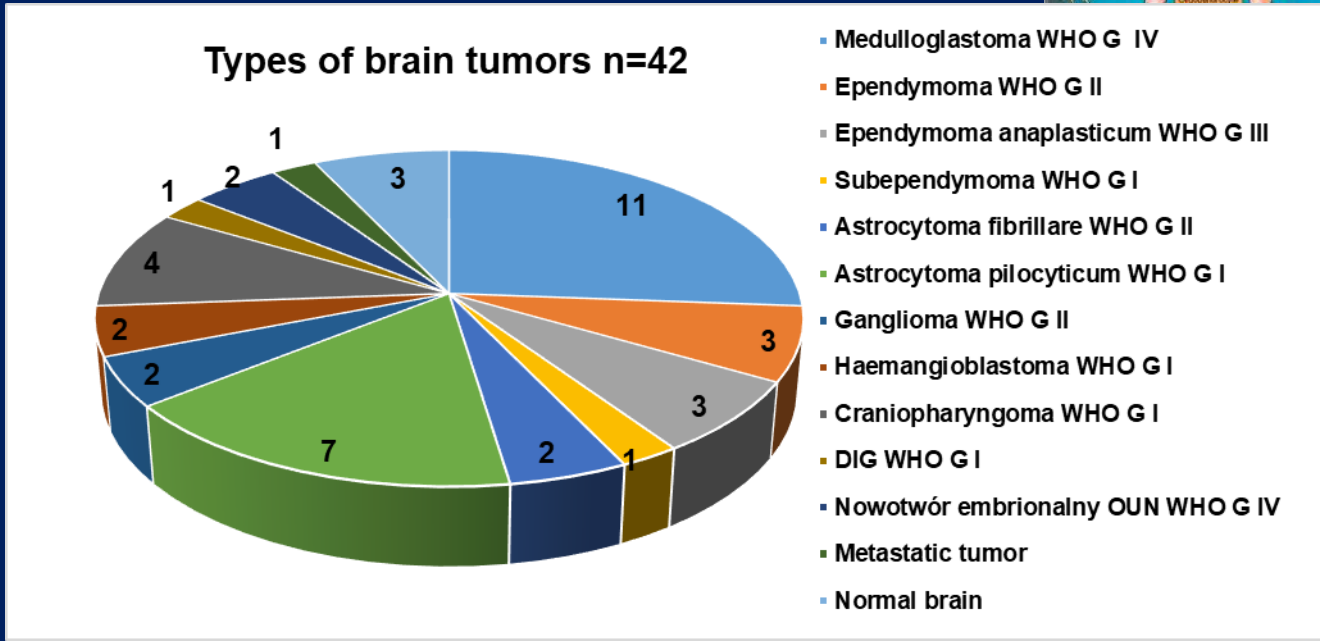
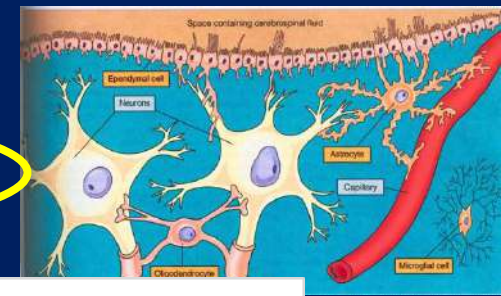
- Carcinoma ductale infiltrans
- Carcinoma lobulare infiltrans
- Carcinoma ductale infiltrans + carcinoma lobulare infiltrans
- Carcinoma multifocale infiltrans
- Papillare intracysticum noninvasium
- Carcinoma mucinosum sinistri
- Carcinoma intraductale
- Fibroadenoma
- Carcinoma metaplasticum
- Dysplasia benigna
- Hyperplasia ductalo-lobularis
- Adenosis
- Leasio-fibroso-cysticum
- Proliferating breast disease

The pathology reports indicated that 70% of the cancer samples were ductal carcinomas; the remaining samples were lobular or untyped mammary carcinomas, metastases were found in 60% of patients

In this lecture we will deal with epithelial cancer types. Most cancers have epithelial origin and they represent approximately 80-85% of all cancers.³⁸

Patients Statistics-brain

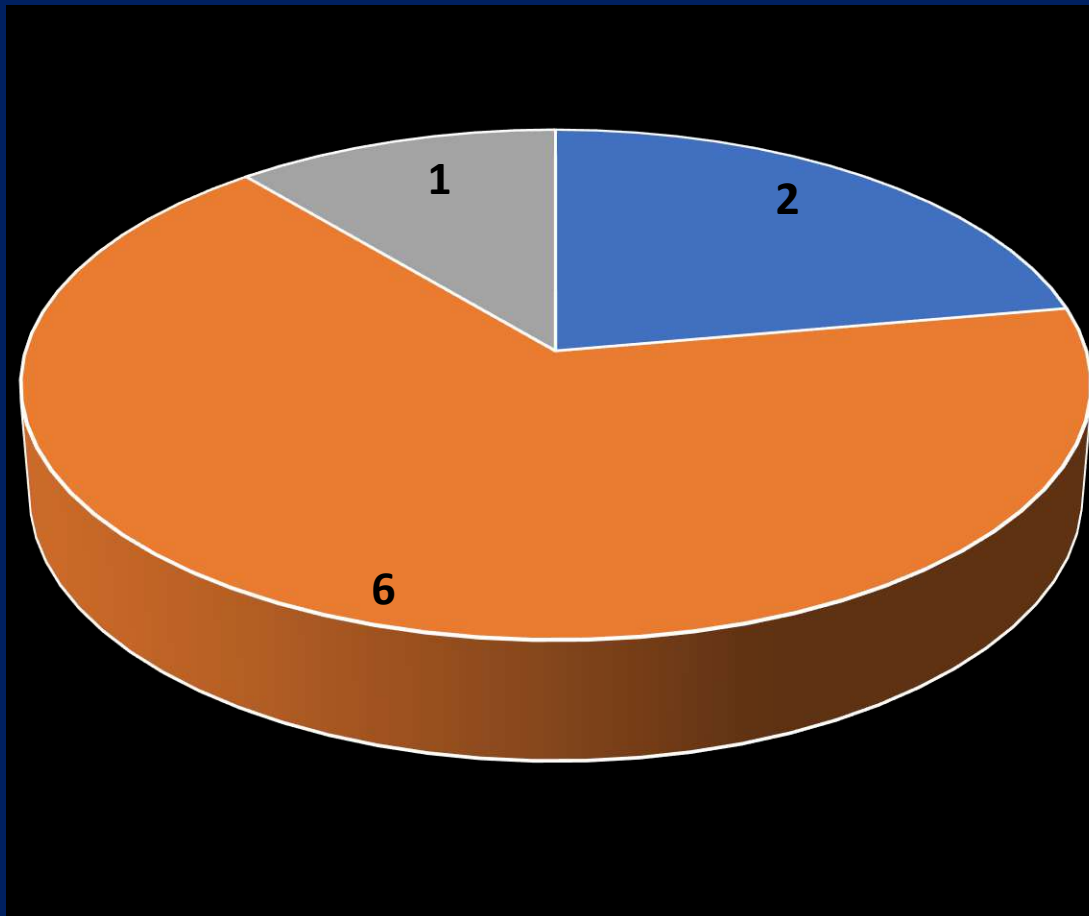
42 patients



The epithelium cells cover the body and lines in the majority of organs, such as the milk ducts in the breast gland or the digestive tract and are involved in the absorption of food, although it is just only one of the many features of epithelia.³⁷ The cells lining the brain called ependymocytes, are a type of glial cells, covering the walls of the ventricular system of the brain: the brain ventricles and the central tube of the spinal cord. They are involved in the exchange of material between the cerebrospinal fluid and nervous tissue and, unlike epithelial cells, have no basal membrane. Despite these differences, for simplicity both groups will be called epithelial cells in this proposal.

Patients Statistics- intestine

9 patients



□ rectal tumor

□ large intestine

□ small intestine passing in the large intestine tumor infiltration at ileocecal valve

Patients Statistics-head and neck

14 patients



The epithelium cells cover the body and lines in the majority of organs, such as the milk ducts in the breast gland or the digestive tract and are involved in the absorption of food, although it is just only one of the many features of epithelia.³⁷ The cells lining the brain called ependymocytes, are a type of glial cells, covering the walls of the ventricular system of the brain: the brain ventricles and the central tube of the spinal cord. They are involved in the exchange of material between the cerebrospinal fluid and nervous tissue and, unlike epithelial cells, have no basal membrane. Despite these differences, for simplicity both groups will be called epithelial cells in this presentation.

HOW DOES RAMAN SPECTROSCOPY AND IMAGING BENEFIT CANCER RESEARCH?

- RAMAN BIOMARKERS OF CANCER
- RAMAN OPTICAL BIOPSY
- the emergence of Raman-driven proteomics, lipidomics, glycomics, and epigenetics research
- POLARITY OF CELLS
- EPIGENETIC MODIFICATIONS
- GLYCOME PROFILE

HOW DOES RAMAN SPECTROSCOPY
AND IMAGING BENEFIT CANCER
RESEARCH?

- **RAMAN BIOMARKERS OF
CANCER**

Cancer biodiagnostics. Raman biomarkers

- We have shown that commonly disregarded in the past alterations in lipid- and retinyl esters-associated pathways encountered in tumors are very important in cancer development.



New look inside human breast ducts with Raman imaging



2016

Analytica Chimica Acta

Volume 909, 25 February 2016, Pages 91–100



New look inside human breast ducts with Raman imaging.
Raman candidates as diagnostic markers for breast cancer prognosis: Mammaglobin, palmitic acid and sphingomyelin

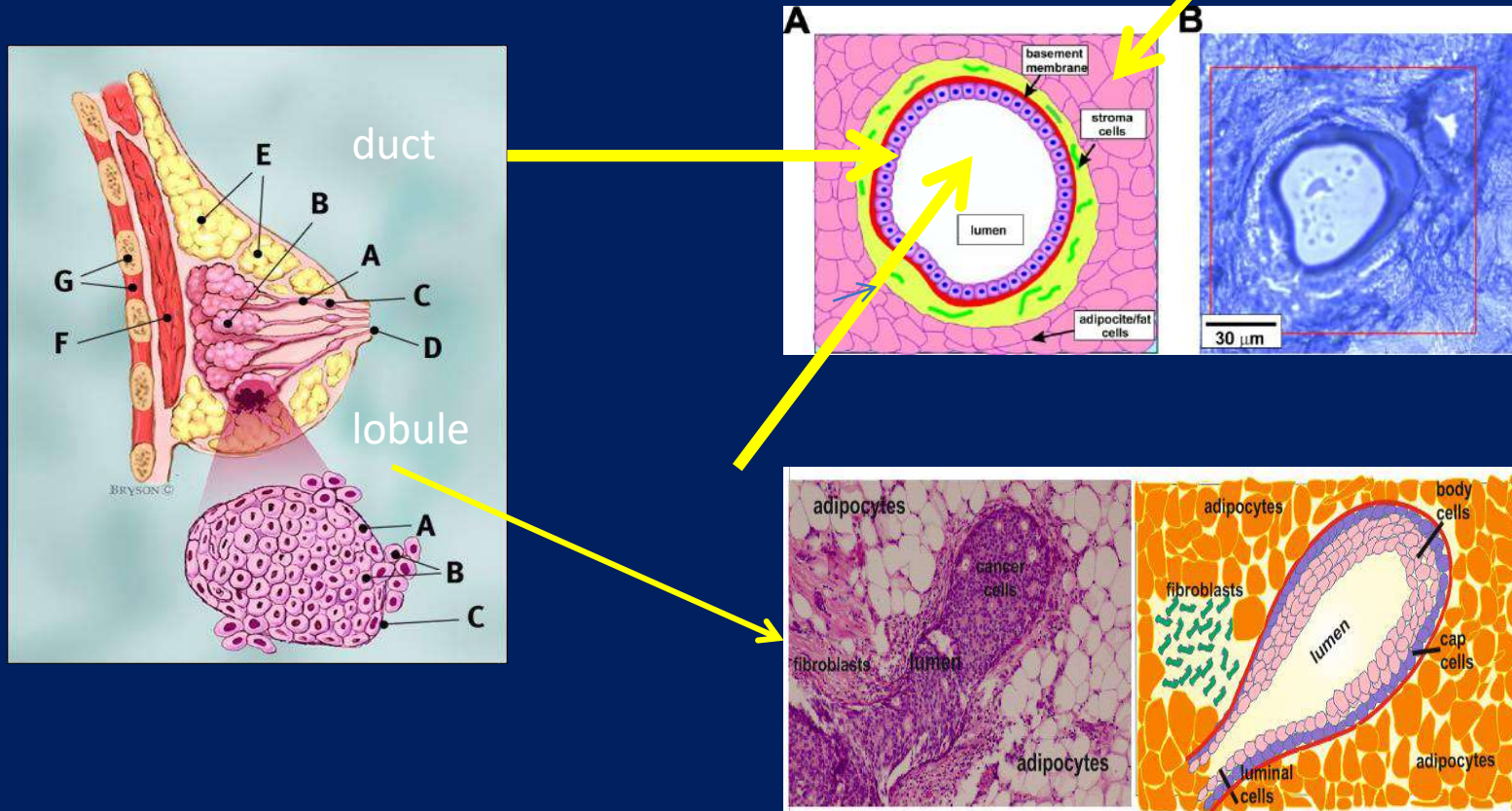
Halina Abramczyk  , Beata Brozek-Pluska

[+ Show more](#)



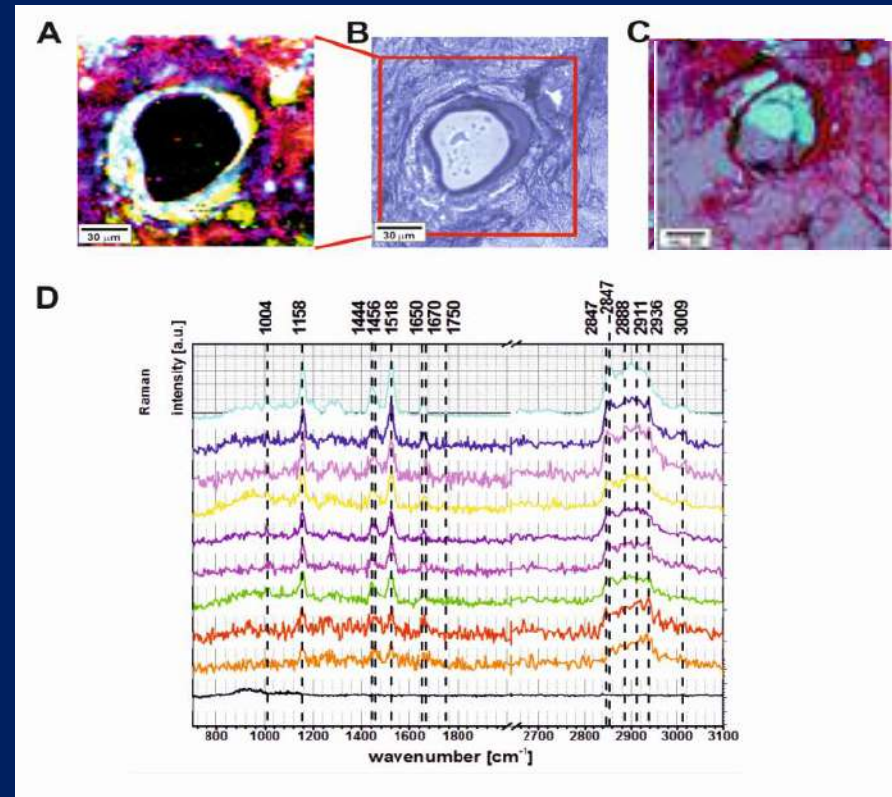
We will look inside human breast ducts answering fundamental questions about location and distribution of various biochemical components inside the lumen, epithelial cells of the duct and the stroma around the duct during cancer development.

Breast morphology and biochemistry by Raman imaging



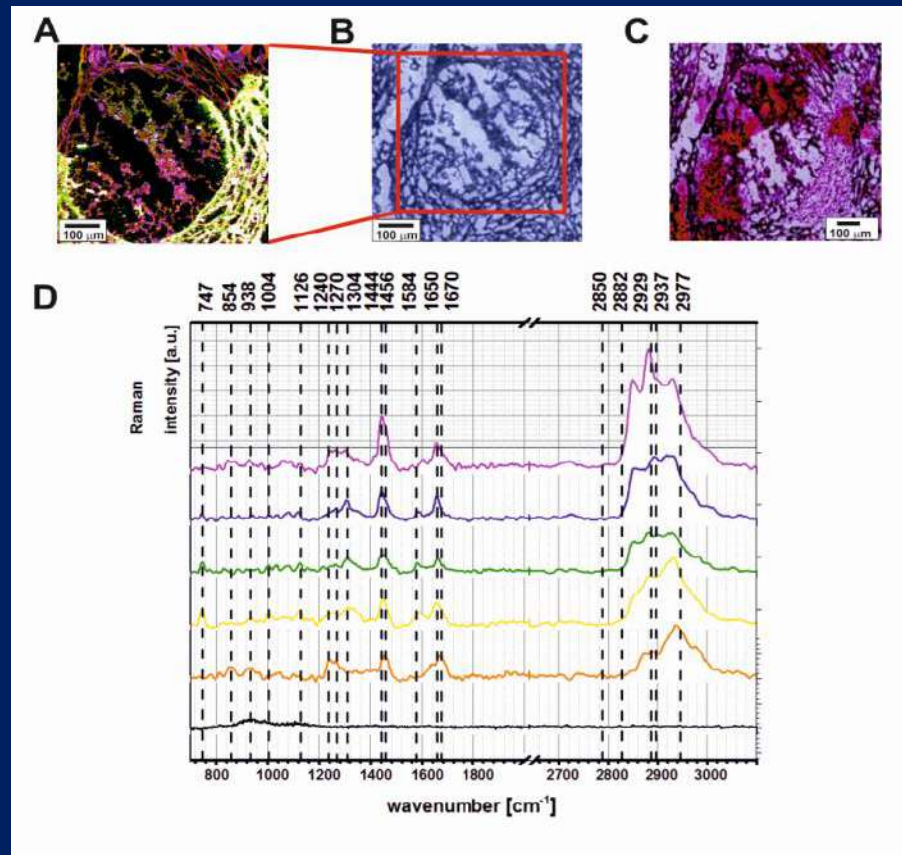
We will look inside human breast ducts answering fundamental questions about location and distribution of various biochemical components inside the lumen, epithelial cells of the duct and the stroma around the duct during cancer development.

Cross section through the normal organization of the duct



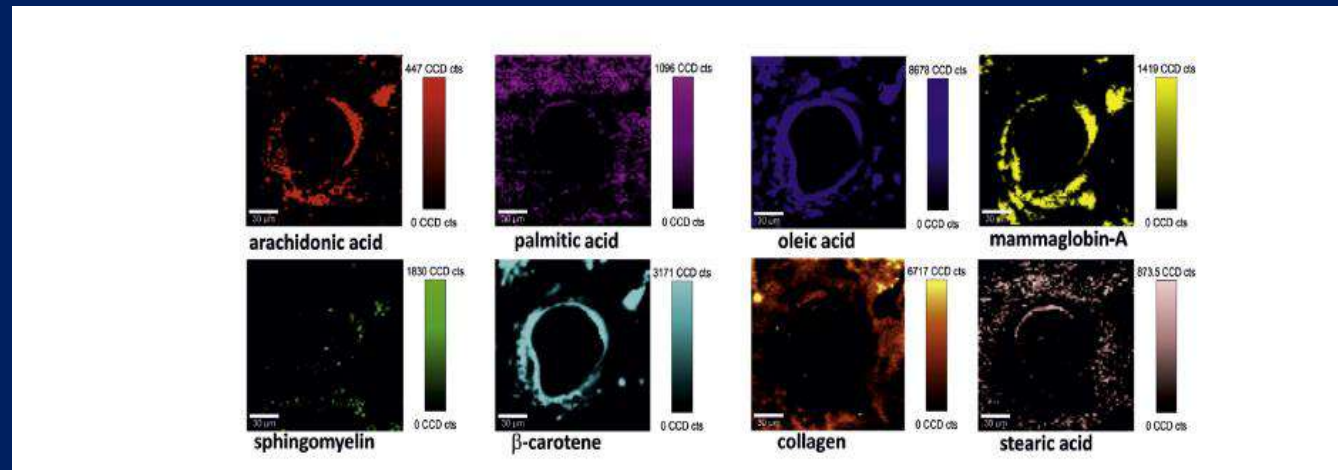
Looking inside the human body fascinated mankind for thousands of years. Current diagnostic and therapy methods are often limited by inadequate sensitivity, specificity and spatial resolution. Raman imaging may bring revolution in monitoring of disease and treatment. The main advantage of Raman imaging is that it gives spatial information about various chemical constituents in defined cellular organelles in contrast to conventional methods (LC/MS, NMR, HPLC) that rely on bulk or fractionated analyses of extracted components. We will demonstrate how Raman imaging can drive the progress on cancer just unimaginable a few years ago.

Cross section through the cancerous duct

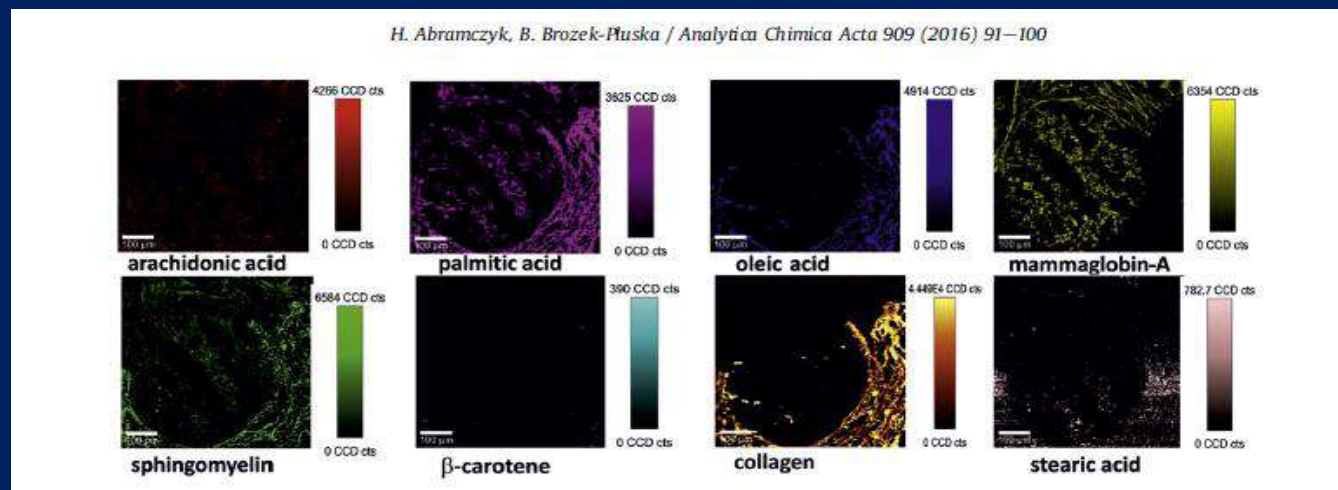


Looking inside the human body fascinated mankind for thousands of years. Current diagnostic and therapy methods are often limited by inadequate sensitivity, specificity and spatial resolution. Raman imaging may bring revolution in monitoring of disease and treatment. The main advantage of Raman imaging is that it gives spatial information about various chemical constituents in defined cellular organelles in contrast to conventional methods (LC/MS, NMR, HPLC) that rely on bulk or fractionated analyses of extracted components. We will demonstrate how Raman imaging can drive the progress on breast cancer just unimaginable a few years ago.

Comparison of Raman images: cross section through the normal and cancerous duct



normal duct



cancerous duct

Carotenoids, oleic acid: candidates as diagnostic markers for normal breast prognosis.

Mammaglobin, palmitic acid, and sphingomyelin: candidates as diagnostic markers for breast cancer prognosis.

Surmacki J, Brozek-Pluska B, Kordek R, Abramczyk H, The lipid-reactive oxygen species phenotype of breast cancer. Raman spectroscopy and mapping, PCA and PLSDA for invasive ductal carcinoma and invasive lobular carcinoma. Molecular tumorigenic mechanisms beyond Warburg effect, Analyst, 2015, 140, 2121 – 2133, (IF=4.2)

Analyst

2015

PAPER

View Article Online
View Journal

The lipid-reactive oxygen species phenotype of breast cancer. Raman spectroscopy and mapping, PCA and PLSDA for invasive ductal carcinoma and invasive lobular carcinoma. Molecular tumorigenic mechanisms beyond Warburg effect

Jakub Surmacki¹, Beata Brozek-Pluska², Radzislav Kordek³ and Halina Abramczyk^{1*}

Vibrational signatures of human breast tissue (invasive ductal carcinoma and invasive lobular carcinoma) were used to identify, characterize and discriminate structures in normal (noncancerous) and cancerous tissues by confocal Raman imaging, Raman spectroscopy and IR spectroscopy. The most important differences between normal and cancerous tissues were found in regions characteristic for vibrations of carotenoids, fatty acids, proteins, and interfacial water. Particular attention was paid to the role played by unsaturated fatty acids and their derivatives. K-means clustering and basis analysis followed by PCA and



Volume 140 | Number 7 | 7 April 2015 | Pages 2047–2524

Analyst

www.rsc.org/analyst

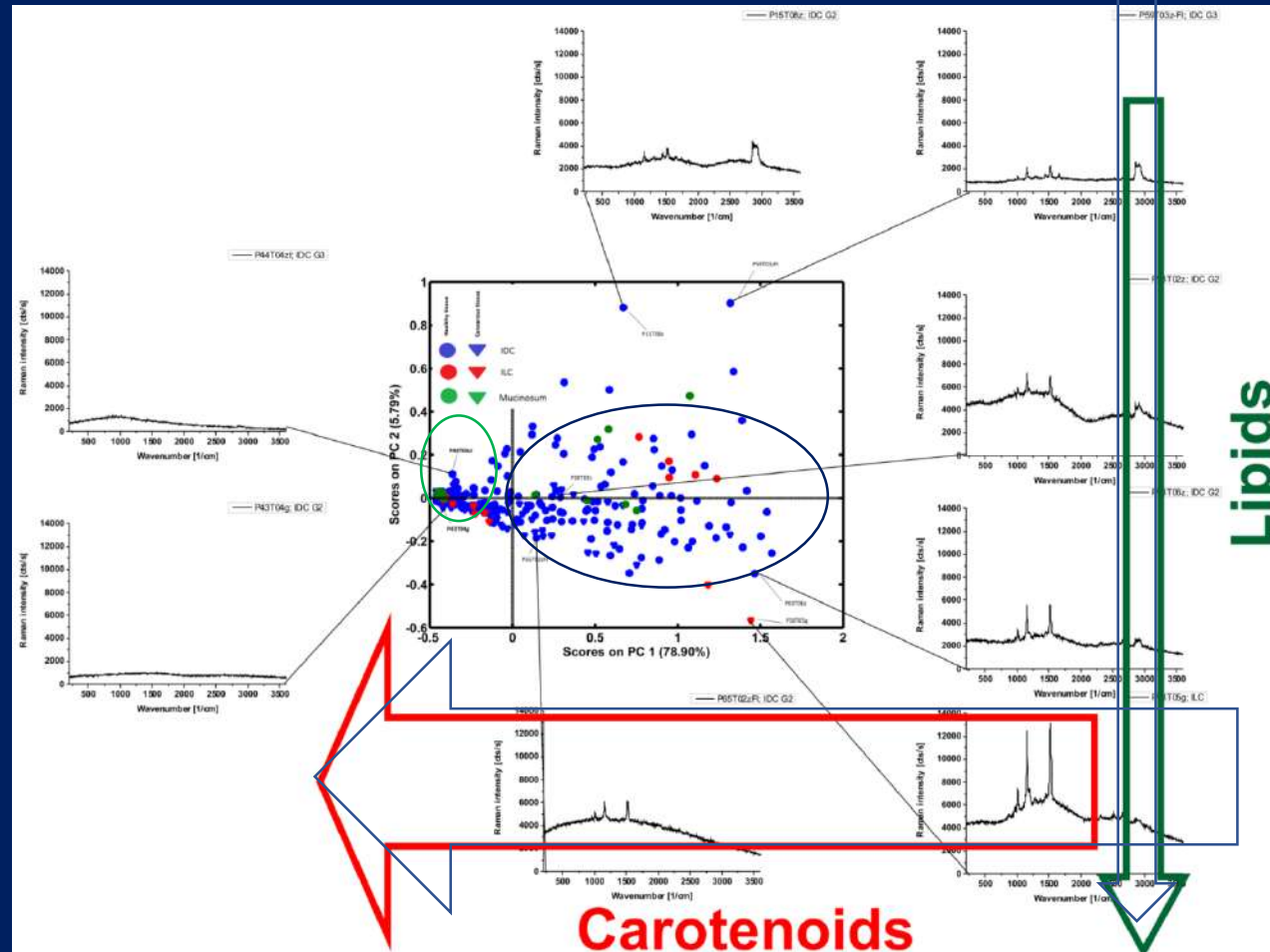
Cover 2015

ISSN 0003-2654

PAPER
Jakub Surmacki, Beata Brozek-Pluska, Radzislav Kordek and Halina Abramczyk
The lipid-reactive oxygen species phenotype of breast cancer: Raman spectroscopy and mapping, PCA and PLSDA for invasive ductal carcinoma and invasive lobular carcinoma. Molecular tumorigenic mechanisms beyond Warburg effect.

The Raman biomarkers we have identified show evidently that lipid phenotype plays a very important role in cancer development.

Breast cancer biodiagnostics. Raman biomarkers



In order to evaluate the diagnostic value of the Raman biomarkers for monitoring cancer pathology we have applied the principal component analysis. Here we can see a score PCA plot. Without going into the PCA details it is easy to see that the samples in this figure belong to one of two groups. Namely, the samples in the left and the right areas separated along PC1. In the left area there are almost exclusively the tumor tissues. In the right area there are almost exclusively the normal tissues.



Contents lists available at SciVerse ScienceDirect

Progress in Biophysics and Molecular Biology

journal homepage: www.elsevier.com/locate/pbiomolbio



Review

Raman 'optical biopsy' of human breast cancer

Halina Abramczyk^{a,*}, Beata Brozek-Pluska^a, Jakub Surmacki^a, Joanna Jablonska-Gajewicz^b,
Radziszław Kordek^b

^a Technical University of Lodz, Institute of Applied Radiation Chemistry, Laboratory of Laser Molecular Spectroscopy, Lodz, Poland

^b Medical University of Lodz, Department of Pathology, Chair of Oncology, Lodz, Poland

2012

ARTICLE INFO

Article history:

Available online 19 November 2011

Keywords:

Raman spectroscopy
Raman mapping
Medical diagnostics
Breast cancer

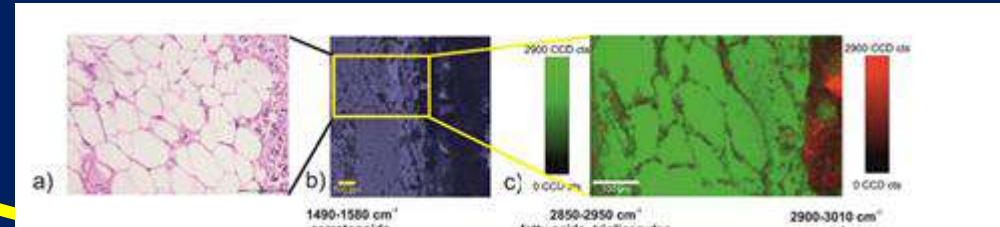
ABSTRACT

Raman imaging (RI) is a novel method of medical diagnostics of human breast cancer and has a potential to become a routine optical biopsy. Up to date the present study is the most statistically reliable Raman analysis based on data of normal, benign, and cancerous breast tissues for 146 patients. This paper present the first Raman 'optical biopsy' images of the normal and cancerous breast tissue of the same patient. The results presented here demonstrate the ability of Raman spectroscopy to accurately characterize cancer tissue and distinguish between normal (noncancerous), and cancerous types. The results provide evidence that carotenoids and lipids composition of cancerous breast tissues differs significantly from that of the surrounding noncancerous breast tissue and may be a key factor responsible for mechanisms of carcinogenesis. We have found that fatty acid composition of the cancerous breast tissue is markedly different from that of the surrounding noncancerous breast tissue. The cancerous breast tissue seems to be dominated by the metabolism products of the arachidonic acid - derived cyclic eicosanoids catalyzed by cyclooxygenase, while the noncancerous breast tissue is dominated by monounsaturated oleic acid and its derivatives.

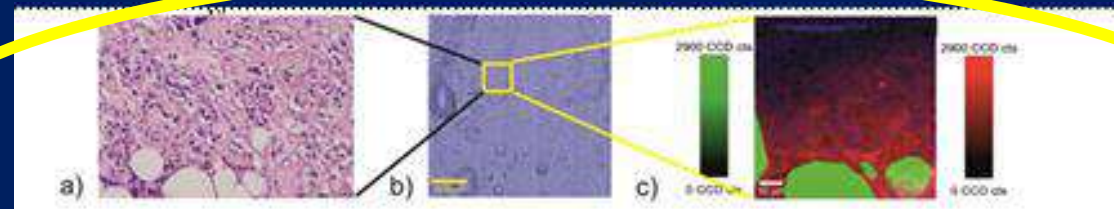
© 2011 Elsevier Ltd. All rights reserved.

Raman optical biopsy of human breast cancer tissue

safety margin

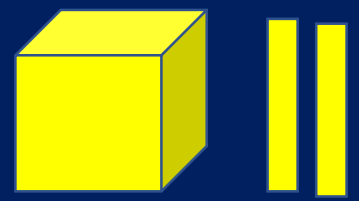
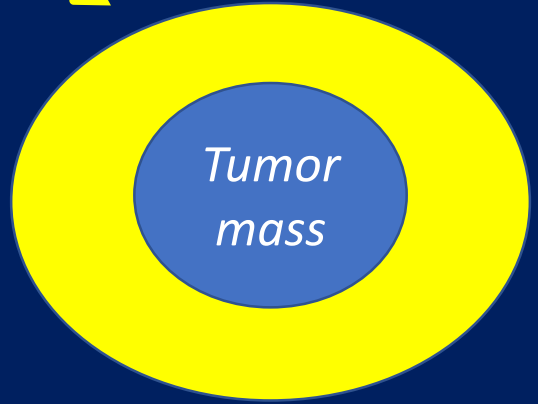


tumor mass

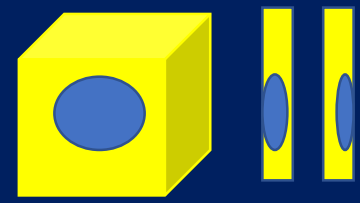
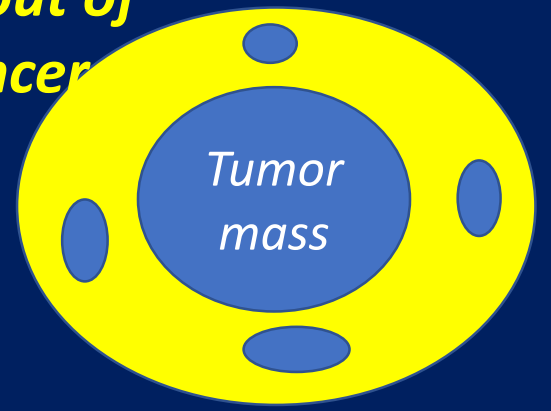


The completeness of the surgical resection is a key factor in the progress of patients with breast tumors. The safety margin can be positive which means that not all cancer cells have been removed in the surgery. Patients with a positive margin often require more surgery to make sure that all the cancer is removed. The advantage of the 'Raman biopsy' is that it provides direct biochemical information (vibrational fingerprint) in real time, it is not prone to subjective interpretations, and it monitors biological tissue without any external agents, in contrast to histopathological assessment.

Negative safety margin
No cancer cells are found by histology

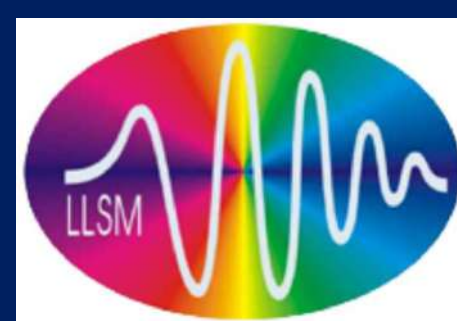


Positive safety margin
cancer cells extend out of the tumor mass, cancer cells are found by histology



adjacent sections of 5 μm

We have already begun to translate Raman spectroscopy into a novel clinical diagnostic tool using various endoscopic strategies for in vivo applications during operations of brain.



The biochemical, nanomechanical and chemometric signatures of brain cancer

Spectrochimica Acta Part A: Molecular and Biomolecular Spectroscopy 188 (2018) 8–19

2018



Contents lists available at ScienceDirect

Spectrochimica Acta Part A: Molecular and Biomolecular Spectroscopy

journal homepage: www.elsevier.com/locate/saa



The biochemical, nanomechanical and chemometric signatures of brain cancer

Halina Abramczyk*, Anna Imiela

Lodz University of Technology, Faculty of Chemistry, Institute of Applied Radiation Chemistry, Laboratory of Laser Molecular Spectroscopy, Wroblewskiego 15, 93-590 Lodz, Poland



HOW DOES RAMAN SPECTROSCOPY AND IMAGING BENEFIT CANCER RESEARCH?

- **the emergence of Raman-driven proteomics, lipidomics, glycomics, and epigenetics research**

- These enhanced studies are needed to improve the elusive outcomes in the war on cancer

ELUSIVE OUTCOMES IN THE WAR ON CANCER

In a recent study, TCGA reported that over 30,000 mutations were identified in breast cancer tissue (Cancer Genome Atlas Network, 2012). The evidence seems to suggest that science based only on cancer genomics, cannot be continued.

TRENDS IN CANCER RESEARCH

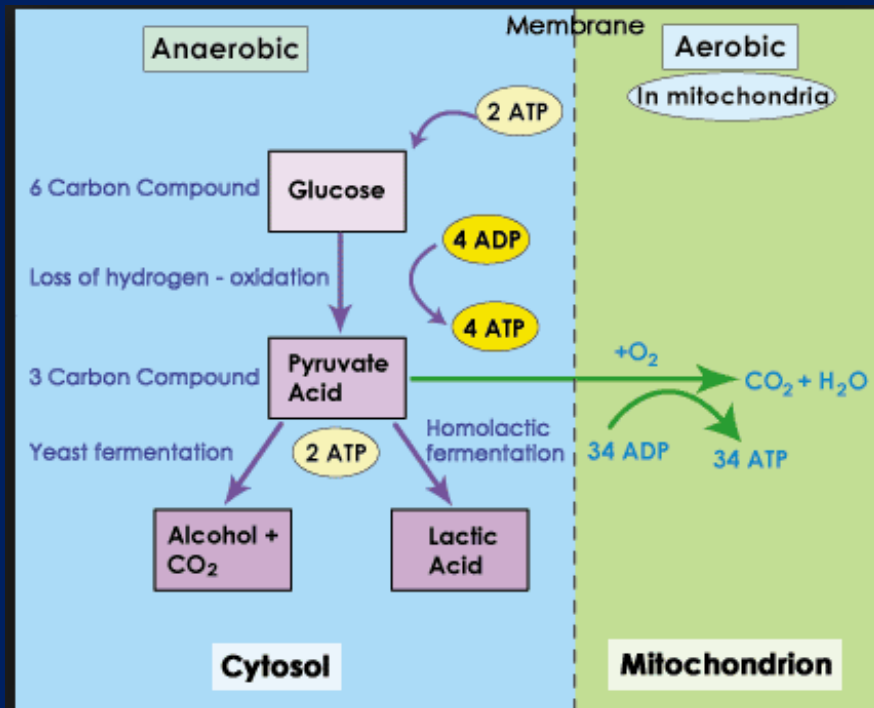
- Presently, a growing number of reports have initiated a discussion about the benefits of metabolic regulation in cancers. The Warburg effect, a great discovery approximately 90 years ago, addresses the “universality” of cancer characteristics. For instance, most cancer cells prefer anerobic glycolysis instead of mitochondrial respiration.

Biomol Ther (Seoul) 2015; 23(2): 99-109 <https://doi.org/10.4062/biomolther.2015.013>

Cancer Metabolism: Strategic Diversion from Targeting Cancer Drivers to Targeting Cancer Suppliers

Warburg effect

The best characterized metabolic phenotype observed in tumour cells is the Warburg effect, which is a shift from ATP generation through oxidative phosphorylation to ATP generation through conversion to lactate glycolysis, even under normal oxygen concentrations.

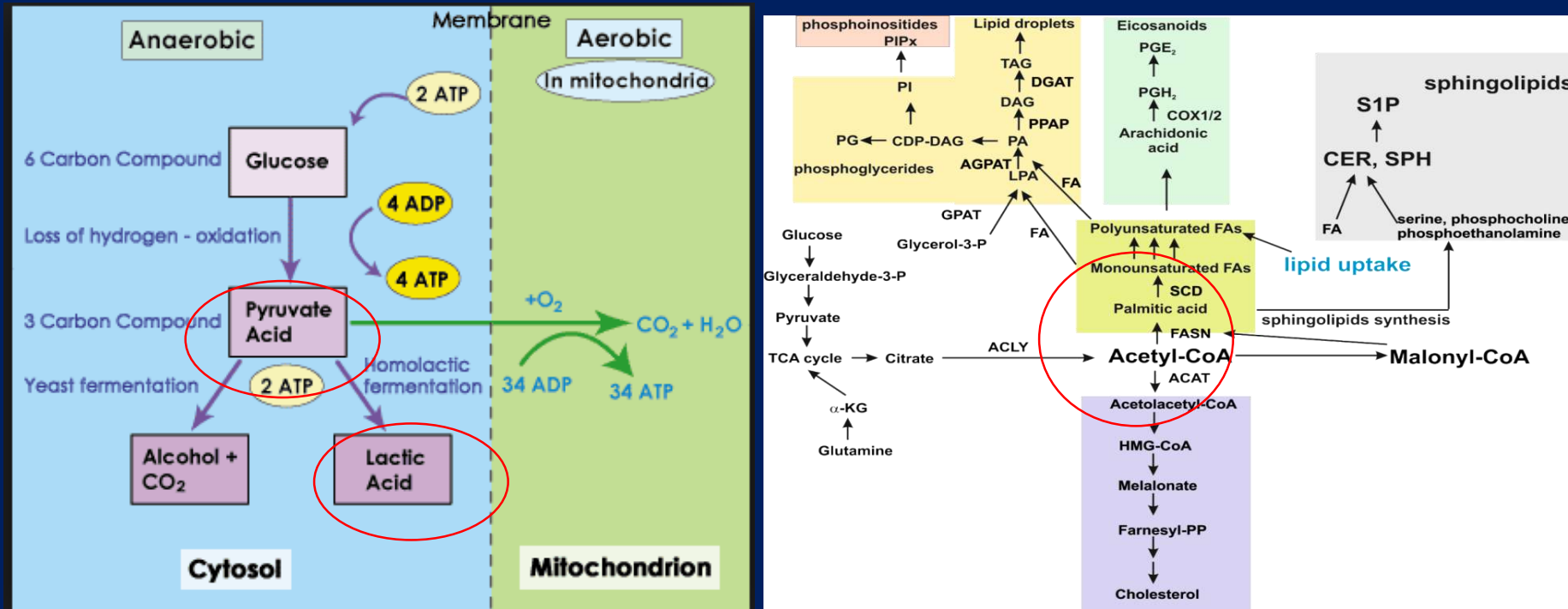


CANCER PHENOTYPE

Lipid metabolic reprogramming in cancer cells

However, metabolic adaptation in tumours extends beyond the Warburg effect. It is becoming clear that alterations to metabolism balance the need of the cell for energy with its equally important need for macromolecular building blocks and maintenance of redox balance.

enhanced anaerobic glycolysis vs *de novo* fatty-acid synthesis



- The altered metabolism is one of the important features of cancer and is usually described by Otto Warburg effect with enhanced anaerobic glycolysis.²⁷ The elevated glucose catabolism produces an excess of the glycolytic end-product, pyruvate. Most of the pyruvate is converted to lactate, whereas some of it is converted to acetyl-CoA, which, in turn, is used in *de novo* fatty-acid synthesis .

The lipid phenotype was ignored for many years by the Raman scientific community that has focused almost exclusively on the biosynthesis of proteins and the proteome profile.

Several groups have explored the potential of Raman and IR spectroscopy for breast cancer detection

13 C. J. Frank, R. L. McCreery and D. C. Redd, *Anal. Chem.*, 1995, 67, 777–783.

14 A. Mahadevan-Jansen and R. R. Richards-Kortum, *J. Biomed. Opt.*, 1996, 1, 31–70.

15 N. J. Kline and P. J. Treado, *J. Raman Spectrosc.*, 1997, 28, 119–124.

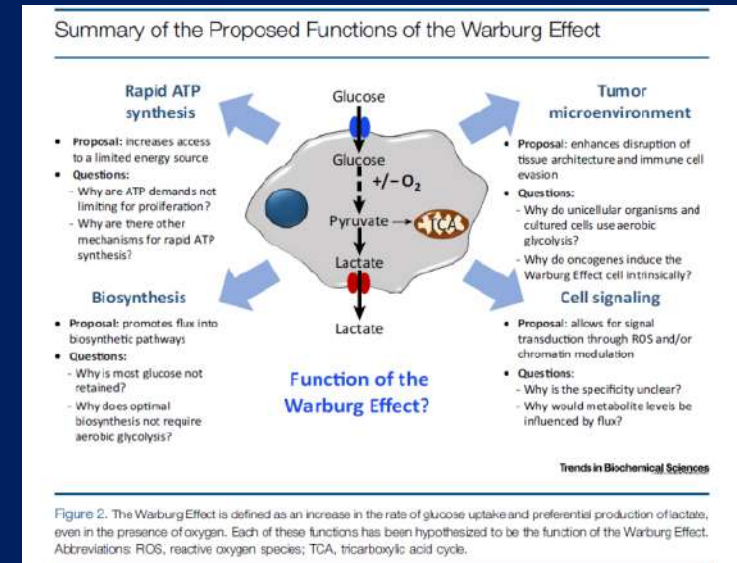
16 N. Stone, R. Baker, K. Rogers, A. W. Parker and P. Matousek, *Analyst*, 2007, 132, 899–905.

17 A. S. Haka, Z. Volynskaya, J. A. Gardecki, J. Nazemi, R. Shenk, N. Wang, R. R. Dasari, M. Fitzmaurice and M. S. Feld, *J. Biomed. Opt.*, 2009, 14, DOI: 10.1117/1.3247154.

18 M. Diem, M. Miljković, B. Bird, T. Chernenko, J. Schubert and E. Marcsisin, *Spectrosc. Int. J.*, 2012, 27, 463–496.

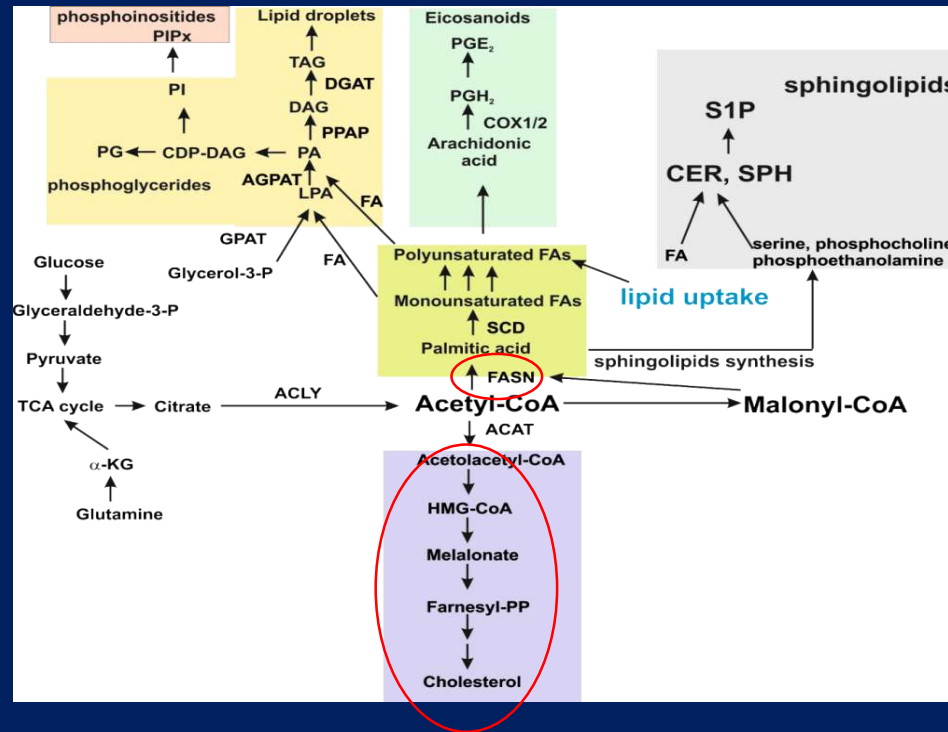
19 A. Mahadevan-Jansen, M. F. Mitchell, N. Ramanujam, A. Malpica, S. Thomsen, U. Utzinger and R. Richards-Kortum, *Photochem. Photobiol.*, 1998, 68, 123–132.

Our result analyzed in the context of a number of literature studies, suggests that fatty acids and the products of their metabolism play an important role in the molecular mechanisms of carcinogenesis



The almost exclusive proteome interpretation of biological tissue in the literature is partially related to the fact that most research uses histological sections or commercially available paraffin embedded tissues instead of using fresh tissue as presented in this paper.

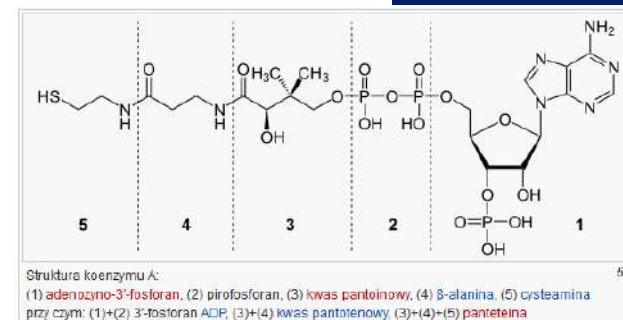
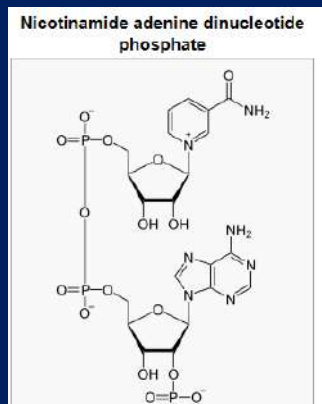
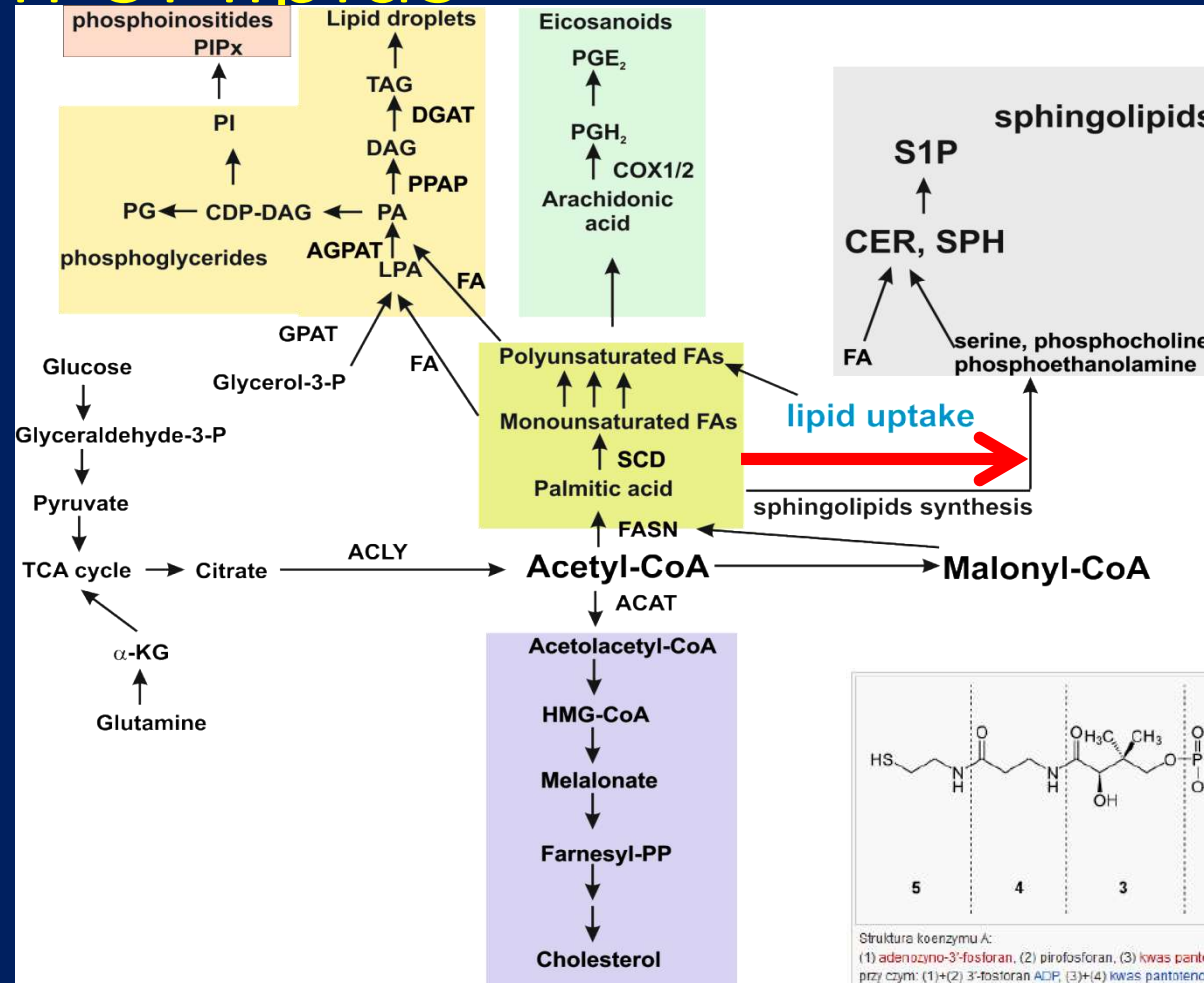
LIPID REPROGRAMMING IN TUMORS



Increased expression of lipogenic enzymes, fatty acid synthase (FASN), and ATP citrate lyase (ACLY) that promote also cholesterol synthesis, represent a nearly-universal phenotypic alteration in most tumors. **FASN overexpression predicts poor prognosis in cancer patients**

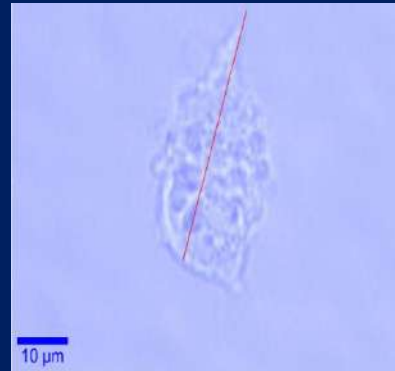
Increased expression of lipogenic enzymes, such as acetyl-CoA carboxylase (ACC) and fatty acid synthase (FASN), and ATP citrate lyase (ACLY) that promote also cholesterol synthesis, represent a nearly-universal phenotypic alteration in most tumors.^{32,33} **FASN overexpression predicts poor prognosis in cancer patients.**³⁴ Its expression levels appear at the precancerous lesion stage and persist in metastatic breast and prostate tumors.³⁴ Colorectal cancer (CRC) lipid signature, defined from a limited lipid-related genes expression profiling, reveals four genes (ABCA1, ACSL1, AGPAT1 and **stearoyl-CoA desaturase (SCD)**) overexpressed only in stage II CRC patients with a high risk of relapse.

Metabolism of lipids



Our results indicate that the lipid synthesis de novo in cancer transformed epithelial cells occurs via sphingolipid synthesis.

To address these important questions on lipid phenotypic alterations we studied lipid compositional mapping of cellular compartments, such as lipid droplets (LDs) in cell cultures



- Recent advances in lipid analytical and imaging technologies, including Raman scattering microscopy, have greatly progressed such lipidomic analysis. Raman-based imaging offers lipid compositional mapping of cellular compartments, such as LDs. These complementary approaches provide crucial information on tumor lipid phenotype, in particular abundance, FA composition and spatial distribution of lipid classes within tumors

Raman imaging of a single cells.

The role of lipid droplets and adipocytes in cancer.

2015

Analyst

1

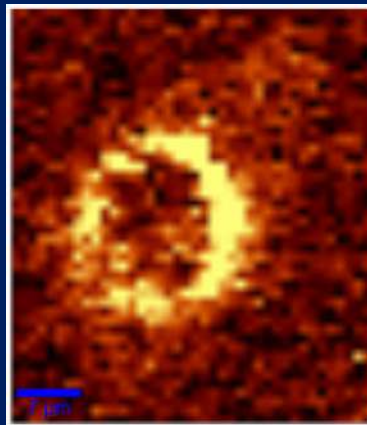
The role of lipid droplets and adipocytes in cancer. Raman imaging of cell cultures: MCF10A, MCF7, and MDA-MB-231 compared to adipocytes in cancerous human breast tissue|

Halina Abramczyk,* Jakub Surmacki, Monika Kopeć, Alicja Klaudia Olejnik, Katarzyna Lubecka-Pietruszewska and Krystyna Fabianowska-Majewska



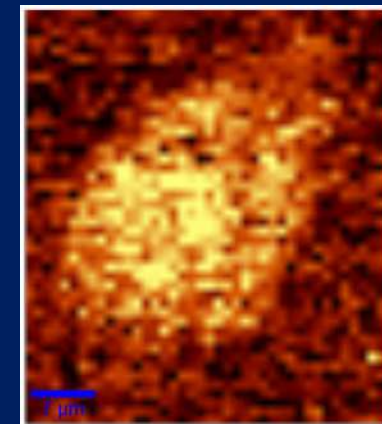
MCF7

Fatty acids



2830 -2950 cm^{-1}

Proteins



2900 -3010 cm^{-1}

Lipid droplets were mostly ignored and regarded mainly as static energy storage deposits. However, recent research has gained exciting new perspectives for lipid droplets showing that they represent important organelles containing specialized proteins and lipids which play essential roles in cell signaling, regulation of lipid metabolism, membrane trafficking and control of the synthesis and secretion of inflammatory mediators.

Microscopy, Raman, staining, fluorescence, AFM, SNOM images of MCF10A, MCF7 and MDA-MB-231 cells

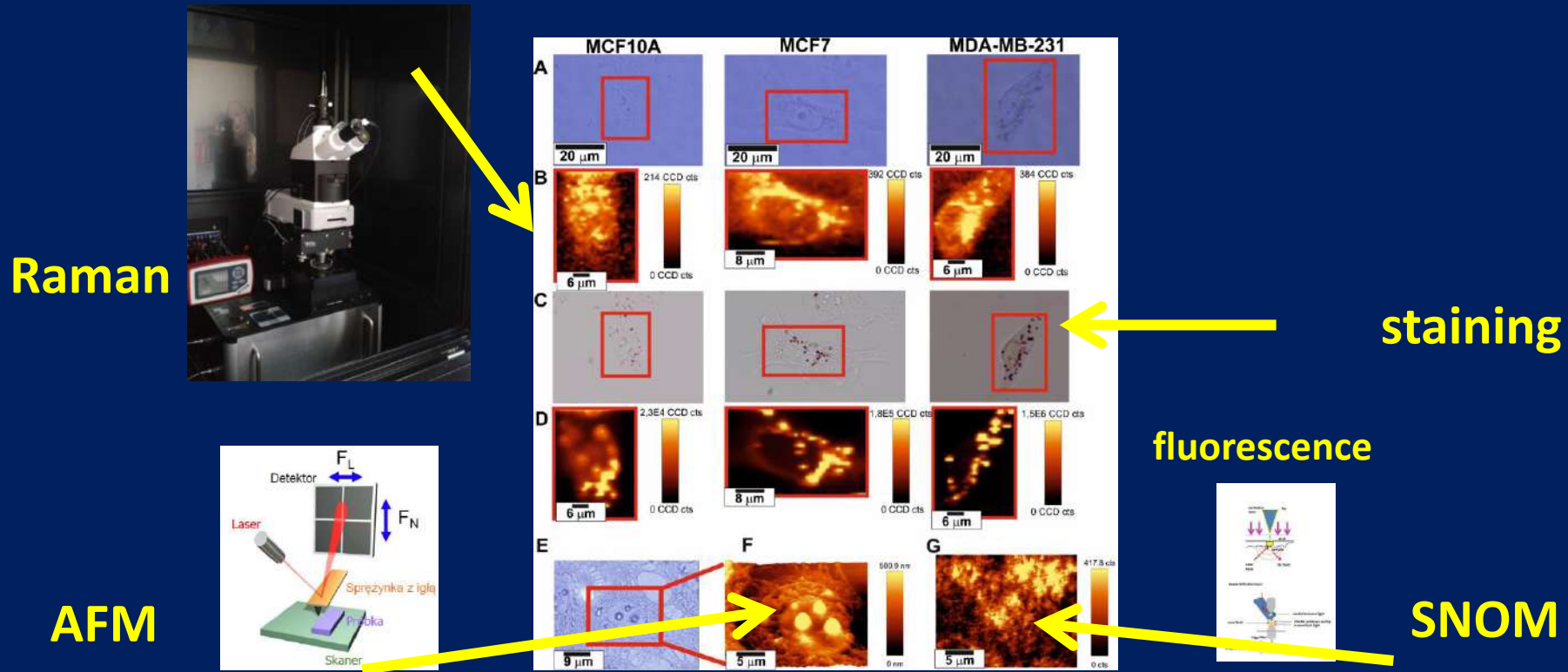
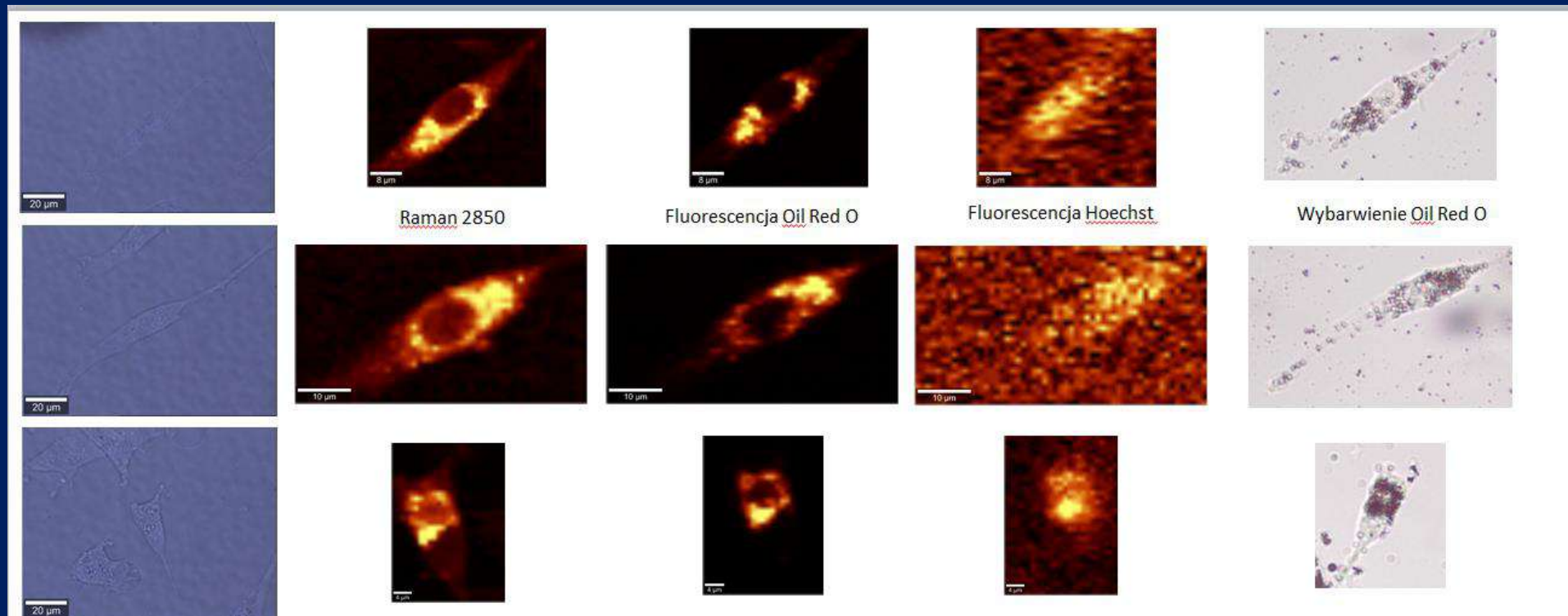
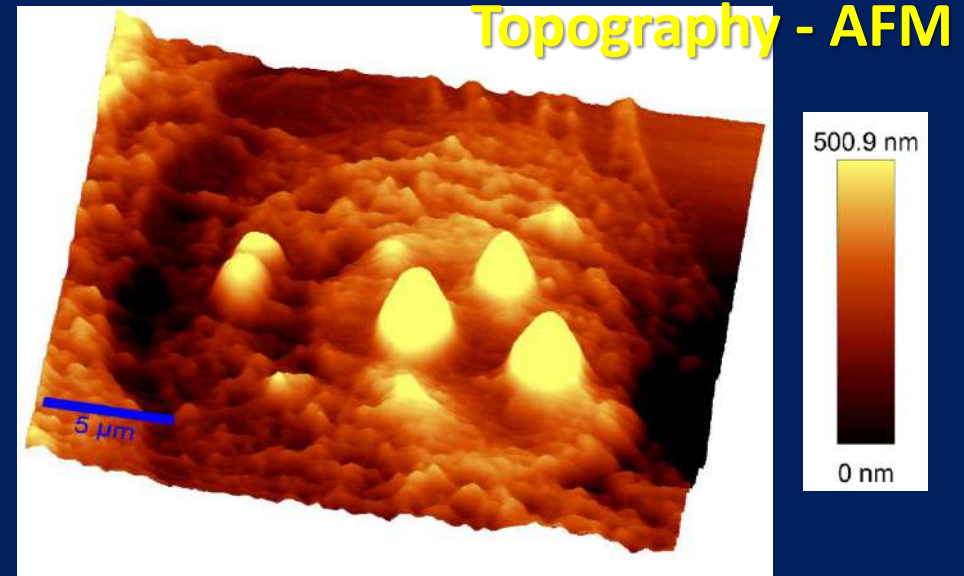
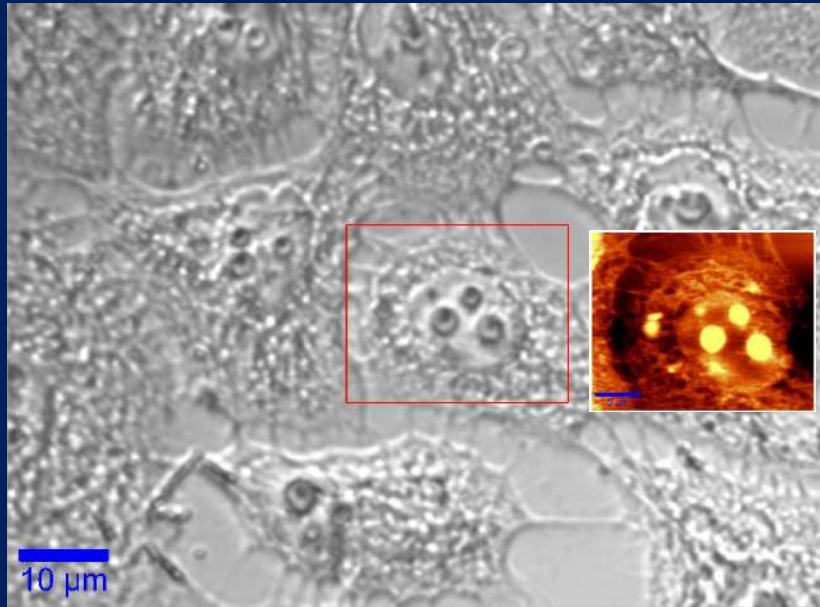


Fig 3. (A) Microscope images without staining of MCF10A, MCF7 and MDA-MB-231 cell lines. (B) Raman images of lipids distribution in the cells base on the Raman peak position at 2852 cm^{-1} (integration time: 0.5 sec, resolution step: 1 mm, excitation line power: 38mW). (C) Microscope images after staining with Oil Red O (D) Fluorescence images of Oil Red O distribution in the cells (integration time: 0.1 sec, resolution step: 1 mm, excitation line power: 10 mW), (E) Microscope images of the MCF10A cell without staining, (F) AFM image of the MCF10A cell, (G) SNOM image of the MCF10A cell,

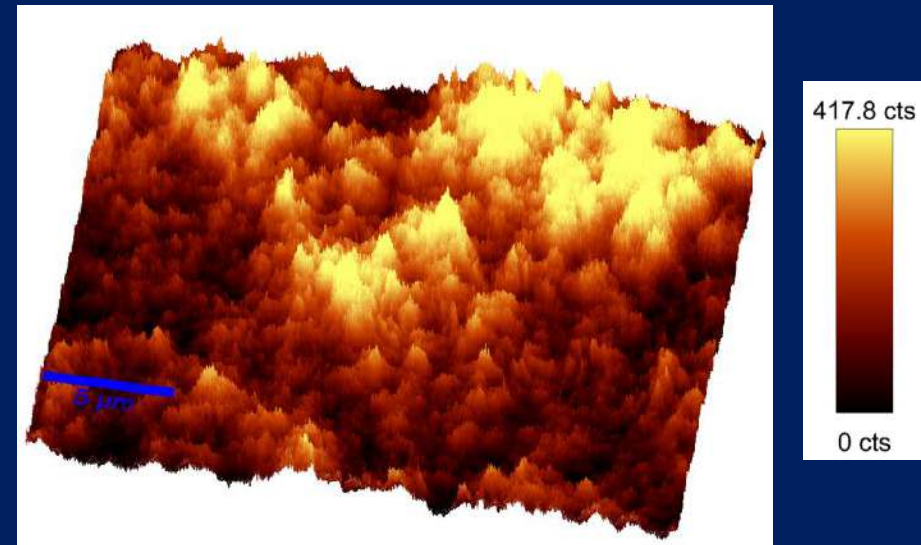
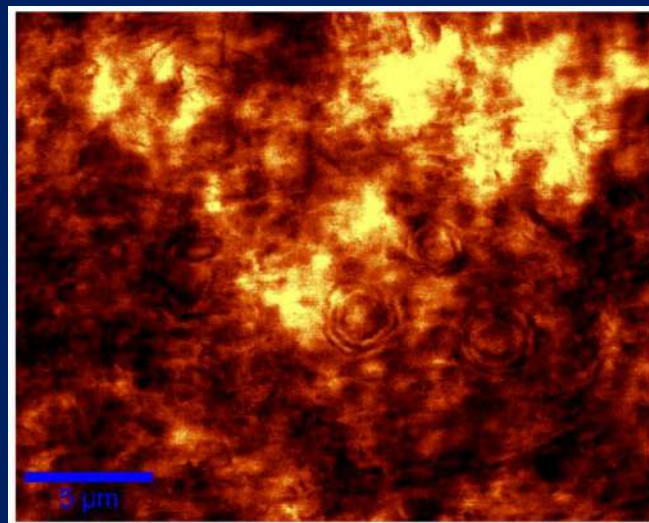
Microscopy, Raman, staining, fluorescence of glioblastoma U87MG cells



MCF10A cell – SNOM (*scanning near field optical microscopy*)



SNOM (*PMT_F*)



The role of lipid droplets and adipocytes in cancer. Raman imaging of cell cultures: MCF10A, MCF7, and MDA-MB-231 compared to adipocytes in cancerous human breast tissue

Analyst

2015

1

The role of lipid droplets and adipocytes in cancer.
Raman imaging of cell cultures: MCF10A, MCF7,
and MDA-MB-231 compared to adipocytes in
cancerous human breast tissue

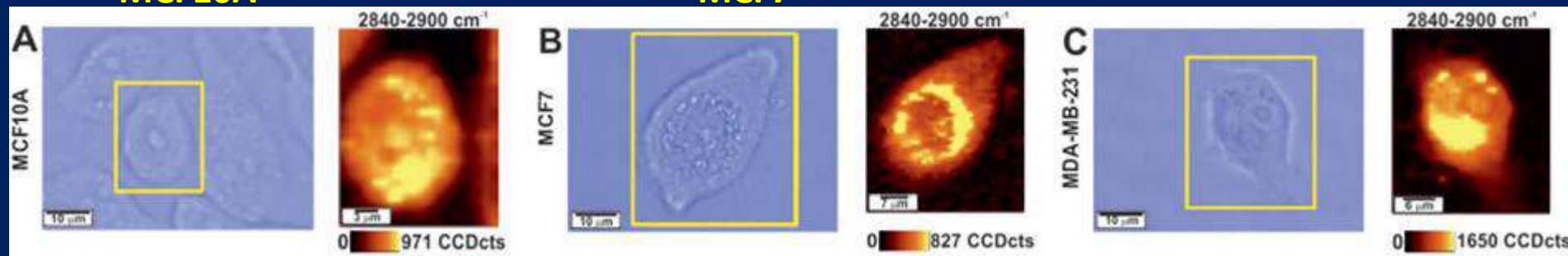
Halina Abramczyk,* Jakub Surmacki, Monika Kopeć,
Alicja Klaudia Olejnik, Katarzyna Lubecka-Pietruszewska
and Krystyna Fabianowska-Majewska

The goal of our study was to assess the impact of cancer aggressiveness on the amount of cytosolic lipid droplets in non-malignant and malignant human breast epithelial cell lines. We have studied live non-malignant (MCF10A), mildly malignant (MCF7) and malignant (MDA-MB-231) breast cancer cells.

MCF10A

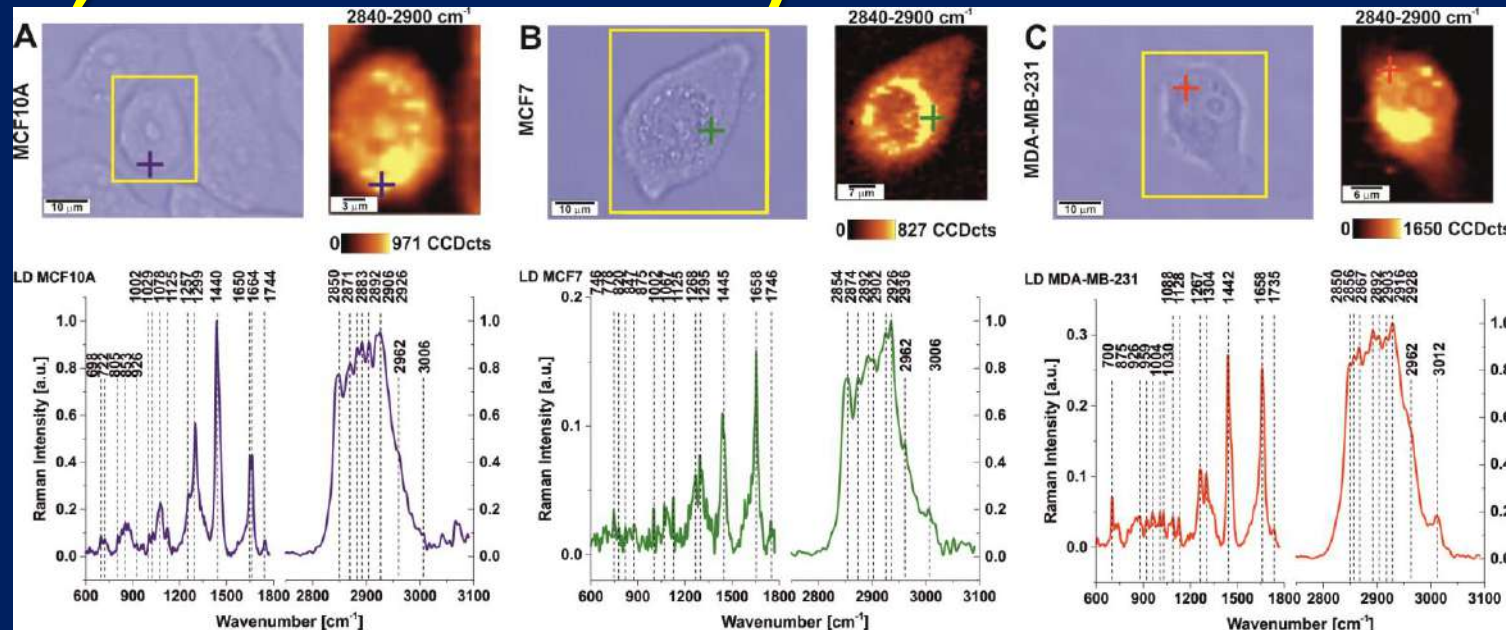
MCF7

MDA-MB-231



the Raman and video images of the intracellular structures are of virtually identical shapes, revealing well-defined subcellular morphological structures. However, Raman microscopy can reveal not only morphological structures but also valuable information on the detailed biochemical composition. The Raman images in the region of characteristic vibrations reveal well-defined protein structures, lipid droplets, and membranes without the need for staining.

Normal (MCF-10A) and cancerous breast cells (MCF-7, MDA-MB-231)



MCF-10A

MCF-7

MDA-MB-231

We have analyzed the composition of lipid droplets in nonmalignant and malignant human breast epithelial cell lines and discussed the potential of lipid droplets as a prognostic marker in breast cancer.

Lipid droplets are typically localized in strings adjacent to the lysosome (Fig. 1B) or randomly distributed in the cytosol (Fig. 1C). They are also frequently observed inside the lysosome.

H. Abramczyk, J. Surmacki, M. Kopeć, A. K. Olejnik, K. Lubecka-Pietruszewska, K. Fabianowska-Majewska, *The role of lipid droplets and adipocytes in cancer. Raman imaging of cell cultures: MCF10A, MCF7, MDA-MB-231 compared to adipocytes in cancerous human breast tissue*, Analyst, 2015, 140, 2224-2235
 ATCC protocols

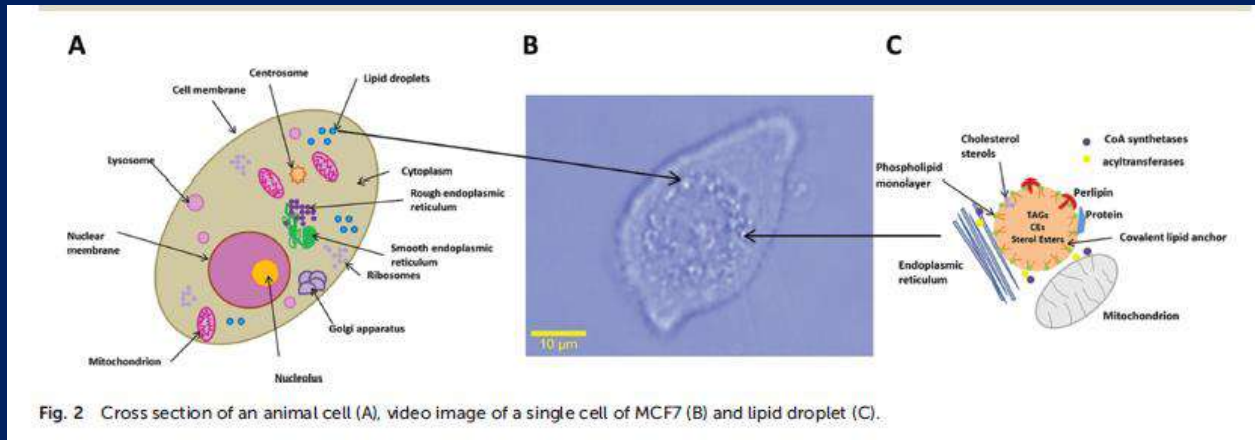
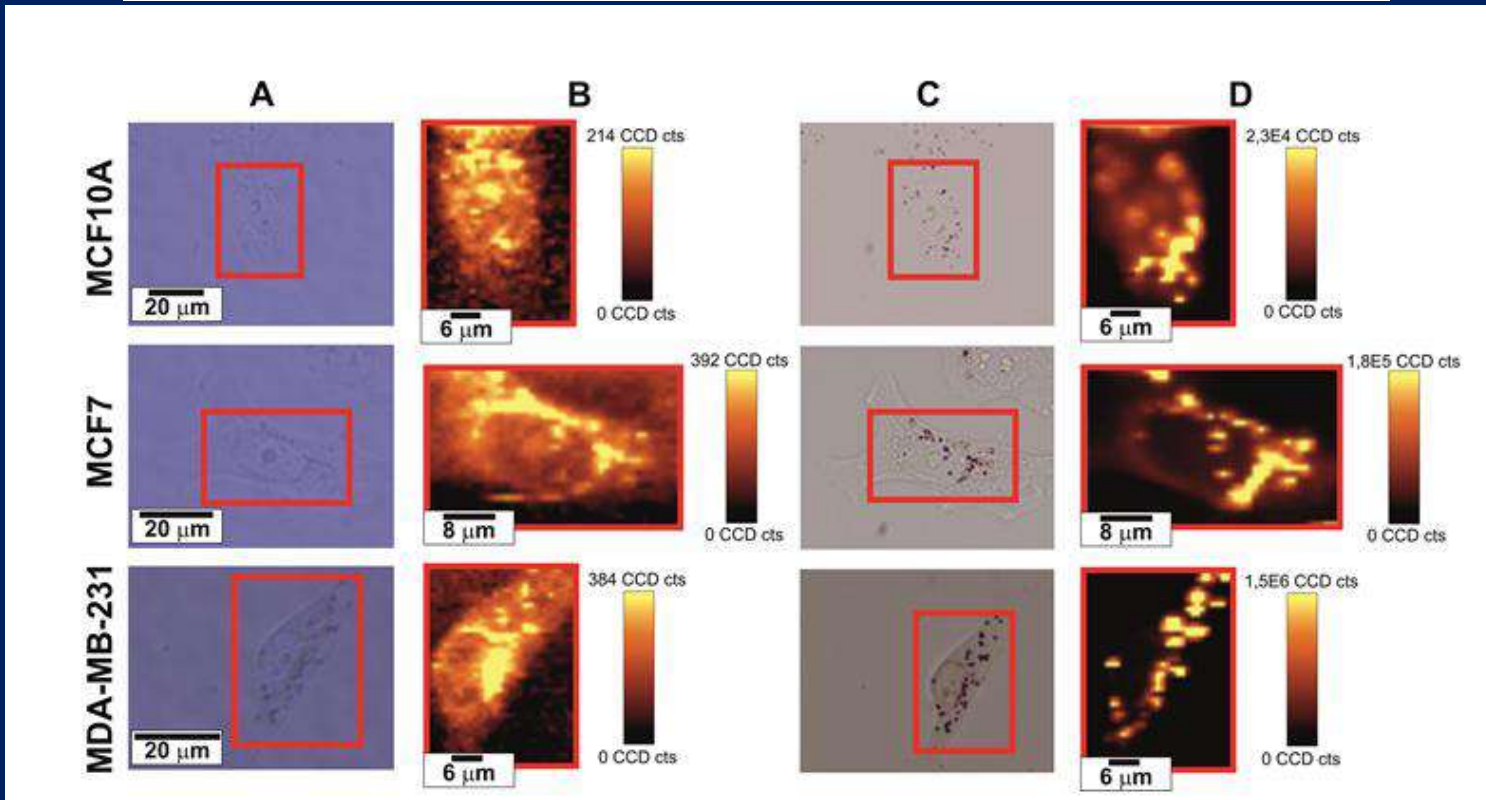
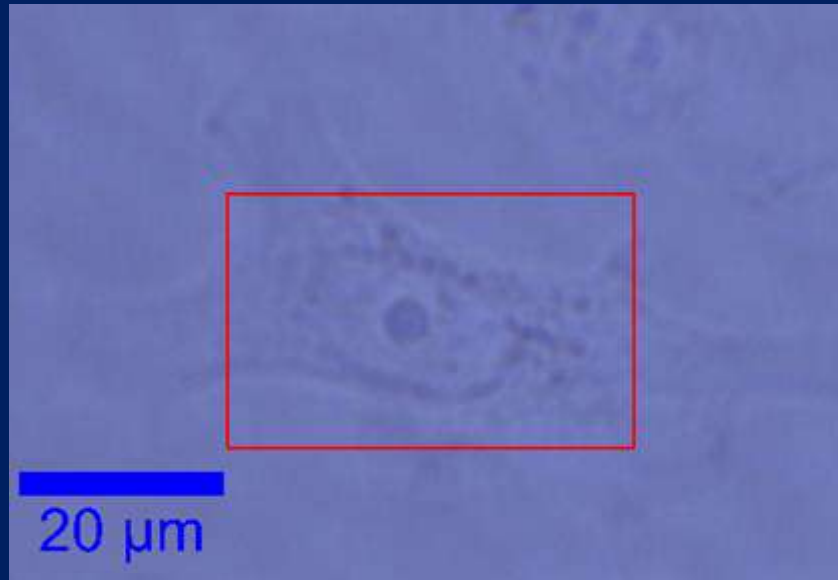


Fig. 2 Cross section of an animal cell (A), video image of a single cell of MCF7 (B) and lipid droplet (C).

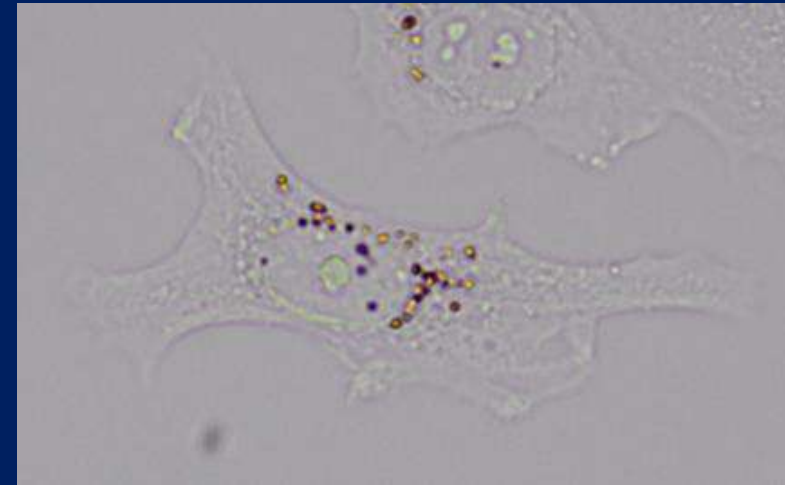


Here we present the microscopy image, Raman image, microscope image after staining with red oil and fluorescence image of the staining dye. One can see full correlation in the distribution of lipid droplets

MCF 7 before and after staining Red Oil O



BEFORE



AFTER



**Lipid droplets
(2820-2870 1/cm)**

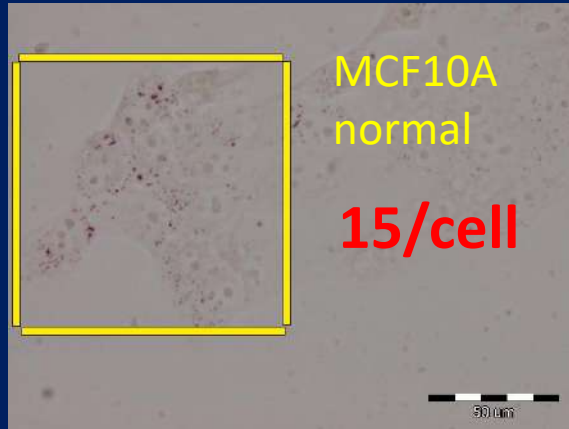


Fluorescence of Red Oil O

H. Abramczyk, J. Surmacki, M. Kopeć, A. K. Olejnik, K. Lubecka-Pietruszewska, K. Fabianowska-Majewska, *The role of lipid droplets and adipocytes in cancer. Raman imaging of cell cultures: MCF10A, MCF7, MDA-MB-231 compared to adipocytes in cancerous human breast tissue*, Analyst, 2015, 140, 2224-2235

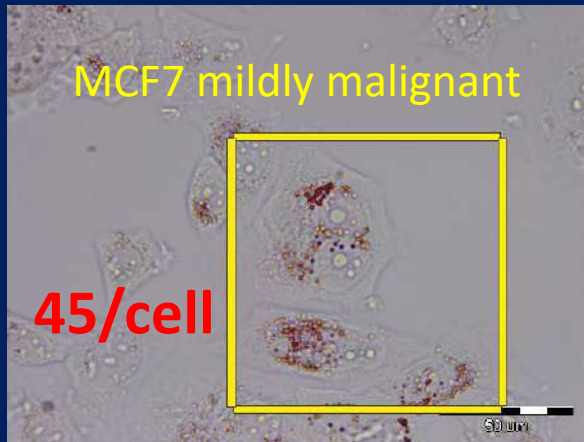
MCF10A

Number of lipid droplets 200
number of cells 13 15/cell



MCF7

Number of lipid droplets 135
number of cells 3 45/cell



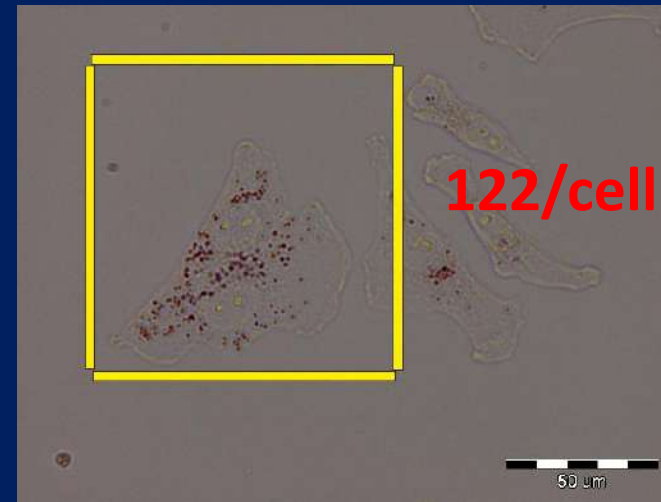
To quantify the number of the lipid droplets in the three cell lines, we have counted the droplets from the classical staining with Oil-Red-O and Raman images from the fixed regions of 120 μm × 120 μm.

MDA-MB-231

Number of lipid droplets 122 number of cells
1, 122/cell

MDA-MB-231

Agressively malignant



Cancer cells contain increased numbers of lipid droplets compared with normal cells.

An increased amount of lipid droplets correlates with increased aggressiveness of cancer.

The increased amount of cytoplasmic lipid droplets in the human breast cell may be closely related to increased rate of lipid synthesis in cancerous tissues.

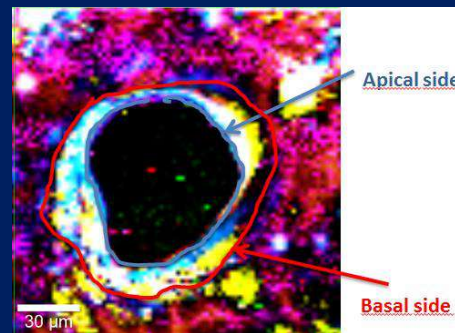
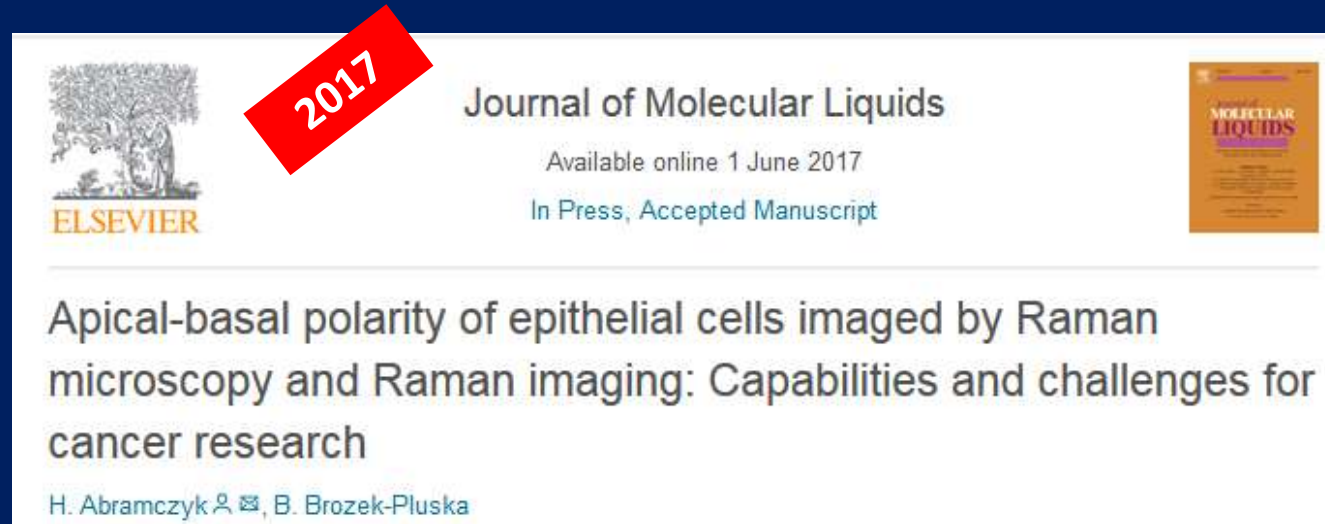
EMERGENCE OF CANCER METABOLISM

Important changes in lipid composition (saturated (SFA) vs unsaturated FA) and abundance severely alter membrane fluidity and protein dynamics. For example, an increase in saturated phospholipids (PLs) markedly alters signal transduction, protects cancer cells from oxidative damage such as lipid peroxidation and potentially inhibits the uptake of chemotherapeutic drugs.

HOW DOES RAMAN SPECTROSCOPY AND IMAGING BENEFIT CANCER RESEARCH?

- **POLARITY OF CELLS**

POLARITY OF EPITHELIAL CELLS



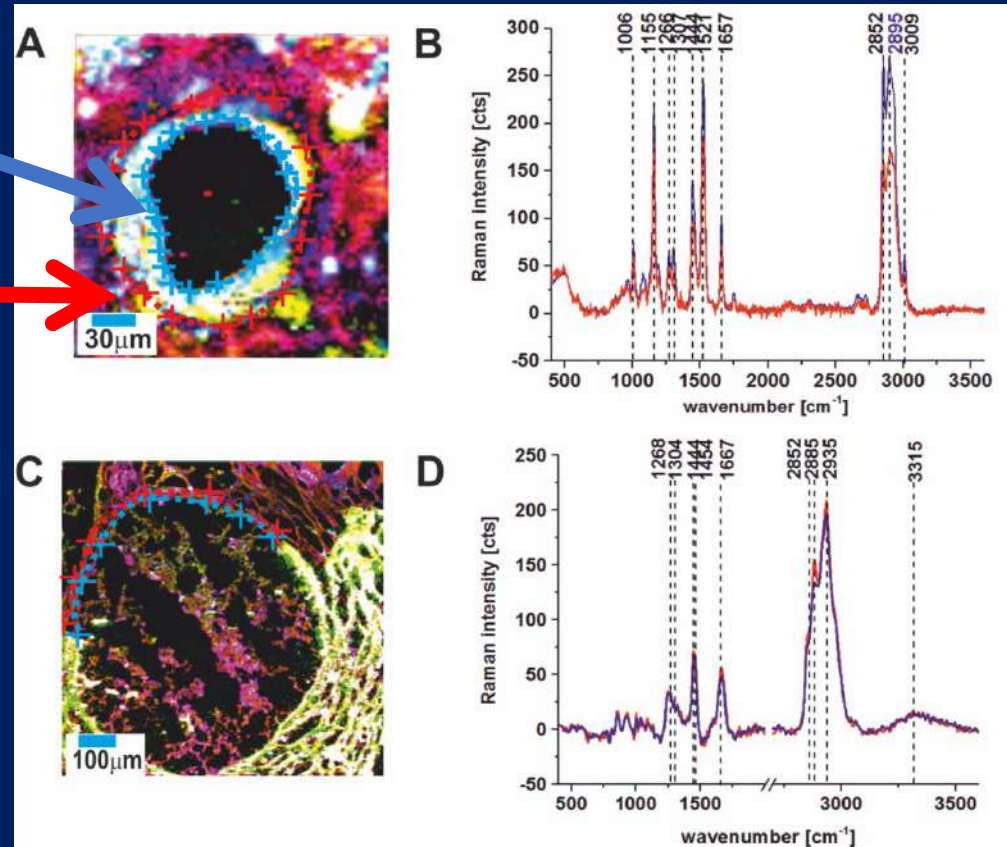
The common feature of cells is their polarity which refers to cellular asymmetry that reflects the asymmetric organization of the cell including the cell surface, intracellular organelles and the cytoskeleton. Cell polarity is a major regulatory mechanism for controlling spatially restricted signaling, reorganization of the cytoskeleton, and polarized membrane trafficking.

It is worth emphasizing that the Physics definition of polarization is different from the Cell Biology term. In Cell Biology polarity refers to cellular asymmetry that reflects the asymmetric organization of the cell, in physics- the asymmetry in the charge distribution.

APICAL-BASAL POLARITY OF EPITHELIAL CELLS BY RAMAN IMAGING

APICAL

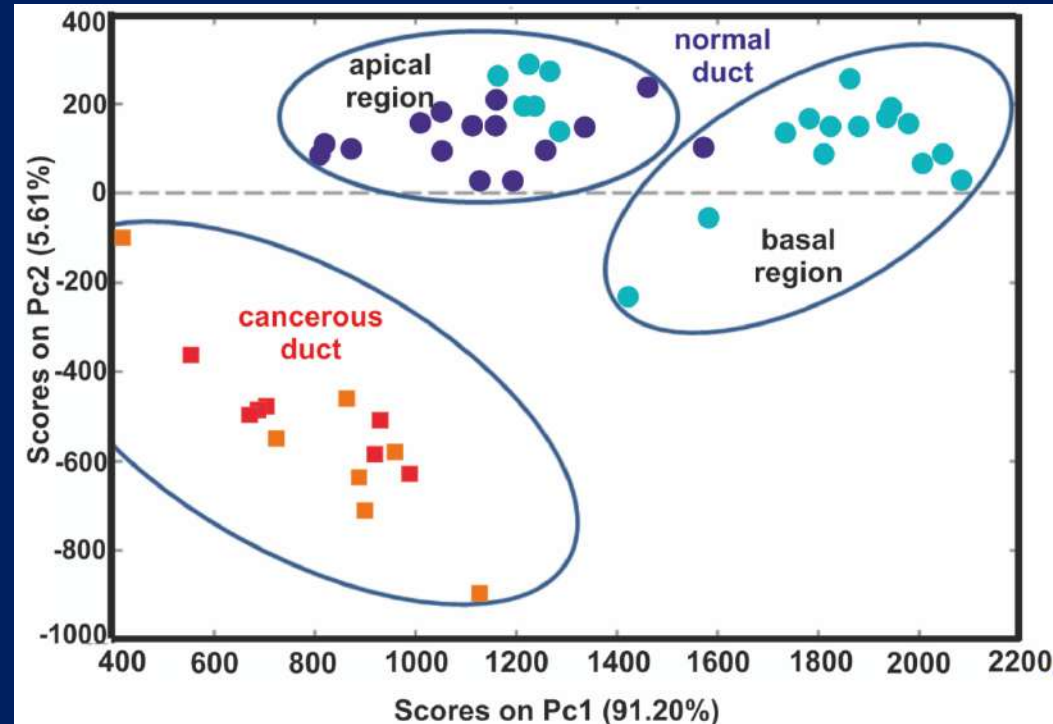
BASAL



Apical - basal polarity of epithelial cells is critical in the correct functioning of an organism and constitutes an important parameter to assess epithelial integrity and homeostasis. Loss of cell polarity results in epithelial tissue disorganization and is a hallmark of cancer development.

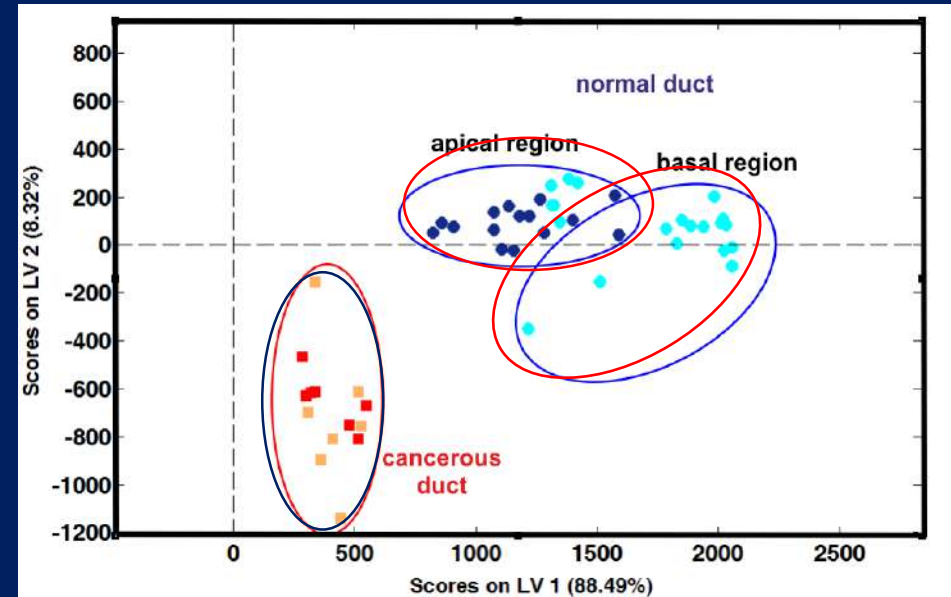
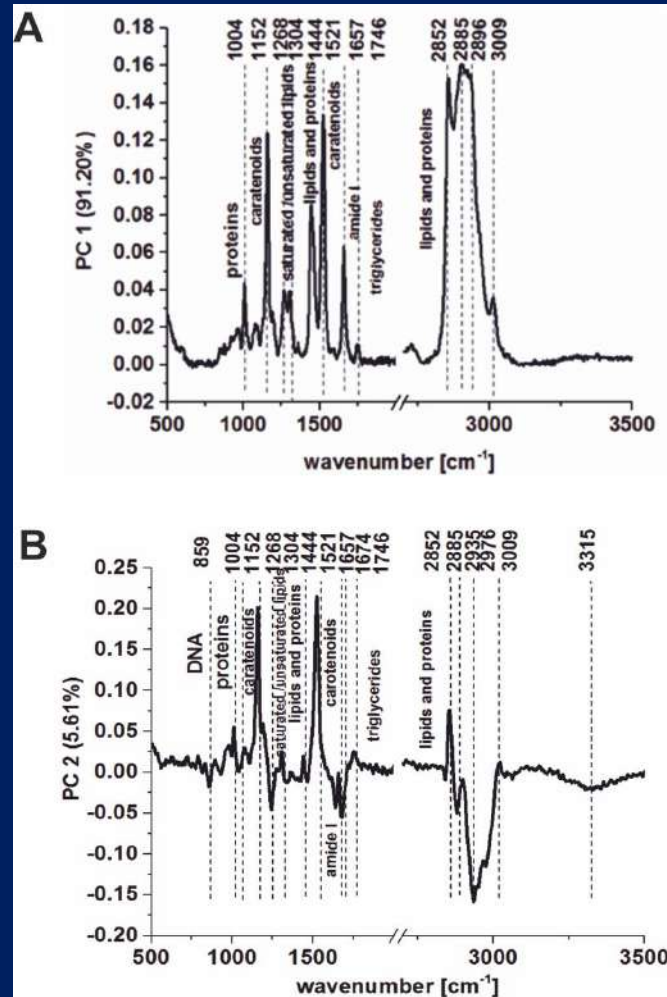
The common feature of cancer development is the increased loss of cell polarity that results in epithelial tissue disorganization. Despite intense interest in determining the origin of tumor tissue disorganization, the function of cell polarity remains unclear. In the study we traced the epithelial cell asymmetry and concentration gradient of main constituents of the cells along the apical-basal axis and monitored ordering at the apical membranes compared to basal membranes in normal and cancerous human breast duct.

APICAL-BASAL POLARITY OF EPITHELIAL CELLS BY RAMAN IMAGING



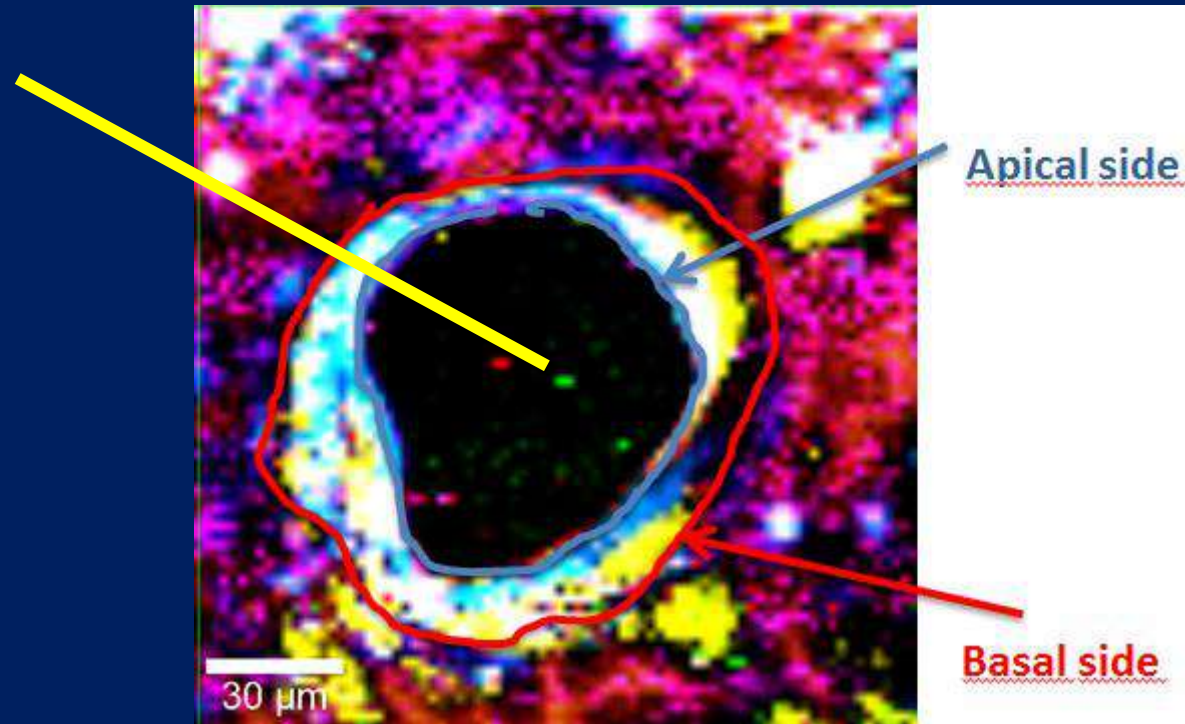
The common feature of cancer development is the increased loss of cell polarity that results in epithelial tissue disorganization. Despite intense interest in determining the origin of tumor tissue disorganization, the function of cell polarity remains unclear. We traced the epithelial cell asymmetry and concentration gradient of main constituents of the cells along the apical-basal axis and monitored ordering at the apical membranes compared to basal membranes in normal and cancerous human breast duct.

APICAL-BASAL POLARITY OF EPITHELIAL CELLS BY RAMAN IMAGING



The results of the PCA reveal separation of the ApM and BaM in normal duct (upper side of the PCA plot). The differences are clearly visible by grouping the Raman spectra of the normal duct in two separate clusters (navy blue and blue points) corresponding to the ApM and BaM samples, where the spectra with similar or identical Raman vibrational properties for the samples from the ApM (navy blue points) are grouped in the upper left area while the samples from the BaM (blue points) are grouped in the upper right area of the plot. The PCA separation indicates that statistically the normal duct is polarized with asymmetric distribution of lipids, proteins, carotenoids, triglycerides on the ApM and BaM sides. An inverse situation occurred in cancerous duct where there is no separation between ApM and BaM, both samples from the ApM (red points) and BaM (orange points) are grouped in the lower area of the PCA plot. It indicates that there are much more similarities than differences between ApM and BaM, which reflects lack of differentiation in the cancerous duct that lost apical polarity upon cancer development.

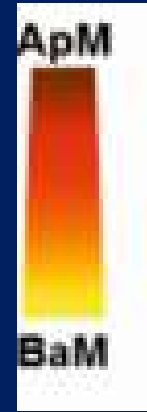
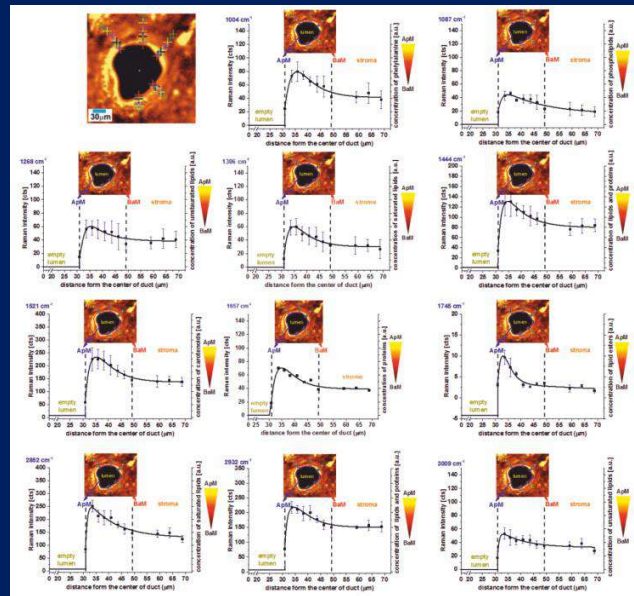
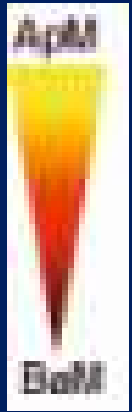
APICAL-BASAL POLARITY OF EPITHELIAL CELLS BY RAMAN IMAGING



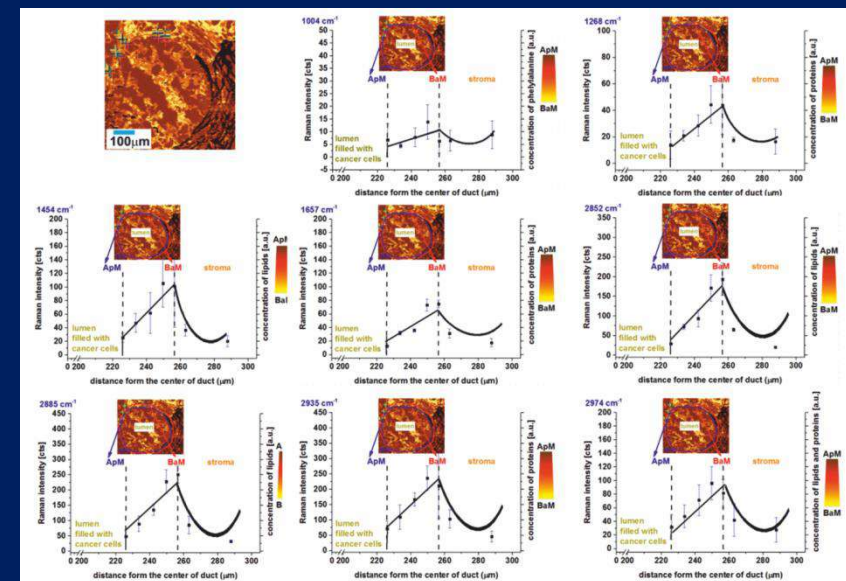
Here, we show the concentration gradient of main constituents of the cells along the apical-basal axis.

APICAL-BASAL POLARITY OF EPITHELIAL CELLS BY RAMAN IMAGING

NORMAL CELLS



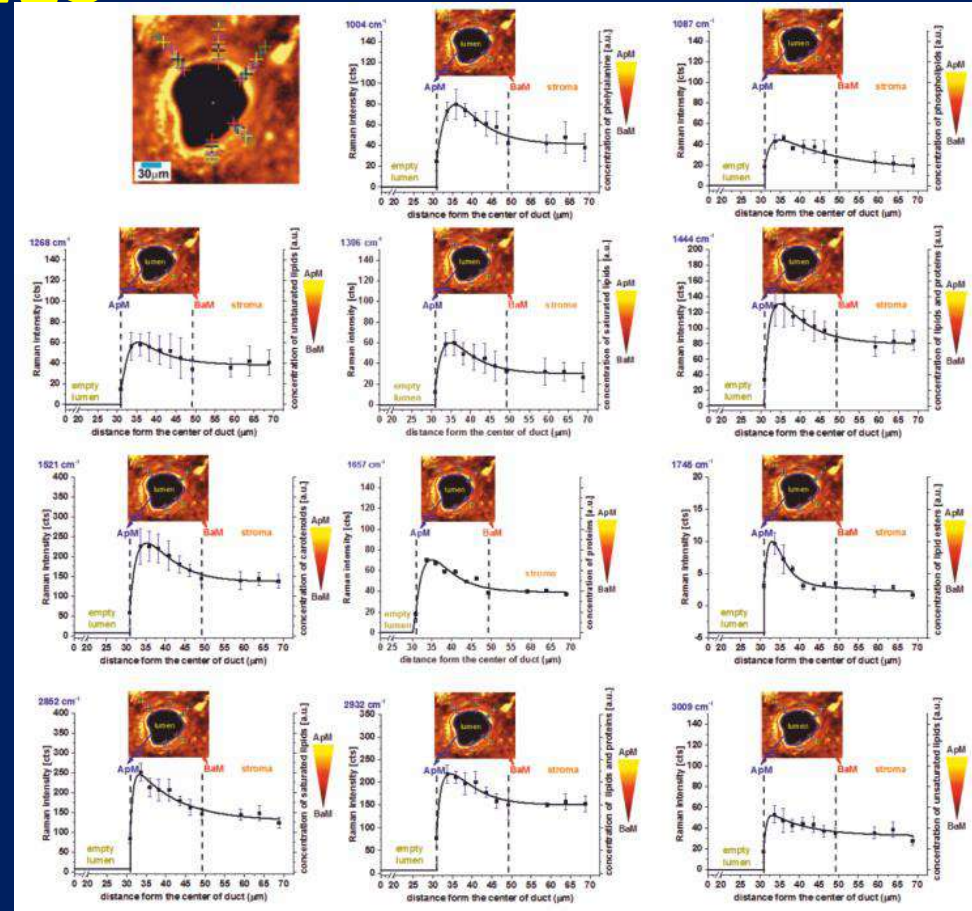
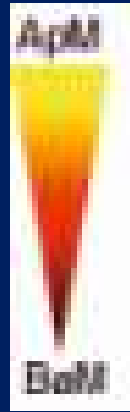
CANCEROUS CELLS



Here, we show the concentration gradient of main constituents of the cells along the apical-basal axis. The radial distribution functions of concentration of major components of the normal and cancerous epithelial cells are presented. The concentration of these chemical components decreases along the apical-basal axis. The apical region of the normal duct is rich in unsaturated triglycerides derived from oleic acid (glyceryl trioleate), carotenoids and proteins.

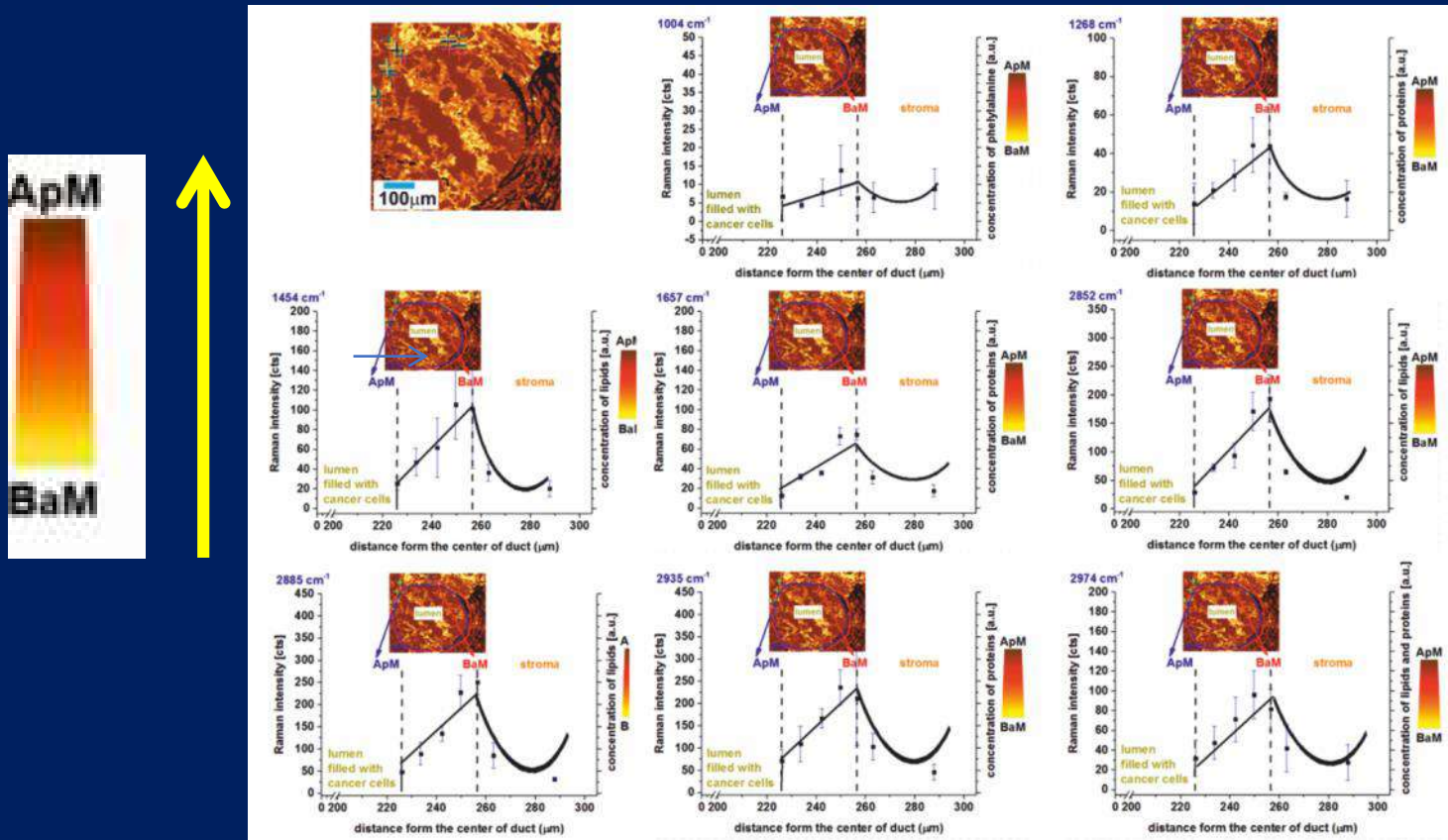
Our results reveal that the normal duct is polarized with asymmetric distribution of lipids, proteins, carotenoids, triglycerides and that an inverse situation occurred in duct that lost apical polarity upon cancer development.

APICAL-BASAL POLARITY OF EPITHELIAL NORMAL CELLS



The concentration of these chemical components decreases along the apical-basal axis for the normal epithelial cells. The apical region of the normal duct is rich in monounsaturated triglycerides derived from oleic acid (glyceryl trioleate), carotenoids and proteins.

APICAL-BASAL POLARITY OF EPITHELIAL CANCER CELLS



An inverse situation occurred in duct that lost apical polarity upon cancer development. The concentration of these chemical components increases along the apical-basal axis for the cancer epithelial cells.

HOW DOES RAMAN SPECTROSCOPY AND IMAGING BENEFIT CANCER RESEARCH?

- **EPIGENETIC MODIFICATIONS**

EPIGENETICS BY RAMAN IMAGING

2017

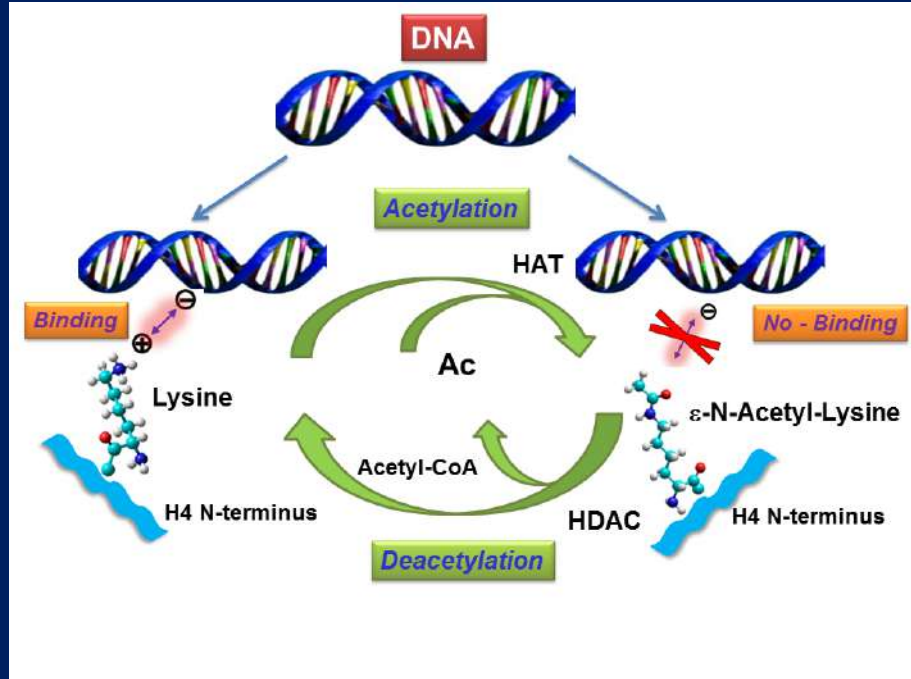
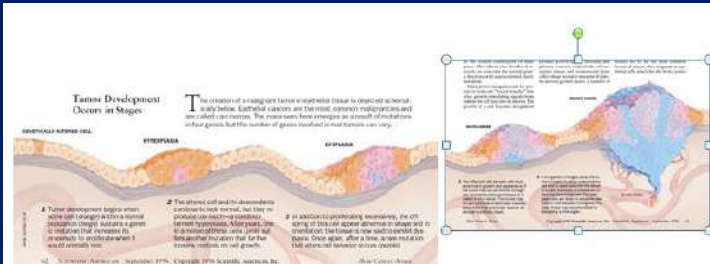
Issue 48, 2016

Analytical Methods

From the journal:
Analytical Methods

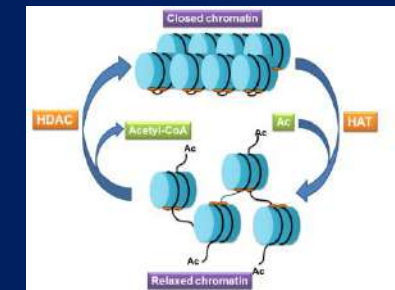
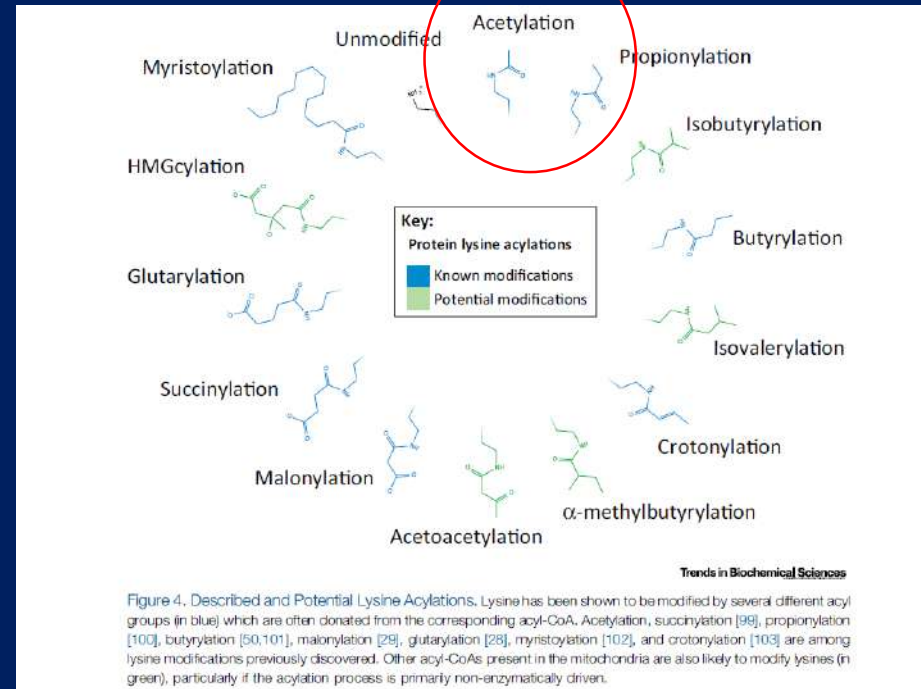
Development of a new diagnostic Raman method for monitoring epigenetic modifications in the cancer cells of human breast tissue

Beata Brozek-Pluska,^a Monika Kopec^c and Halina Abramczyk^{*a}



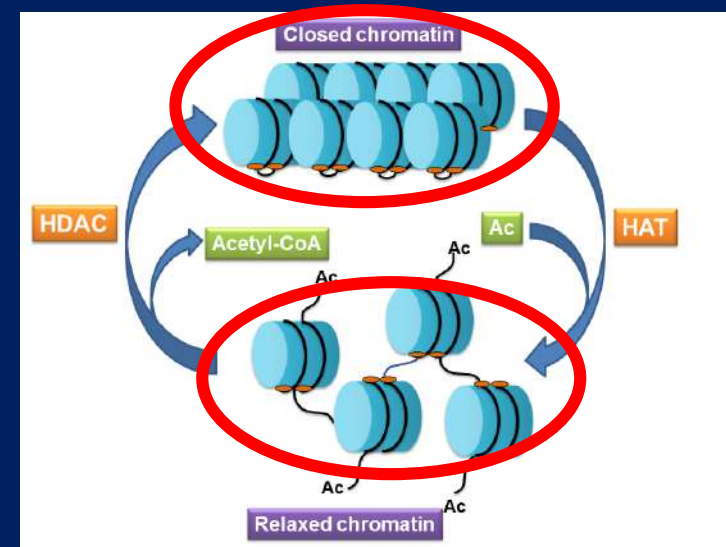
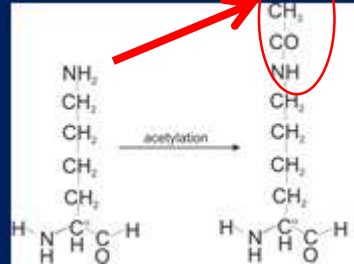
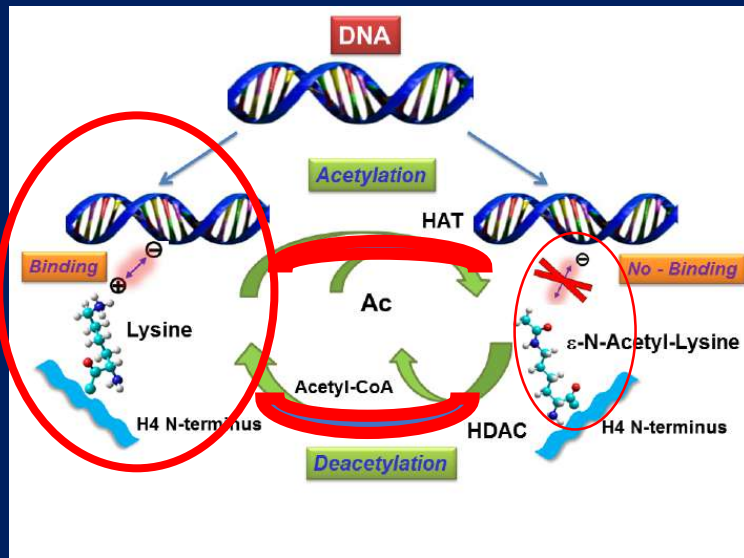
For many years it was thought that cancer is a genetic disease in which changes in the sequence of certain genes, oncogenes and tumor suppressors cause the disease. In recent years it has become evident, however that changes in cancer are also based on the epigenetic factors such as DNA methylation and histone acetylation, phosphorylation that modify transcriptional and posttranslational potential of the cell.

EPIGENETIC MODIFICATIONS



Now is just the beginning of our understanding of epigenetic factors involved in development of cancer diseases, but it has become evident that cancer cells have many epigenetic differences compared to normal cells in the same patient. The list of all possible epigenetic modifications is not yet complete, but it is obvious that in the future the manipulation of the epigenetic landscape will become a key element of cancer therapy . We have concentrated on Lysine acetylation and methylation because they are involved in diverse cellular processes, such as chromatin remodeling.

EPIGENETICS BY RAMAN IMAGING



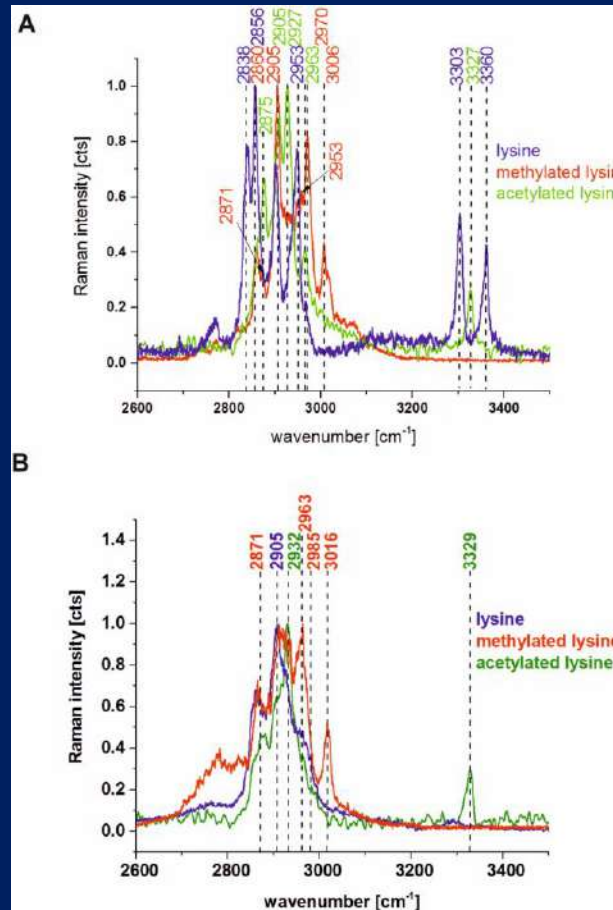
Here we can see interaction between DNA and histone protein via lysine residue. Briefly, mechanism of acetylation and deacetylation presented in Fig. 1 is maintained by opposing activities of histone acetyltransferases (HAT) and deacetylases (HDAC). The acetylation transfers an acetyl group from acetyl CoA to form ϵ -N-acetyl lysine. The acetylation mechanism induced by HAT is particularly important in post translational alterations of histone proteins, because the positive charge of the histone tail can be changed to neutral by acetylation. Ultimately, such a modification leads to weaker binding via electrostatic forces between the histone proteins and DNA of the nucleosome components that results in structure alteration of chromatin (less compact euchromatin) and affects the expression of genes making them more active. The opposite effect is due to the HDAC, which removes the acetyl groups from the lysine residues, making the DNA more tightly wrapped around the histone cores (and resulting in a repression of gene activity known as a gene silencing). These opposite effects of HAT/HDAC on chromatin structure are presented in Fig. 2.

Few meters of DNA; wound on the histones- proteins found in eukaryotic cell nuclei

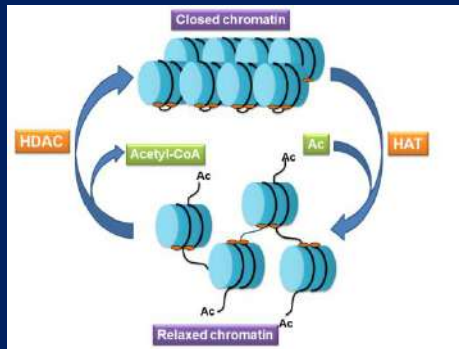
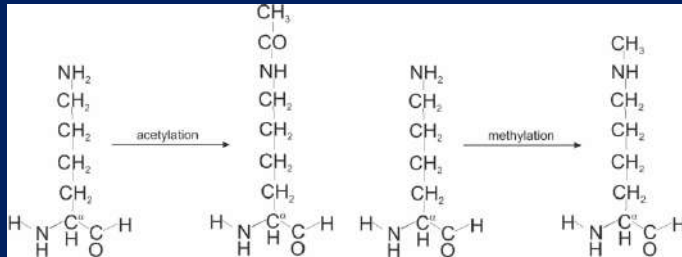
EPIGENETICS BY RAMAN IMAGING

- **We developed a novel Raman based alternative for currently existing epigenetics research approaches. The proposed Raman approach can 'upgrade' cancer epigenetic tests and answer many questions by monitoring the biochemistry of cancer cells.**

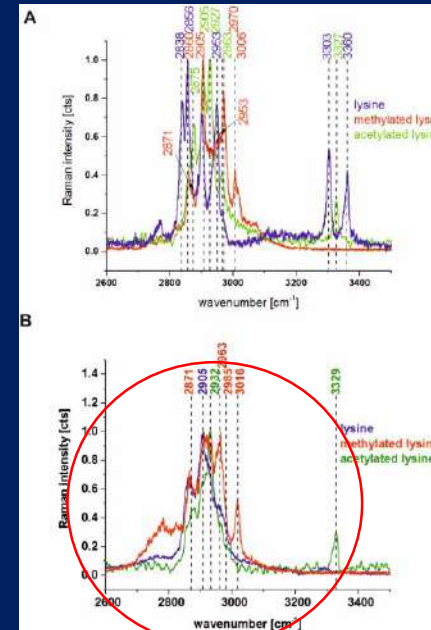
NON-INVASIVE MONITORING OF EPIGENETIC MODIFICATIONS BY RAMAN IMAGING



EPIGENETICS BY RAMAN IMAGING



Histone acetylation/deacetylation by HAT and HDAC enzymes alters chromatin structure by decreasing/increasing accessibility of exposed sites on DNA to silencing/activating gene transcription.

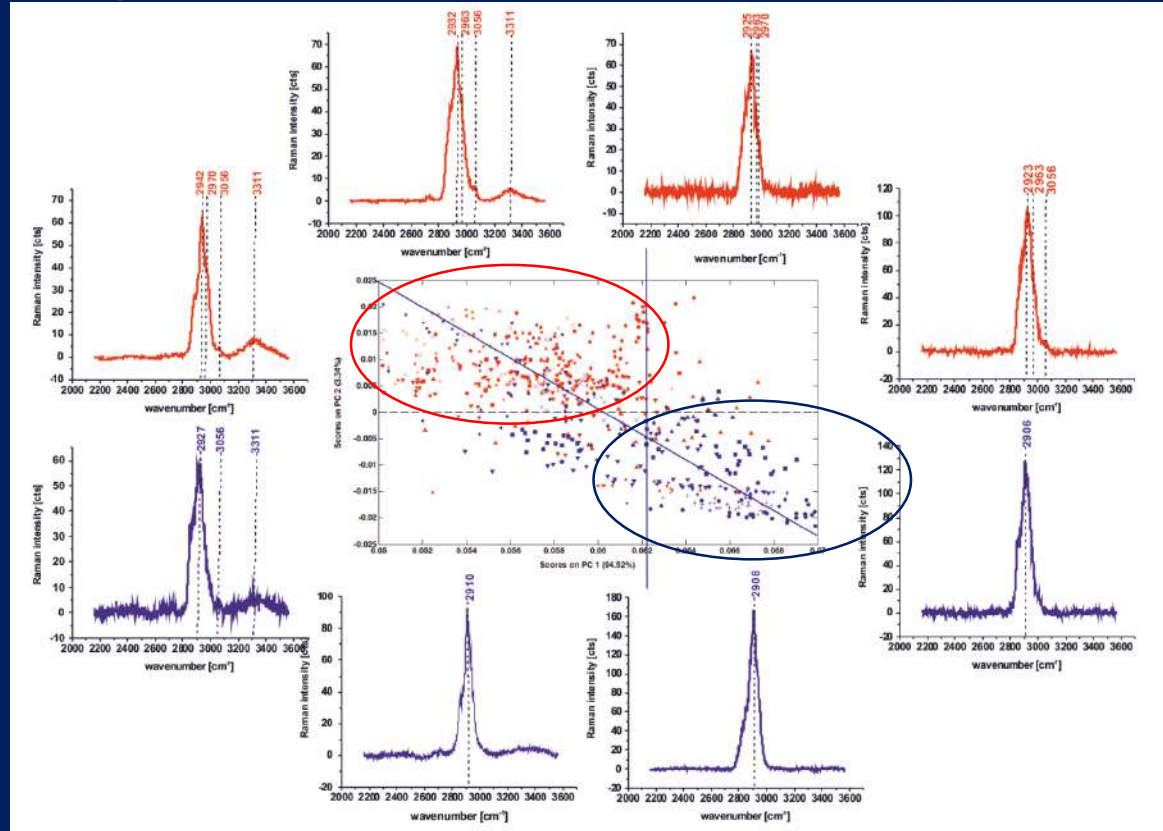


Raman spectrum of lysine, acetylated lysine and methylated lysine, solid crystalline powder (A), Raman spectrum of lysine, acetylated lysine and methylated lysine amorphous phase evaporated from aqueous solution $c=10^{-2}$ M (B).

Raman spectroscopy and Raman imaging have strong diagnostic potential for monitoring acetylation and methylation processes in cancer cells of human breast tissues. We will show that Raman spectroscopy and Raman imaging can detect the relative amounts of acetylated and methylated lysine by monitoring the vibrations of the acetyl and methyl chemical functional groups. In comparison to existing tests and assays, Raman-based methods represent a powerful alternative that allows non-invasively detect cellular acetylation and methylation processes that are not limited to only those events that are sensitive to a specific antibody.

EPIGENETICS BY RAMAN IMAGING

In order to visualize chemical similarities and differences in level of acetylation and methylation in cancerous and normal tissues we have evaluated the predictive validity and potential of Raman spectroscopy by using multivariate statistical methods for data interpretation.

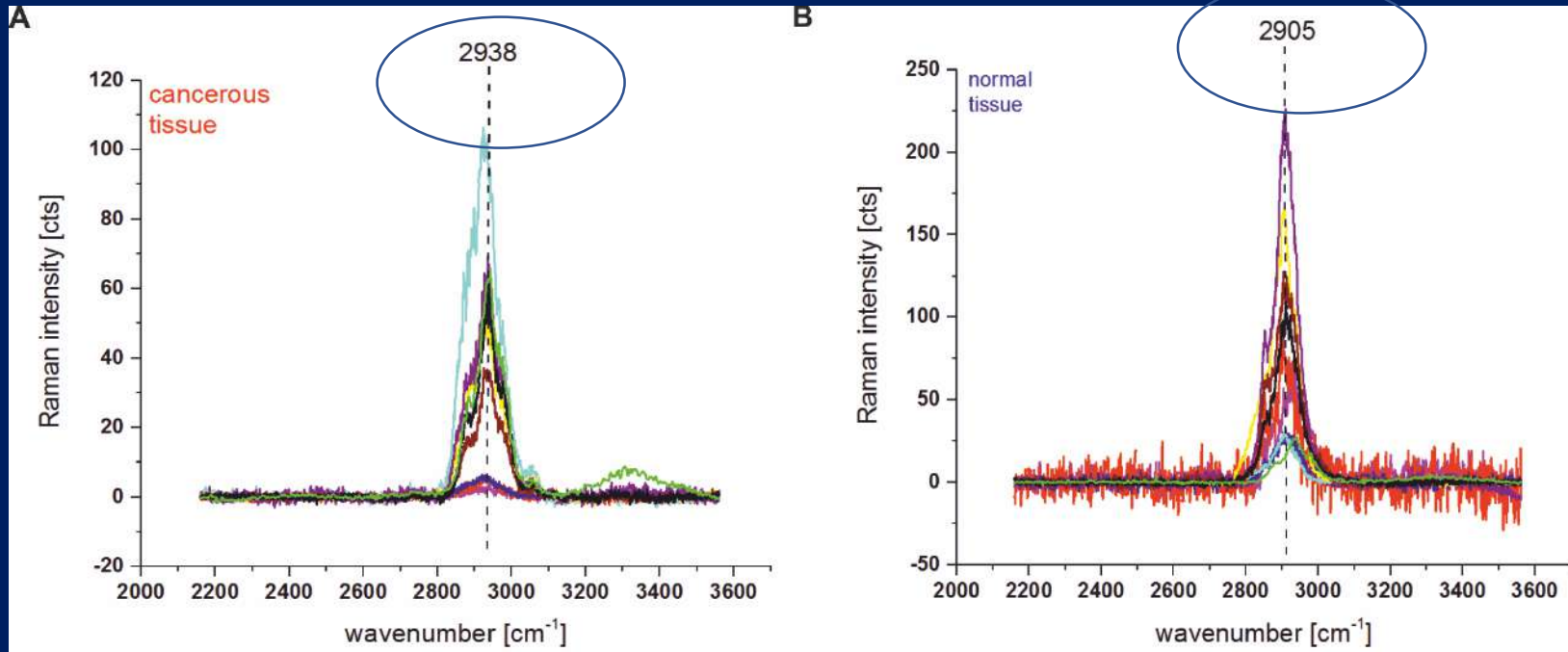


The results of the PCA reveal separation of the cancer and normal tissues. The similarities and differences are clearly visible by grouping the Raman spectra in two separate clusters, where the spectra with similar or identical vibrational properties for the samples from the tumor mass (red points) are grouped in the upper area while the samples from the safety margin (blue points) are grouped in the lower area of the plot.

PCA score plot (model: area normalized to 1) for the Raman spectra from the region (2000 cm⁻¹ -3700 cm⁻¹) of the human breast tissue samples from the tumor mass (red points) and the safety margin (blue points), integration time 0.5 s, laser power 10 mW;

The characteristic spectra corresponding to the various coordinates of the PC1-PC2 score plot.

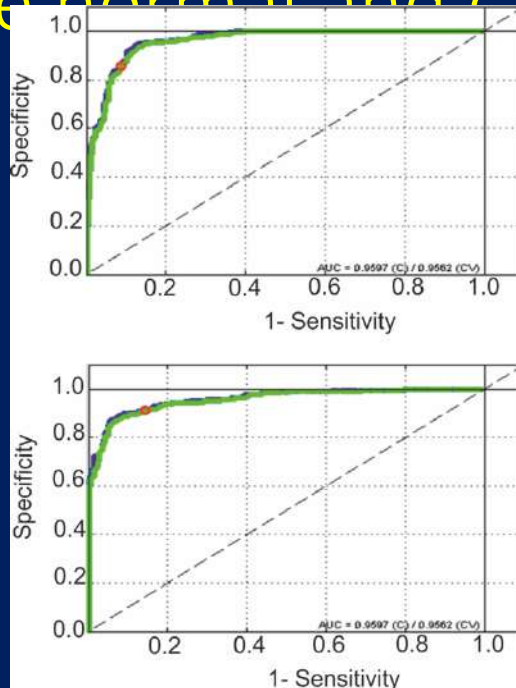
EPIGENETICS BY RAMAN IMAGING



In the view of the results presented so far one can provide strong evidence that the global acetylation level of histone and non-histone proteins increases in human breast cancer cells.

One can see that the samples of the cancerous tissue from the tumor mass have the Raman peak frequency at 2938 cm⁻¹ correlating quite well with the Raman peak position of acetylated lysine. The samples of normal tissue from the safety margin have the Raman peak frequency at 2905 cm⁻¹ corresponding to the vibrations of non-methylated/non-acetylated proteins (CH₂ symmetric stretching vibration).

Bimodal ROC (Receiver operating characteristic) curves graph for the normal and cancerous human samples



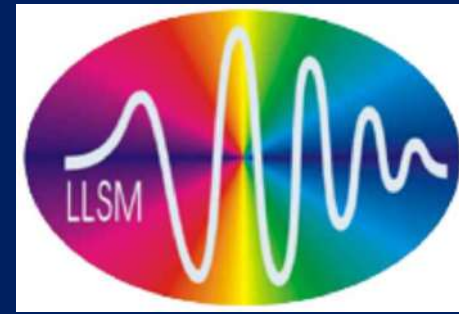
To further evaluate and compare the performance of the PCA and PLSDA based diagnostic algorithm for breast cancer diagnosis, the receiver operating characteristic (ROC) analysis was performed.

Fig. 10 shows a bimodal ROC (Receiver operating characteristic) curves graph for the normal and cancerous human samples. The sensitivity and specificity obtained directly from the ROC curve are 0.861 and 0.913, respectively. The ROC curve in Fig. 10 illustrates the ability of Raman spectroscopy to separate enhanced methylation/acetylation of proteins occurring in cancerous breast tissue. A simulated ROC curve of two indistinguishable populations is included for comparison.

Although PCA method is useful for visualization of data trends, it cannot be used as Supervised Learning classification method, where the previous knowledge of the samples under study must be known. In our case the class membership of every sample is a priori known from a 'gold standard' method of histopathology performed by the certified doctors.

We used supervised learning algorithm PLSDA to calculate the sensitivity .

The sensitivity and specificity obtained directly from PLSDA and cross validation for a chosen model gives a sensitivity and specificity of 86.1% and 91.3% for calibration and 85.3% and 91.3% for cross-validation, respectively.



Novel strategies of Raman imaging for brain tumor research

2017

www.impactjournals.com/oncotarget/

Oncotarget, Advance Publications 2017

Novel strategies of Raman imaging for brain tumor research

Imiela Anna¹, Polis Bartosz², Polis Lech² and Abramczyk Halina¹

¹Lodz University of Technology, Institute of Applied Radiation Chemistry, Laboratory of Laser Molecular Spectroscopy, 93-590 Lodz, Poland

²Polish Mother's Memorial Hospital Research Institute, Department of Neurosurgery and Neurotraumatology, 3-338 Lodz, Poland

Correspondence to: Abramczyk Halina, **email:** abramczy@mitr.p.lodz.pl

Keywords: Raman spectroscopy, Raman imaging, brain tumor, CNS, iodine number

Received: January 21, 2017

Accepted: April 29, 2017

Published: July 28, 2017

The biochemical and nanomechanical signatures of brain cancer

- The development of a variety of cancers is linked to changes both in the biochemical and mechanical properties of living cells and extracellular matrix. Oncogenically transformed cells are expected to have differences in all cell and tissue layers, but it still remains unclear whether a mechanical (stiffness, adhesion) or biochemical alterations are a cause or a consequence of cancer development.

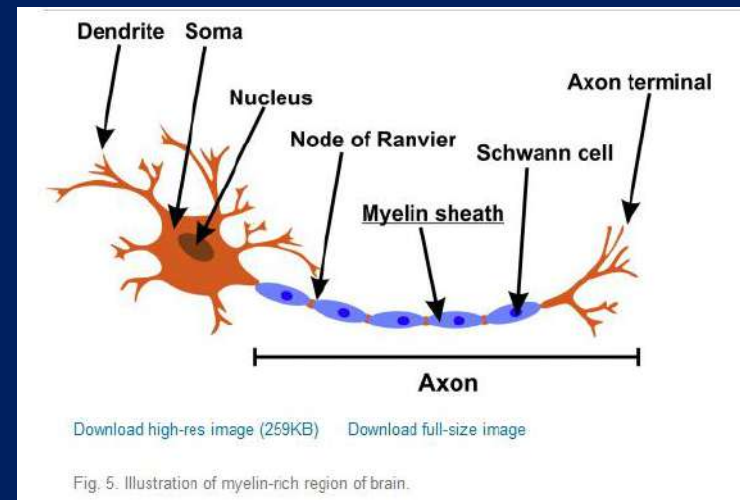
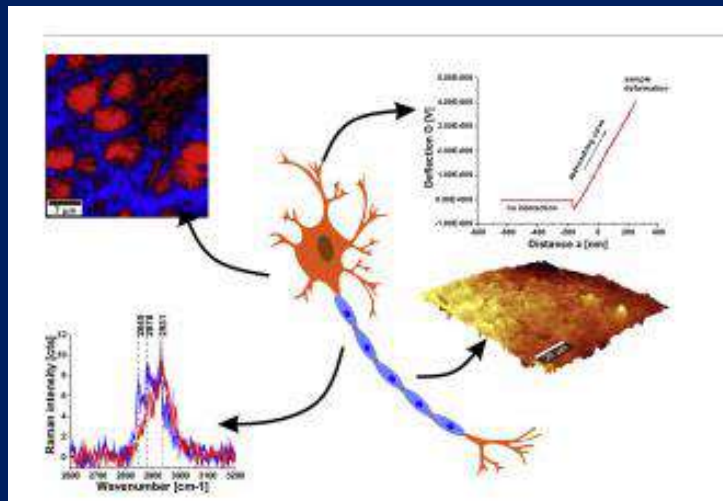
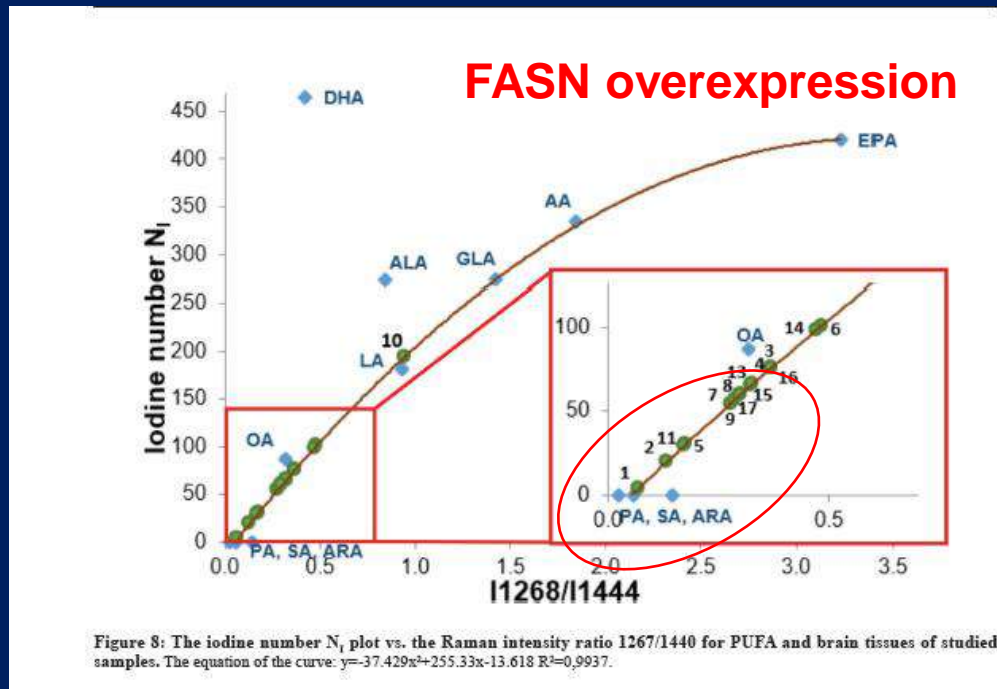


Fig. 5. Illustration of myelin-rich region of brain.

Table 1: Raman intensity ratios at 2930/2845 cm⁻¹ for all analyzed brain tissue samples

Type of cancer	Patient number	Intensity at 2930 cm ⁻¹	Intensity at 2845 cm ⁻¹	Ratio I_{2930}/I_{2845}	Standard deviation
Medulloblastoma WHO grade IV	1	0.07	0.09	0.78	0.010
	2	0.09	0.04	2.32	0.026
	3	0.12	0.05	2.55	0.035
	4	0.10	0.06	1.68	0.021
	9	0.10	0.04	2.62	0.032
Astrocytoma WHO grade II	7	0.11	0.04	3.15	0.038
	8	0.10	0.06	1.77	0.022
Astrocytoma WHO grade I	10	0.11	0.04	2.977	0.037
	14	0.11	0.04	2.63	0.034
Ependymoma WHO grade II	5	0.09	0.04	2.06	0.028
	6	0.08	0.05	1.74	0.018
	11	0.12	0.03	3.81	0.043
Ganglioma WHO grade II	13	0.11	0.06	1.83	0.024
Heamaningioblastoma WHO grade I	15	0.11	0.06	0.87	0.025
Metastatic brain tumor	16	0.11	0.05	1.96	0.026
Normal brain tissue	17	0.108	0.07	1.46	0.016

The iodine number N_i plot vs the Raman intensity ratio 1268/1444 for PUFA and human brain cancer tissues of studied samples.

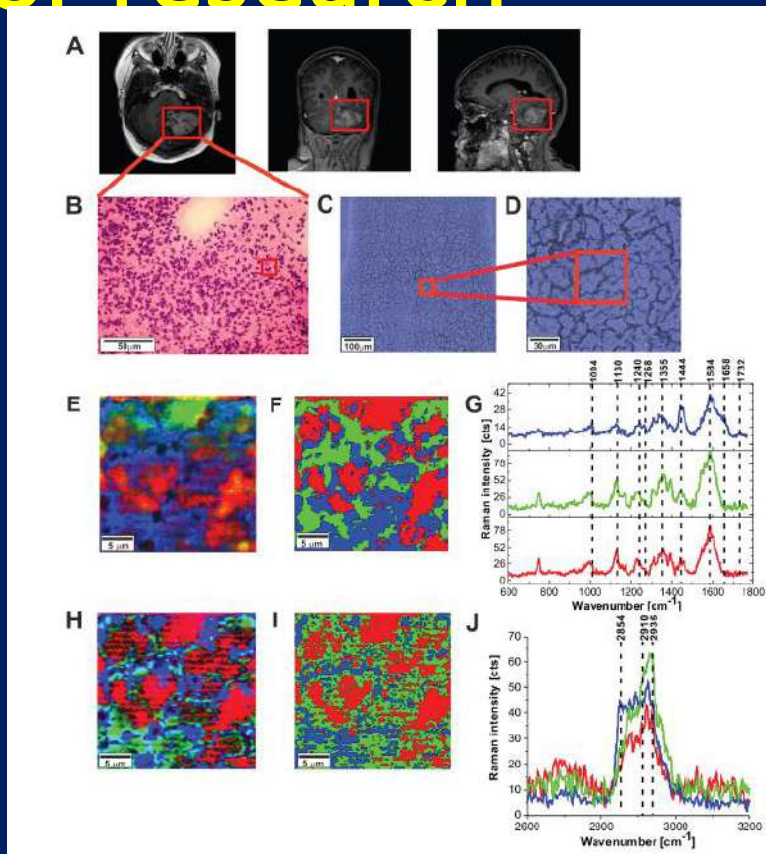


To address these important questions on lipid phenotypic alterations we used the iodine number N_i to characterize tissues. The iodine number N_i is accepted as a good source of information on the amount of unsaturation in fatty acids, where the double bonds react with iodine compounds. The higher the iodine number, the more C=C bonds are present in the fat.^{38,39} We have applied the iodine number plot vs the Raman intensity ratio 1268/1444 measured at 1268 cm^{-1} and 1444 cm^{-1} used as a source of information on the ratio of saturated/unsaturated lipids in the human tissue.

The **iodine value** (or "iodine adsorption value" or "iodine number" or "iodine index") in chemistry is the mass of iodine in grams that is consumed by 100 grams of a chemical substance. Iodine numbers are often used to determine the amount of unsaturation in fatty acids. This unsaturation is in the form of double bonds, which react with iodine compounds. The higher the iodine number, the more C=C bonds are present in the fat

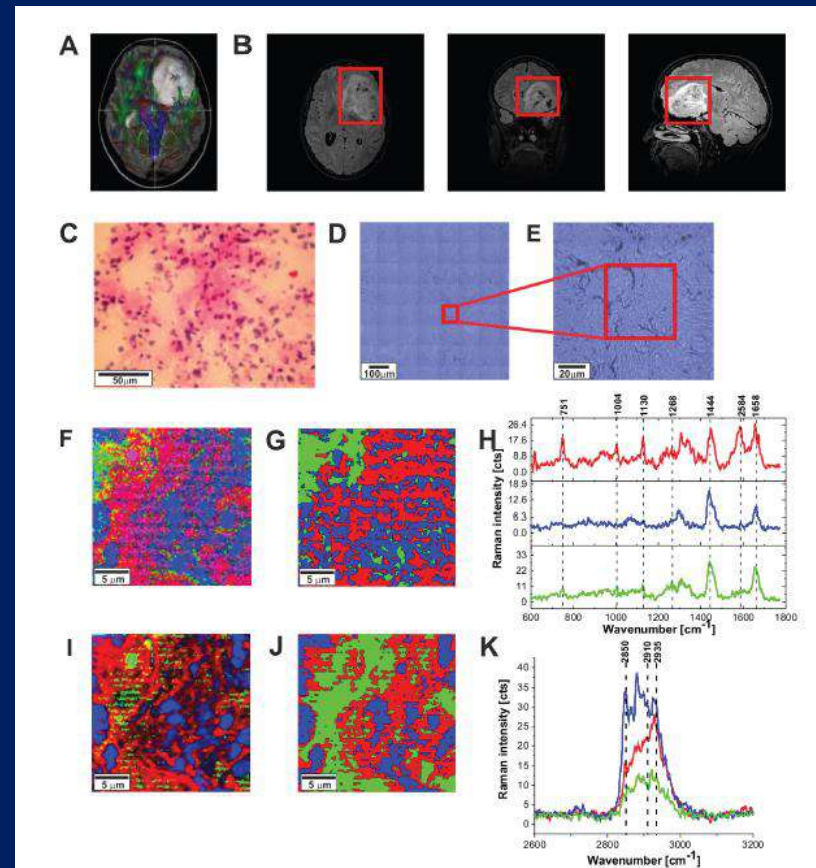
Figure 5 The iodine number N_i plot vs the Raman intensity ratio 1268/1444 for PUFA and human brain cancer tissues of studied samples. palmitic acid (PA), stearic acid (SA), arachidic acid (ARA), oleic acid (OA), linoleic acid (LA), γ -linolenic acid (GLA), arachidonic acid (AA), docosapentaenoic acid (DPA), eicosapentaenoic acid (EPA), α -linolenic acid (ALA), eicosatetraenoic acid (ETA), tetracosahexaenoic acid (THA), docosahexaenoic acid (DHA)

Novel strategies of Raman imaging for brain tumor research



Medulloblastoma , grade IV

Figure 5: The MRI image (A) H&E-stained histological image (B) stitching microscopy image (520 $\mu\text{m} \times 520 \mu\text{m}$) (C) microscopy image (155 $\mu\text{m} \times 155 \mu\text{m}$) (D) Raman images (50 $\mu\text{m} \times 50 \mu\text{m}$) obtained by basis analysis (E) and cluster analysis (F) and the characteristic vibrational Raman spectra in the fingerprint frequency region (G) Raman images (50 $\mu\text{m} \times 50 \mu\text{m}$) obtained by basis analysis (H) and cluster analysis (I) and the characteristic vibrational Raman spectra in the high frequency region (J) of the tumor CNS (medulloblastoma, grade WHO IV, infratentorial, Left cerebellar hemisphere) (P9). The line colors of the spectra correspond to the colors of the Raman maps. Raman integration time for images 0.5 s, resolution step: 1 μm , laser excitation power: 10m W.



Astrocytoma , grade II

Figure 9: The tractography image (A) MRI image (B) H&E-stained histological image (C) stitching microscopy image (550 $\mu\text{m} \times 550 \mu\text{m}$) (D) microscopy image (120 $\mu\text{m} \times 120 \mu\text{m}$) (E) Raman image (50 $\mu\text{m} \times 50 \mu\text{m}$) by basis analysis (F) and cluster analysis (G) and the characteristic vibrational Raman spectra in the fingerprint frequency region (H) Raman image (50 $\mu\text{m} \times 50 \mu\text{m}$) by basis analysis (I) and cluster analysis (J) and the characteristic vibrational Raman spectra in the high frequency region (K) of the tumor (Astrocytoma fibrillare, grade WHO II) (P9). The line colors of the spectra correspond to the colors of the Raman maps. Raman integration time for images 1s for low frequencies and 0.5 s for high frequencies, resolution step: 1 μm , laser excitation power: 10m W.

Novel strategies of Raman imaging for brain tumor research

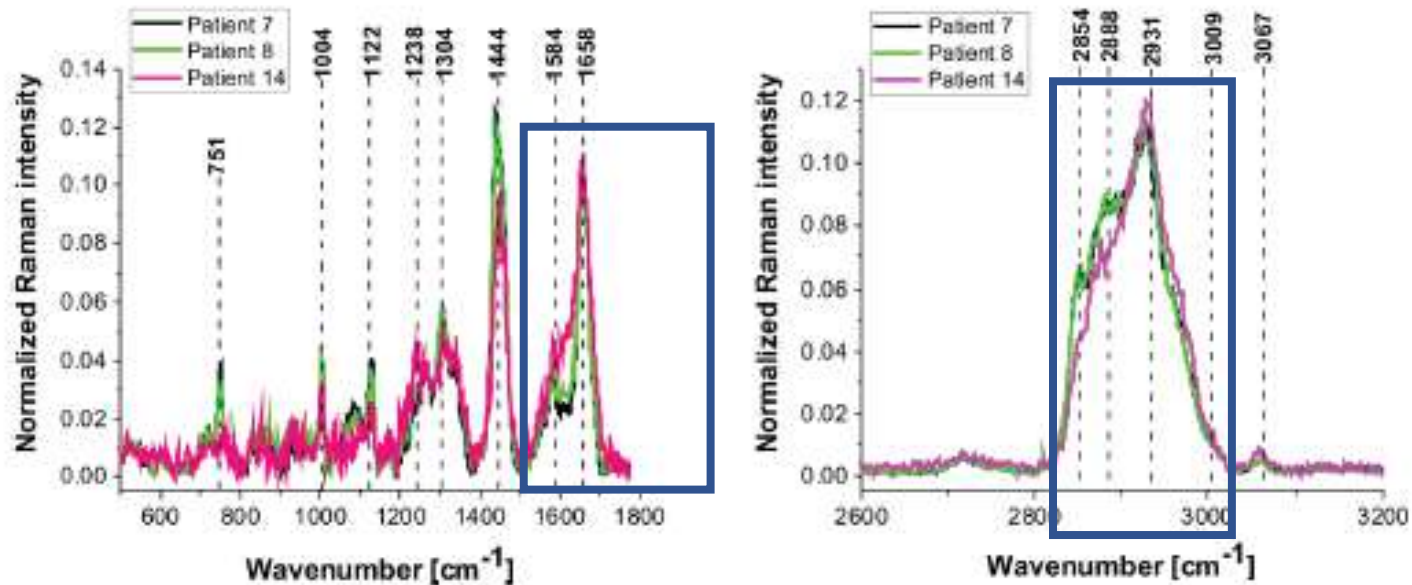


Figure 10: The average vibrational Raman spectra in the low and high frequency region for different areas of the low-grade brain tumor (astrocytoma, grade WHO I and II) (P7, P8, P14), Raman integration time for images 0.5 s for high frequency and 1s for low frequency region, resolution step: 1 μm , laser excitation power: 10m W.

Astrocytoma , grade II

Novel strategies of Raman imaging for brain tumor research

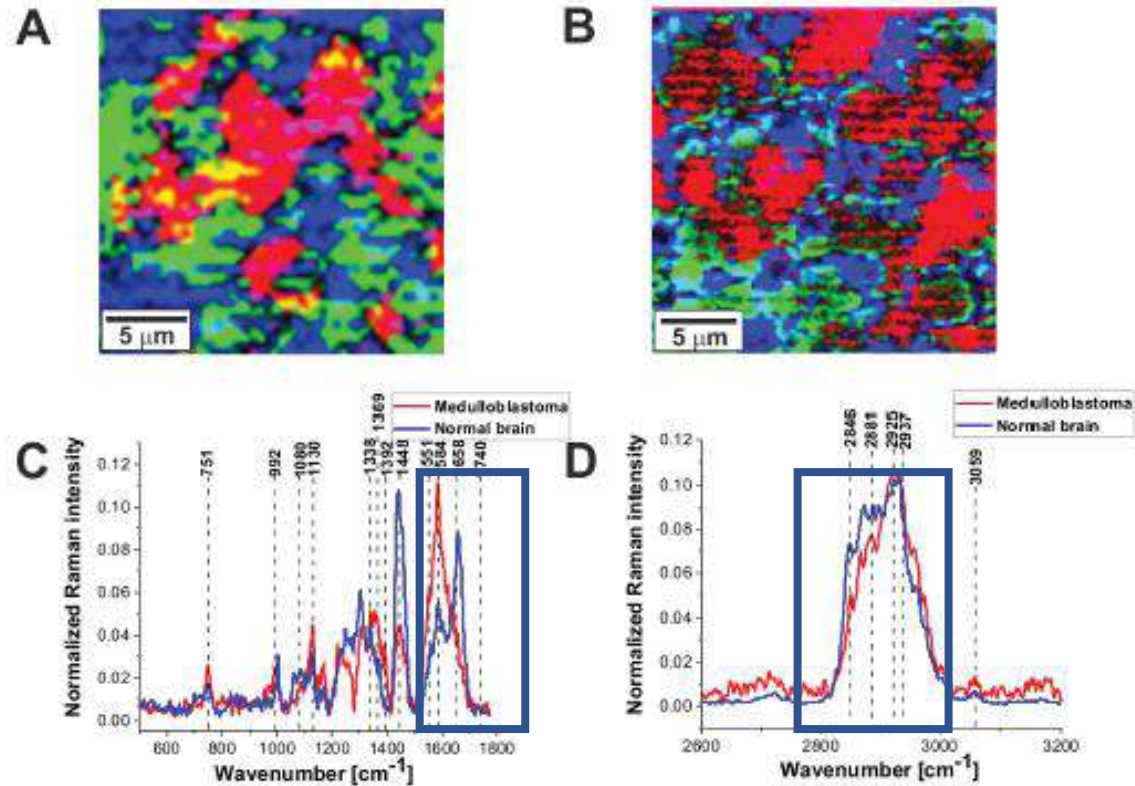


Figure 6: The comparison of the Raman images of the normal (A) and tumor (medulloblastoma, grade WHO IV) (B) tissues. The average vector normalized Raman spectra in the fingerprint region (C) and the high frequency region (D) for the high-grade medulloblastoma (medulloblastoma, grade WHO IV, infratentorial. Left cerebellar hemisphere) (P9), compared with the spectra for normal brain.

Medulloblastoma , grade IV

Novel strategies of Raman imaging for brain tumor research

- We have found that metabolism of proteins, nucleic acids, and lipids is markedly deregulated in malignant medulloblastomas. Our results indicates marked metabolic differences between high grade medulloblastoma and normal brain tissue. The Raman spectra for high-grade brain tumors show many significant differences compared to the normal brain spectra. Detailed inspection shows notable differences in vibrations of proteins, lipids, and nucleic acids:

Novel strategies of Raman imaging for brain tumor research

- 1) the high grade tumors of central nervous system (medulloblastoma) exhibit enhanced level of β -sheet conformation and down-regulated level of α -helix conformation when comparing against normal tissue.
- 2) almost all tumors studied in the paper have increased Raman signals of nucleic acids. This increase can be interpreted as increased DNA/RNA turnover in brain tumors.
- 3) The ratio of Raman intensities I₂₉₃₀/I₂₈₄₅ at 2930 and 2845 cm⁻¹ is a good source of information on the ratio of lipid and protein contents. We have found that the ratio reflects the different lipid and protein contents of tumorous brain tissue compared to the non-tumor tissue. Almost all brain tumors have the Raman intensity ratios significantly higher than that found in non-tumor brain tissue, and indicates that the relative amount of lipids compared to proteins is significantly higher in the normal brain tissue.
- 4) We found that levels of the saturated fatty acids were significantly reduced in the high grade medulloblastoma samples compared with non-tumor brain samples and low grade astrocytoma. Differences were also observed in the n-6/n-3 PUFA (polyunsaturated FA) content for medulloblastoma and non-tumor brain samples. The content of the oleic acid (OA) was significantly smaller in almost all brain high grade brain tumors than that observed in the control samples. It indicates that the fatty acid composition of human brain tumors is different from that found in tumor-free brain tissue.

Angiogenesis - a crucial step in breast cancer growth, progression and dissemination by Raman imaging



Spectrochimica Acta Part A: Molecular and Biomolecular
Spectroscopy

Volume 198, 5 June 2018, Pages 338-345



Angiogenesis - a crucial step in breast cancer growth, progression and dissemination by Raman imaging

Monika Kopeć, Halina Abramczyk  

[Show more](#)

<https://doi.org/10.1016/j.saa.2018.02.058>

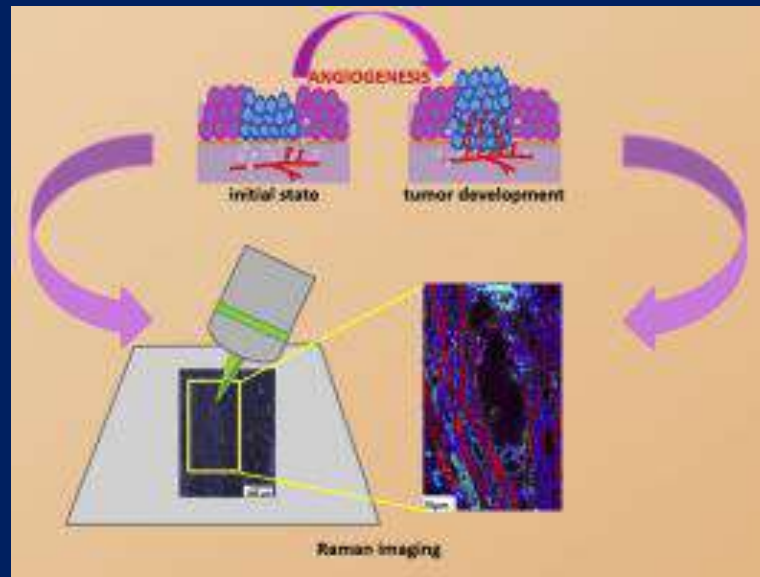
[Get rights and content](#)

2018

Highlights

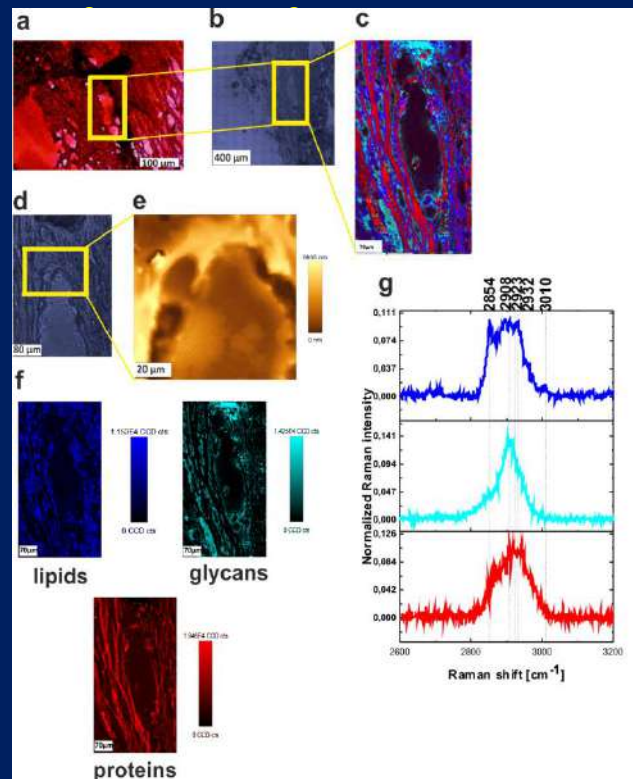
- Raman imaging allows monitoring angiogenesis during cancer development.
- Raman imaging visualizes collagen-fibroblast-glycocalyx network around the blood vessel.
- Raman imaging allows distinguishing between collagen type I and III.
- The iodine value provides information on level of unsaturation in cancer tissue.

Angiogenesis - a crucial step in breast cancer growth, progression and dissemination by Raman and AFM imaging

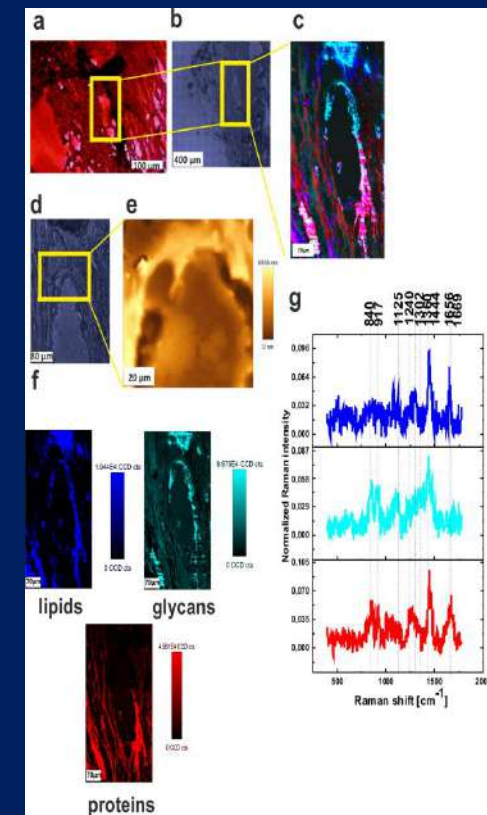


Angiogenesis, the process of new blood vessel formation, plays a central role in both local tumor growth and distant metastasis in breast cancer, because like healthy cells, cancer cells cannot live without oxygen and nutrients. The diversity of responsible angiogenic pathways that encourage new blood vessels to grow into the tumor in breast cancer for different tumors has been studied for many years

Angiogenesis - a crucial step in breast cancer growth, progression and dissemination by Raman and AFM

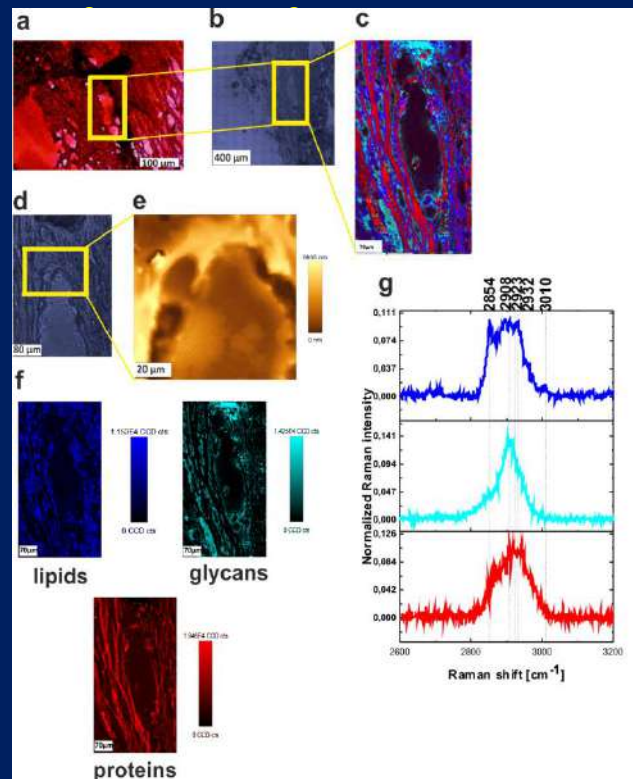


The aim of this study was to use Raman and AFM methods to determine **biochemical composition** around **blood vessels** in **cancerous human breast ex vivo tissue**. Changes of the chemical and structural environment around the blood vessel were reported both in extracellular matrix of a connective tissue and an amorphous ground substance with a pronounced increase of collagen-fibroblast network and glycosaminoglycans, as well as enhanced lactic acid, and glycogene activity in patients affected by breast cancer.

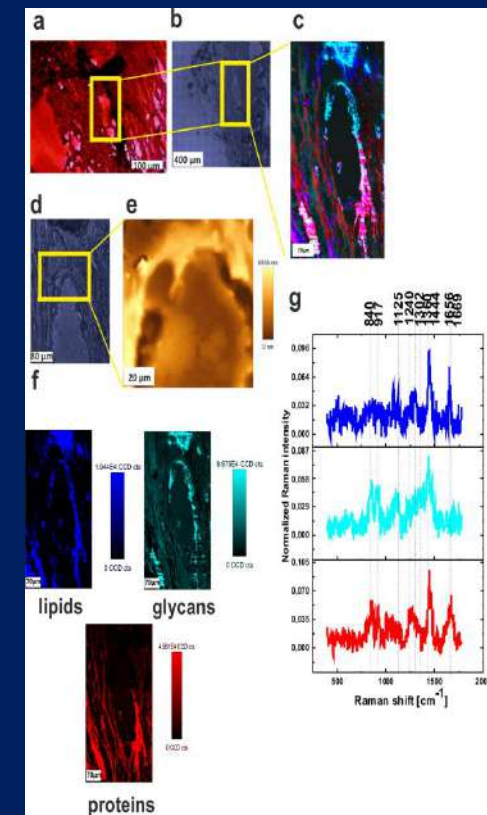


One can see that the matrix constitutes mainly of collagen (green color, Fig. 1c and d)) and lipids (fibroblasts –blue color, and glycan (light blue) Fig. 1 c and d). Cancer cells invade in the collagen and fibroblast network (red color, Fig. 1 c and d). Each collagen fiber is made-up of a variable number of smaller collagen fibrils. These fibrils are composed predominantly of type I collagen, because a characteristic feature of these fibrils is that they exhibit axial periodicity due to the way in which type I collagen assembles to form collagen fibrils. In loose connective tissue, type I collagen is synthesized primarily by fibroblasts, which tend to align

Angiogenesis - a crucial step in breast cancer growth, progression and dissemination by Raman and AFM

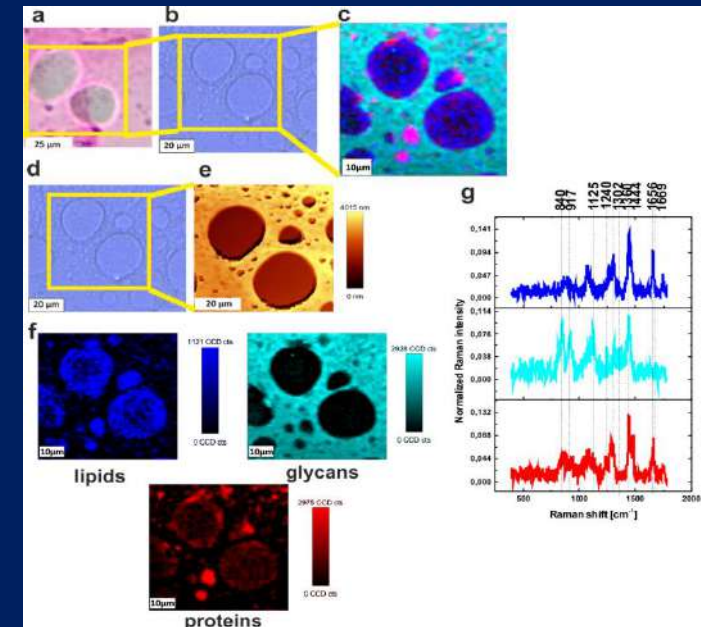
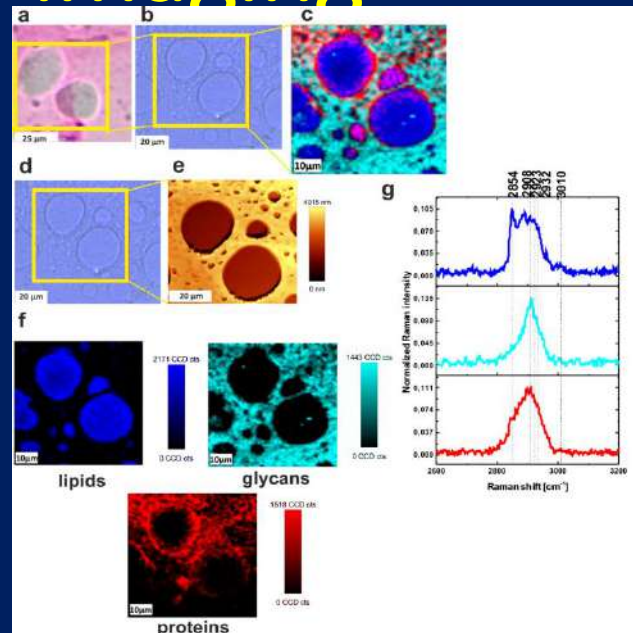


The results presented here demonstrate the central importance of the network of collagen-fibroblast-glycocalyx matrix formed around the blood artery. This matrix seems to be required to protect the balance between rigidity of the environment and deformability of cancer cells to form a stable vascular structure for supplying nutrients and oxygen to the tumor mass. Collagen matrix plays a role of a scaffold that protect the deformable cancer cells.



One can see that the matrix constitutes mainly of collagen (green color, Fig. 1c and d)) and lipids (fibroblasts –blue color, and glycan (light blue) Fig. 1 c and d). Cancer cells invade in the collagen and fibroblast network (red color, Fig. 1 c and d). Each collagen fiber is made-up of a variable number of smaller collagen fibrils. These fibrils are composed predominantly of type I collagen, because a characteristic feature of these fibrils is that they exhibit axial periodicity due to the way in which type I collagen assembles to form collagen fibrils. In loose connective tissue, type I collagen is synthesized primarily by fibroblasts, which tend to align

Angiogenesis - a crucial step in breast cancer growth, progression and dissemination by Raman and AFM imaging



High-resolution of Raman and AFM mapping show that matrix stiffening in tumor progression is due to alteration of biochemical composition of the tumor microenvironment composed of non-cellular (ie, vascular and interstitial) and cellular compartments. We found changes of the chemical, structural around the blood vessel both in intracellular matrix of the connective tissue and in an amorphous ground substance with a pronounced increase of collagen- fibroblast network and glycosaminoglycans. We found that in oncogenically transformed cells enhanced lactic acid, and glycogene activity is observed in breast cancer tissue. In contrast, the normal tissue around the tumor mass does not demonstrate enhanced collagen- fibroblast network. It is dominated by large amount of fat (adipose tissue) and antioxidants ROS.

Angiogenesis - a crucial step in breast cancer growth, progression and dissemination by Raman and AFM imaging

- The results presented here demonstrate the central importance of the network of collagen-fibroblast-glycocalyx matrix formed around the blood artery. This matrix seems to be required to protect the balance between rigidity of the environment and deformability of cancer cells to form a stable vascular structure for supplying nutrients and oxygen to the tumor mass. Collagen matrix plays a role of a scaffold that protect the deformable cancer cells.
- Under the influence of Vascular Endothelial Growth Factor (VEGF), the angioblasts and newly formed endothelial cells migrate on a matrix constituted mainly of collagen and fibroblasts, allowing the fusion of the blood islands, their remodeling into tubular structures, and the formation of the first primitive vascular plexus. These tubules remodel through vasculogenesis into larger vessels, leading to vascularization of a tumor mass

FUTURE DIRECTIONS OF CANCER RESEARCH

Nanooncology: monitoring glycosylation metabolism in brain and breast cancer by Raman and AFM imaging

The last presented topic on angiogenesis of cancer opened a new window for exploration of processes occurring in non-cellular space - glycocalyx –a coat on the external surface of their plasma membranes of epithelial cells consisting of several carbohydrates several carbohydrate moieties of membrane glycolipids and glycoproteins, which serve as backbone molecules for support. Generally, the carbohydrate portion of the glycolipids found on the surface of plasma membranes helps these molecules contribute to cell-cell recognition, communication, and intercellular adhesion.

Functional importance

The epithelial glycocalyx as the epithelial gatekeeper. It is able to limit access of certain molecules to the epithelial cell membrane

The epithelial glycocalyx as mechanotransducer. The epithelium is exposed to mechanical forces. However, the molecule(s) responsible for the translation of biomechanical forces into biochemical signals (mechanotransduction) have not been identified as yet.

GLYCOMICS

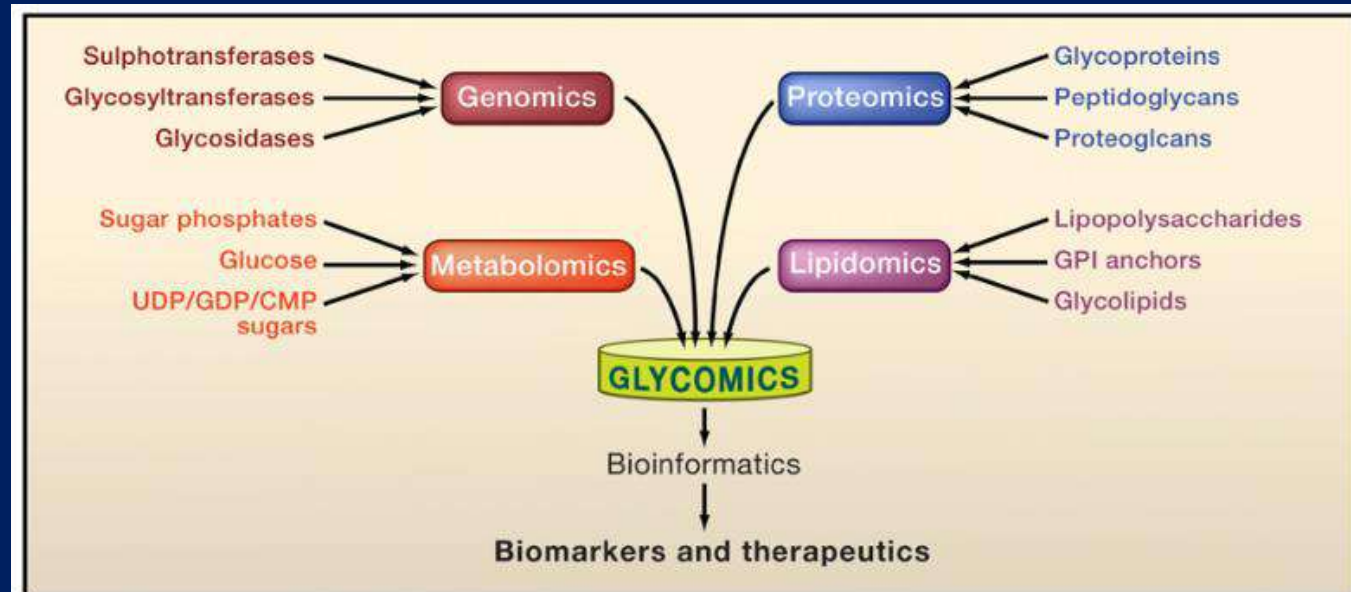


Figure 2. Glycomic Complexity Reflects Cellular Complexity

Given that glycan structures are regulated by metabolism and glyco-enzyme expression and glycans modify both proteins and lipids, functional glycomics also requires the tools of genomics, proteomics, lipidomics, and metabolomics (modified after Packer et al., 2008).

By analogy to the genome, transcriptome, or proteome, the “glycome” is the complete set of glycans and glycoconjugates that are made by a cell or organism under specific conditions.

Visualization techniques- Raman imaging wins once again

- Because of the functional importance of the epithelial glycocalyx, development of direct visualization techniques is crucial to establish its exact role. The glycocalyx can be labeled by administration of specific markers that attach to one or more of its components, making them fluorescent or detectable. The first images of the glycocalyx, made by transmission electron microscopy (TEM) in 1966
- Apparently, the new staining and preparation protocols improved glycocalyx conservation in TEM experiments. However, TEM cannot be used in the in vivo situation.

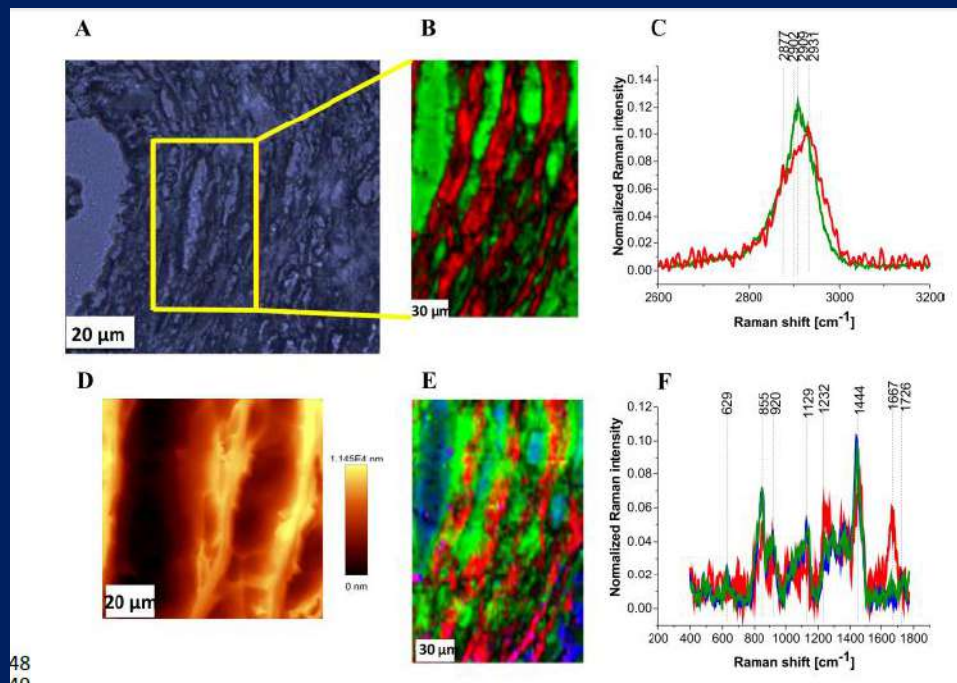
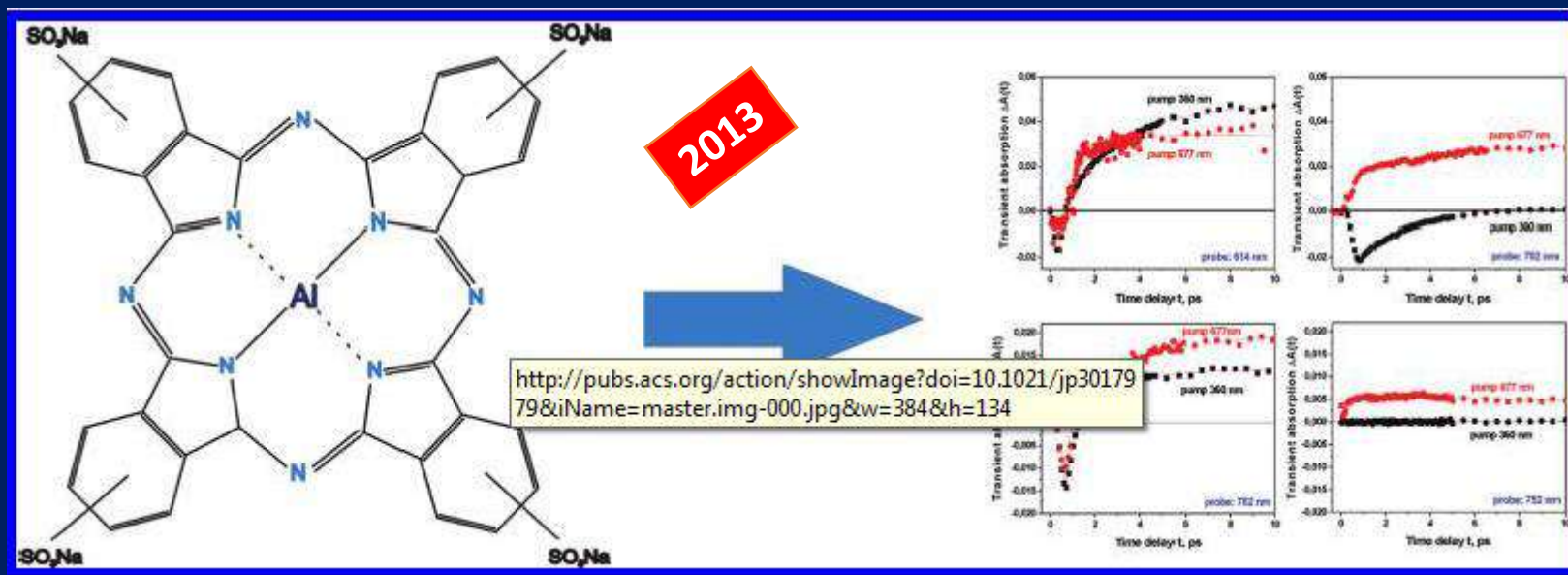


Fig. 6 Distribution of the glycans (green), lipids (blue) and protein (red) in the human breast tumor tissue, the white light microscopy image (A), Raman image (150 μm x 230 μm) obtained from the basis analysis (B) and Raman spectra (C) in the high frequency spectral region. AFM image (D), Raman image obtained from the basis analysis (E) and Raman spectra (F) in the fingerprint region of the tumor breast tissue (Patient P155, Infiltrating adenocarcinoma grade WHO according to Elston and Ellis modification G2), integration time for Raman images 0.5 s in the high frequency region and 1 s in the low frequency region, resolution step 0.5 μm, laser excitation power 10 mW. The line colors of the spectra correspond to the colors of the Raman maps.

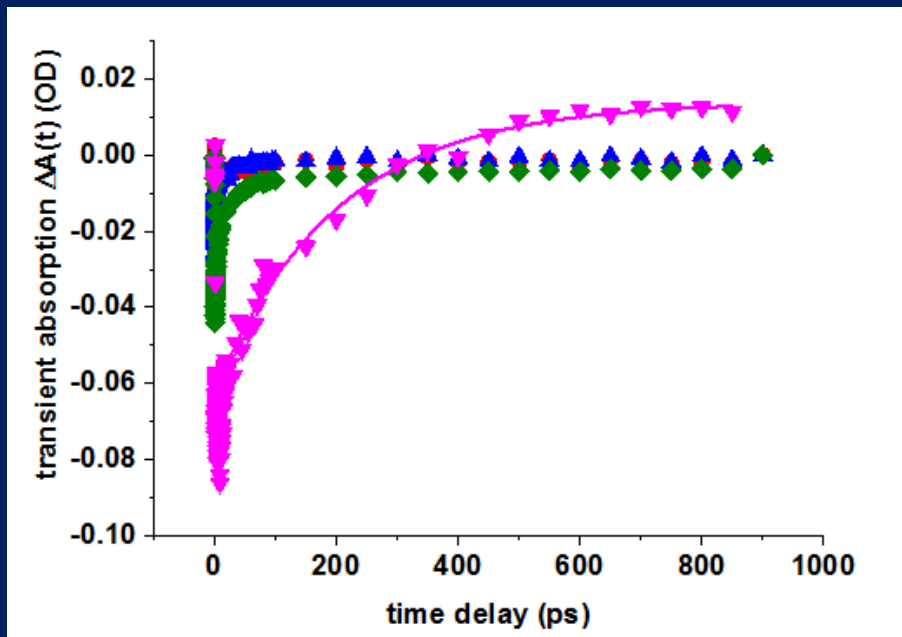
Ultrafast Dynamics of Metal Complexes of Tetrasulphonated Phthalocyanines at biological interfaces of the human tissue



Arkadiusz Jarota, Marc Tondusson, Geoffrey Galle, Eric Freysz, and Halina Abramczyk, 2012

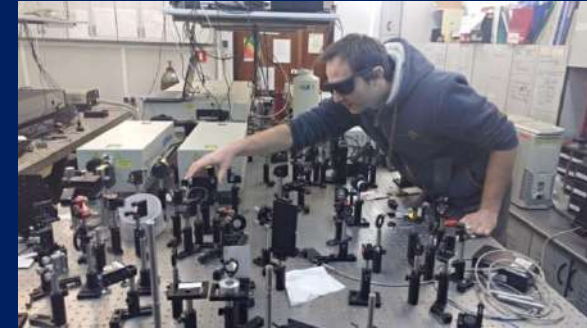
THE JOURNAL OF
PHYSICAL CHEMISTRY A

Femtosecond spectroscopy of human breast tissues with aluminum phthalocyanine



pump 677 nm, probe 670 nm
P58

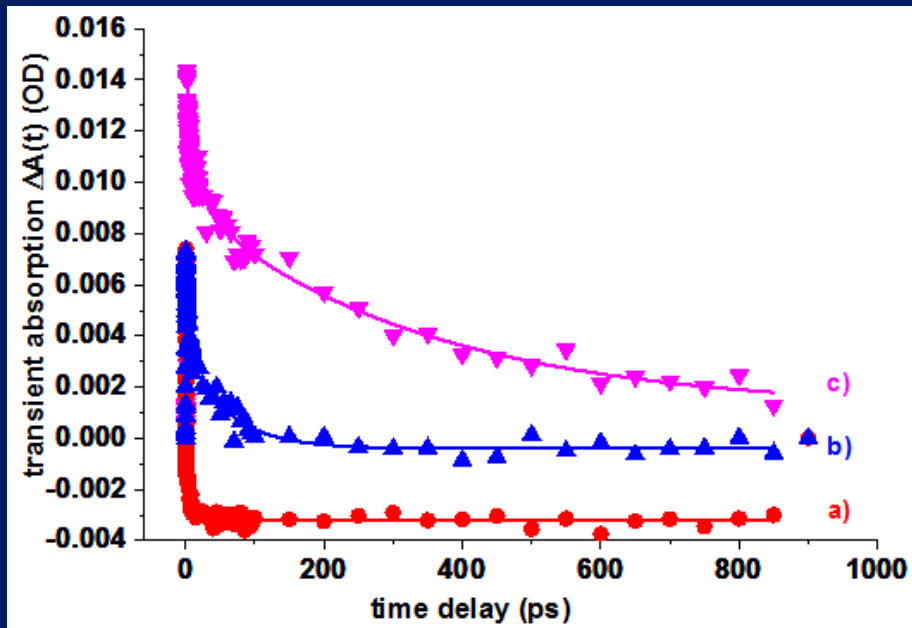
H. Abramczyk, B. Brozek-Pluska, E. Freysz, M. Tondusson,
J. Phys. Chem. C 2013, 113, 4999.



Normal tissue
 130 ± 0.10 fs, 1.53 ± 0.19 ps, i 37.86 ± 5.25 ps
Cancer tissue
 110 ± 0.10 fs, 1.34 ± 0.16 ps, i 40.72 ± 7.86 ps
Film
 830 ± 100 fs, 7.31 ± 1.02 ps, i 56.03 ± 6.58 ps
Solutions
 232.52 ± 81.00 ps, 5.09 ± 0.99 ps



Femtosecond spectroscopy of human breast tissues with aluminum phthalocyanine



Cancer tissue

810 ± 0.04 fs, 5.63 ± 0.49 ps, 59.90 ± 1.85 ps

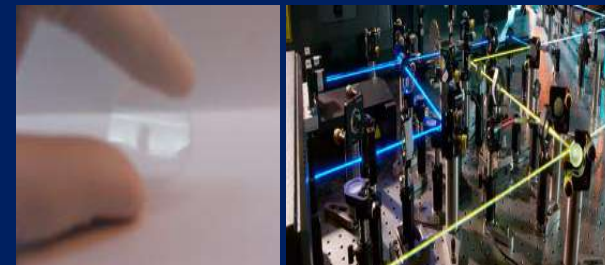
Normal tissue

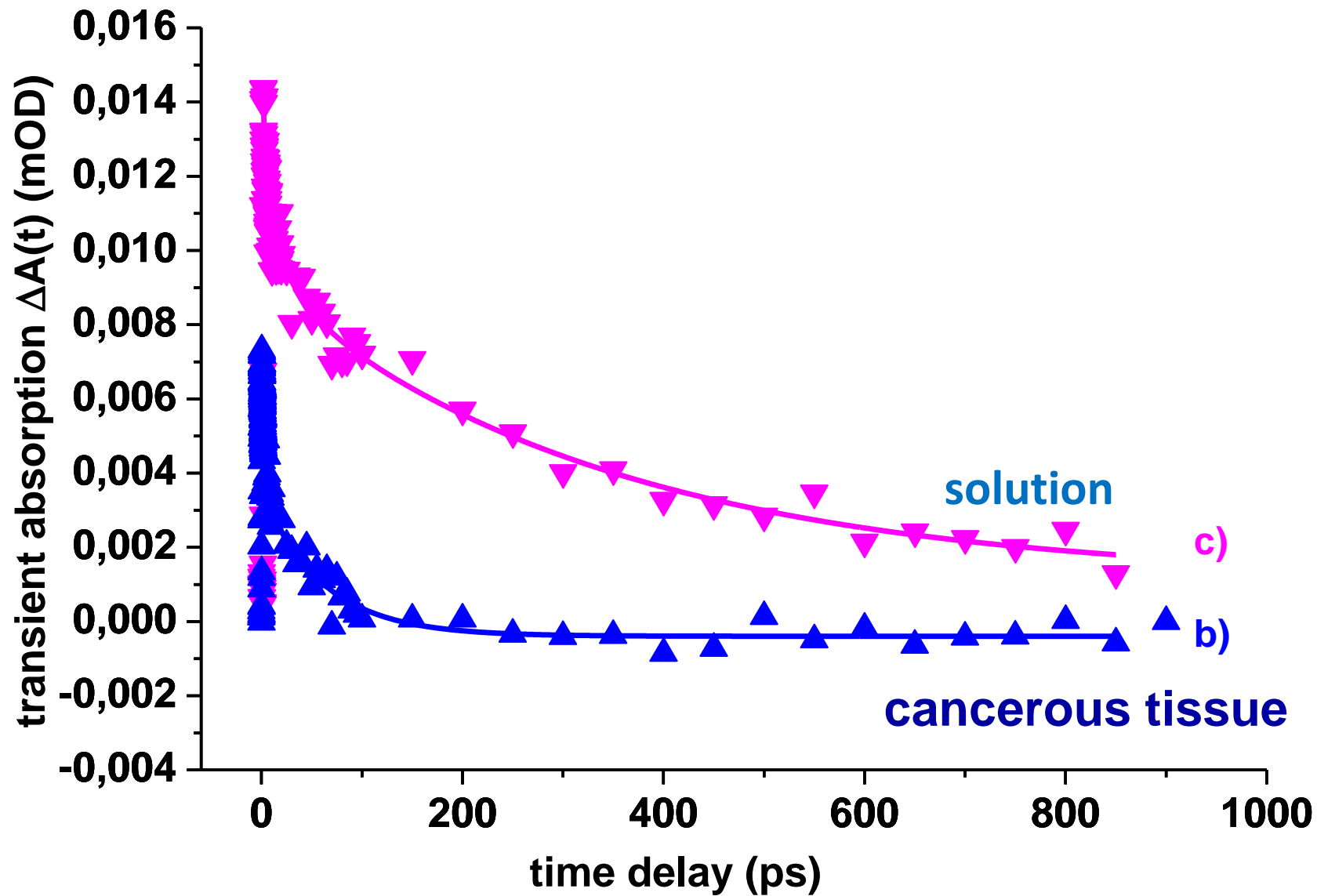
176 ± 0.20 fs, 840 ± 0.42 fs, 6.03 ± 1.92 ps

Solutions

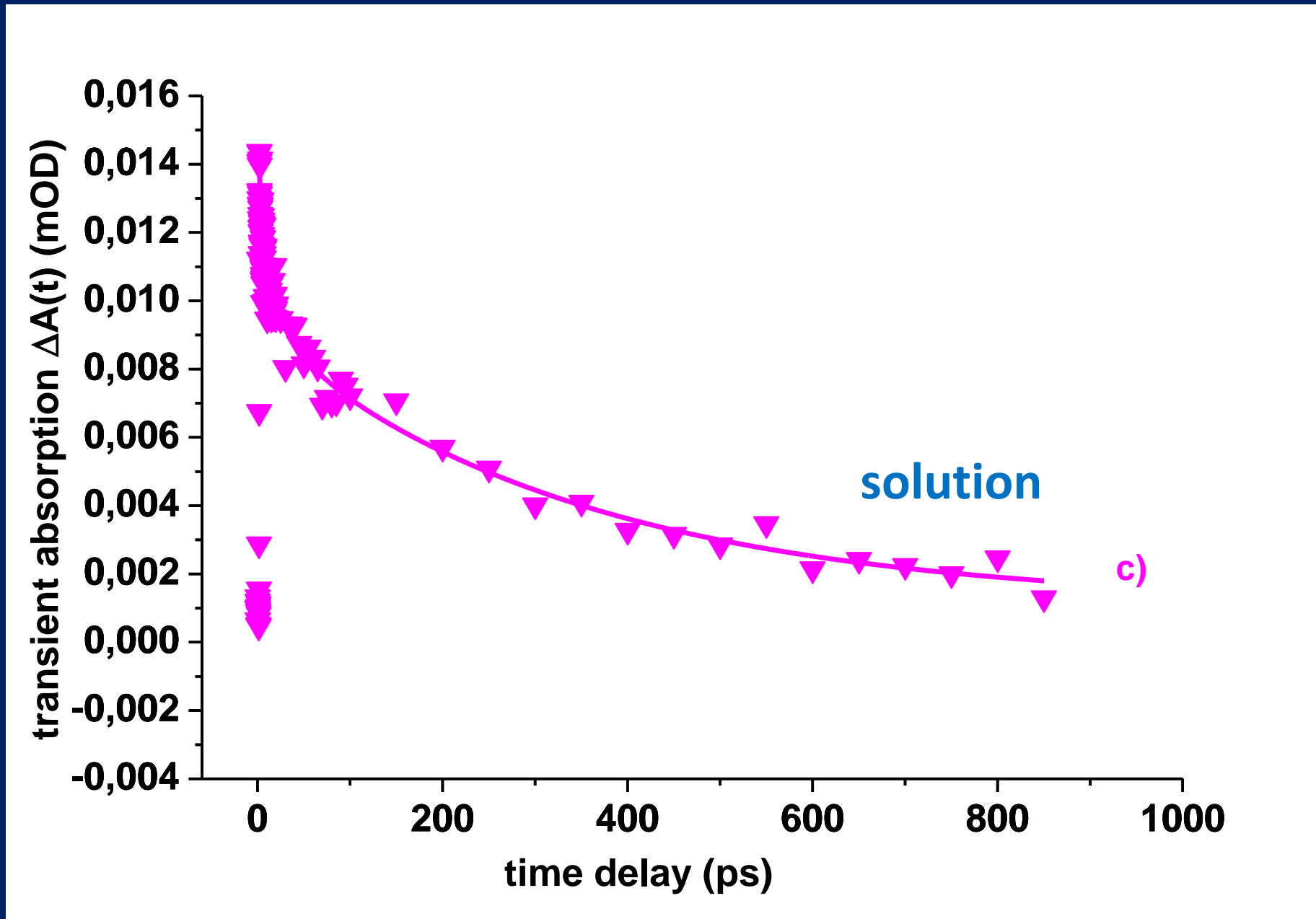
345.81 ± 107.00 ps, 2.37 ± 0.71 ps

pump 677 nm, probe 602 nm
P58

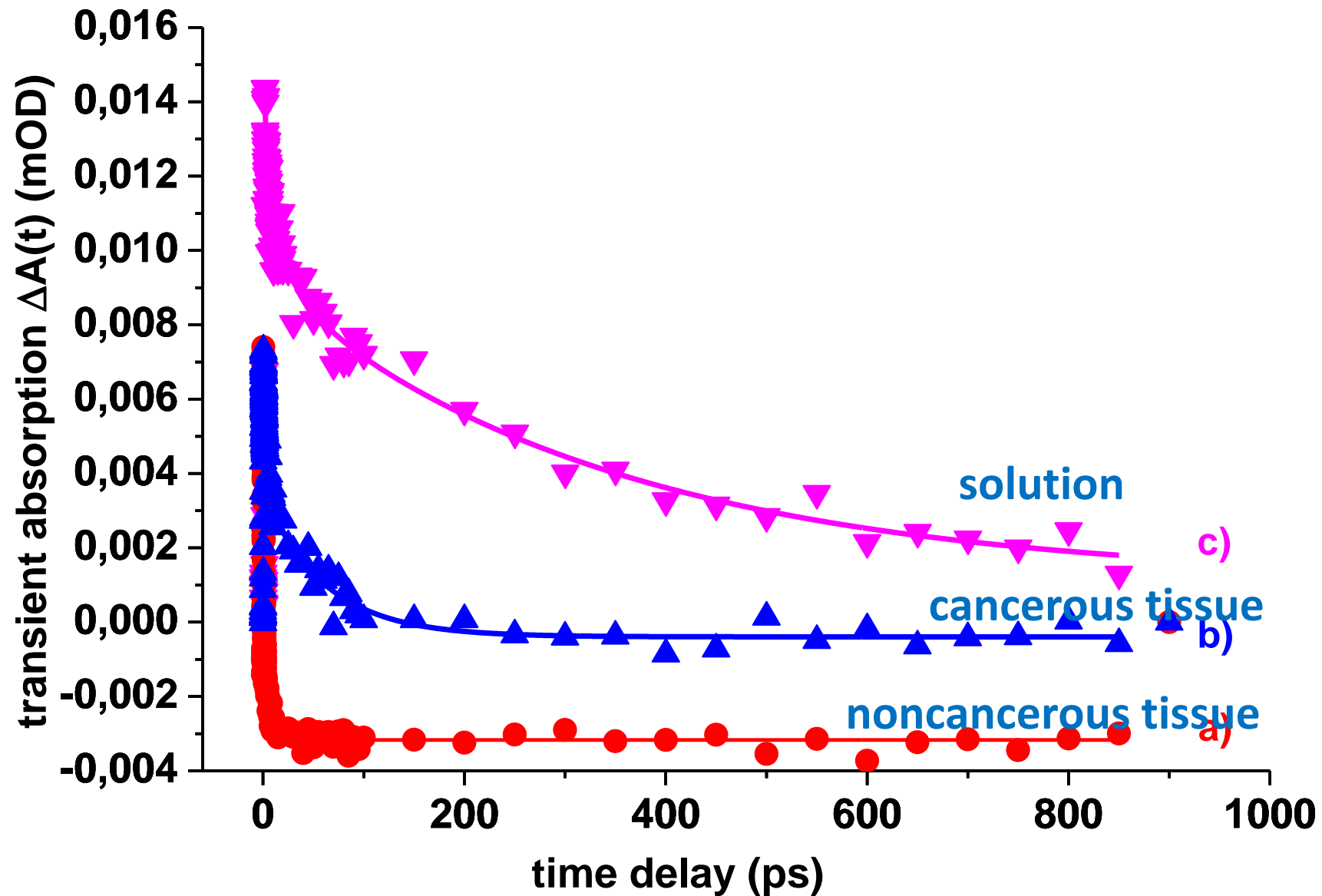




the results showed that the dynamics of the photosensitizer was markedly faster in the interfacial regions of the biological tissue than in solutions. Second, the photosensitizer localized in noncancerous tissue dissipates the energy through different pathways than that in cancerous breast tissue.



the results showed that the dynamics of the photosensitizer was markedly faster in the interfacial regions of the biological tissue than in solutions. Second, the photosensitizer localized in noncancerous tissue dissipates the energy through different pathways than that in cancerous breast tissue.



We have shown that the lifetimes characterizing both the ground state S_0 and the first excited state S_1 in the interfacial regions of noncancerous tissue are markedly shorter than those in cancerous tissue.

CONCLUSIONS

- We showed that Raman measurements of the biochemical mapping of human cancer tissue and cell cultures reveals unique Raman fingerprints that
- discriminate normal and cancer cells
- provide information on cancer phenotype
- monitor epigenetic modifications
- provide information on glycome profile.

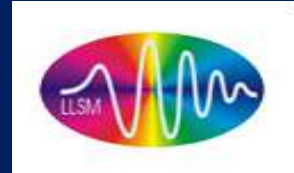
CONCLUSIONS



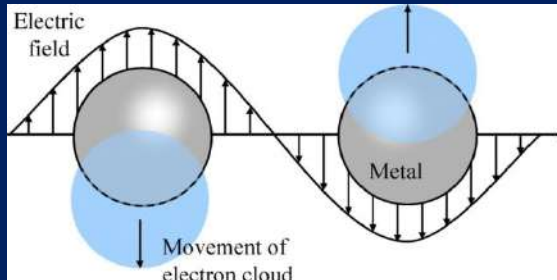
The results presented here demonstrate that Raman spectra and images are sensitive indicators of distribution of different compounds in a normal and cancerous breast tissue, and epithelial cell cultures

- **MORPHOLOGY, BIOCHEMISTRY AND PHOTOCHEMISTRY OF HUMAN TISSUE, AND SINGLE CELLS** to gaining a Practical Understanding of cancer
- Raman spectroscopy and Raman imaging is useful in monitoring epigenetic molecular processes , such as acetylation or methylation in cancer cells.
- Raman results provide strong evidence that the global acetylation level of histone and non-histone proteins increases in human breast cancer cells and is a common hallmark of cancerogenesis.
- the combined Raman/fluorescence imaging exhibits great potential for photodynamic therapy monitoring the distribution of photosensitizers and the biochemical distribution of tissue components.
- The femtosecond dynamics of the photosensitizer can be employed as an important indicator of the cancer pathology

Silver nanoparticles to SERS

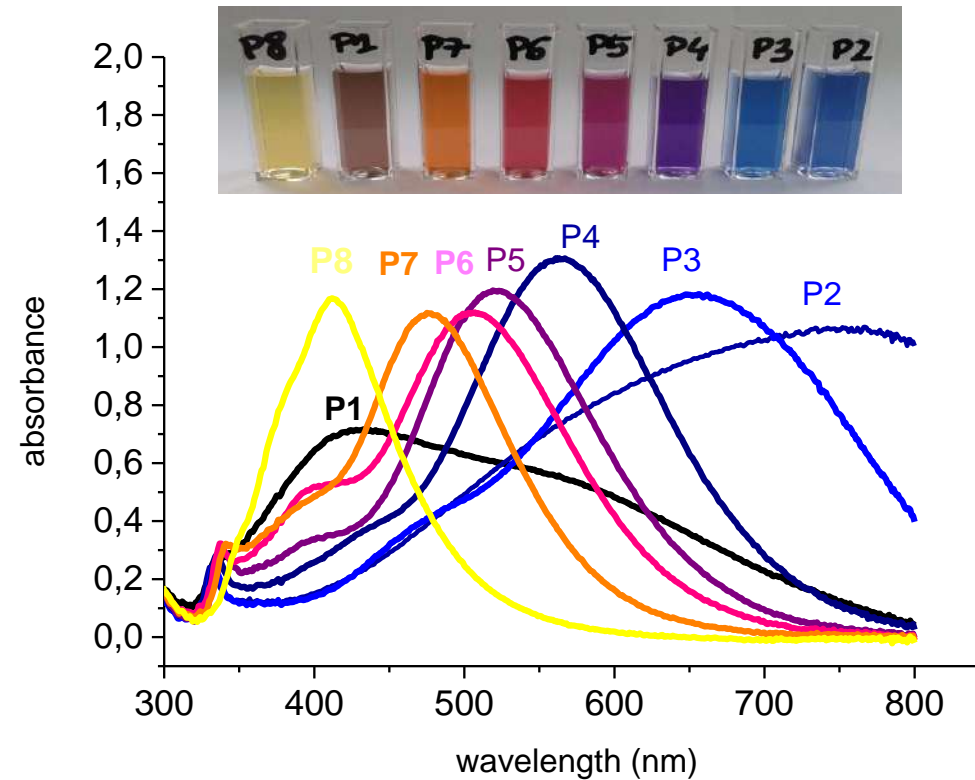


plasmon



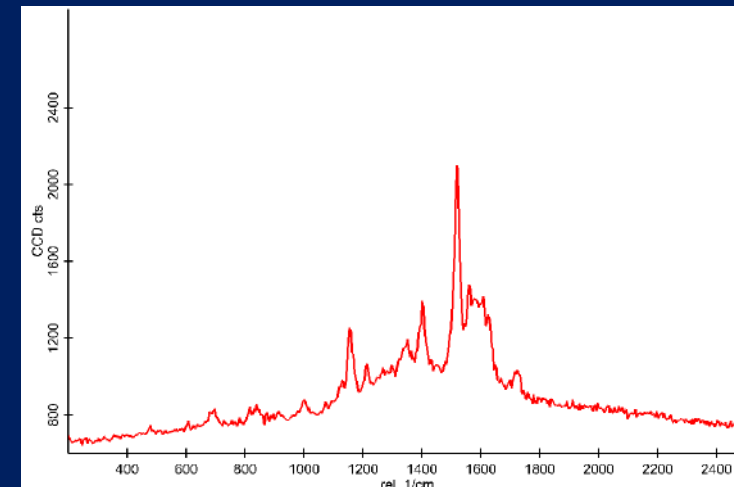
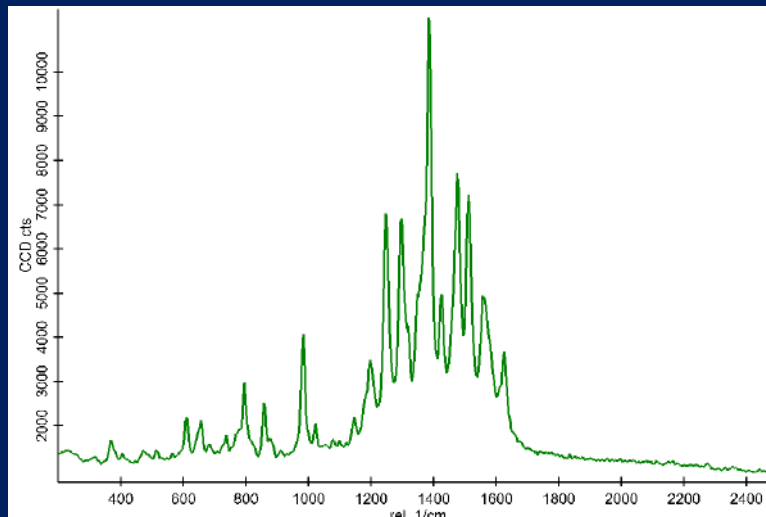
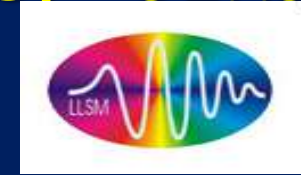
the enhancement mechanism for SERS comes from intense localized fields arising from surface plasmon resonance in metallic (e.g. Ag) nanostructures with sizes of the order of tens of nanometers, a diameter much smaller than the wavelength of the excitation light

Sebastian Schlücker (Ed.): Surface enhanced Raman spectroscopy: analytical, biophysical and life science applications

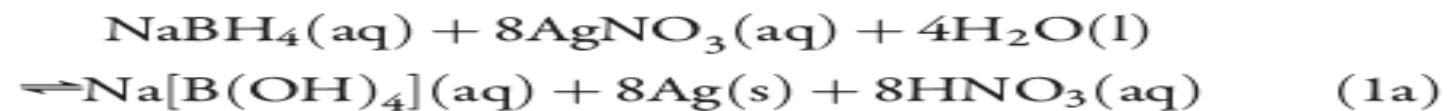


Nanoparticles produced by chemical reduction.

MCF7 cell with silver nanoparticles (PR8) - SERS

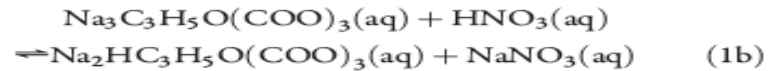


With the method used in this experiment, sodium borohydride is added to reduce silver nitrate:



Sodium citrate -stabilizer – prevents aggregation

As the silver ions are reduced, silver atoms begin to aggregate, forming a well-defined nanoparticle in the presence of surface-stabilizing (capping) and shape- and size-modifying agents. Excess sodium citrate acts as a buffer to maintain neutral or weakly basic pH of the solution by reaction with the nitric acid as it is generated:



In addition to acting as a buffer, sodium citrate charge stabilizes the silver nanoprisms. First, citrate complexes silver, then associates with Ag^+ on a surface of a growing nanoparticle, rendering the surface negatively charged and electrostatically preventing

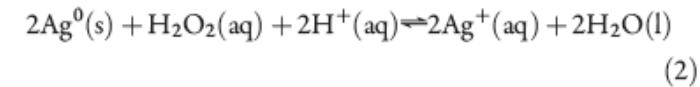
nanoparticles from aggregating. Without proper stabilization, reduction of silver ions leads either to a bulk metal (e.g., the well-known silver mirror reaction(15)) or heavily aggregated nanoparticles (a blackish precipitate). Two other roles attributed to citrate include the complexation of silver ions and possible stabilization of close-packed (111) planes in silver and gold nanostructures.

Potassium bromide KBr Limits the growth of silver nanoparticles

In the approach developed in our laboratory (19), bromide is added to the reaction to alter the size at which the particle stops growing, thus overcoming the limitations of using borohydride for size control. Potassium bromide limits the growth of the silver nanoparticles, leading to smaller sizes of nanoprisms being produced and allowing size control. Bromide is known to strongly bind to the silver surface, forming silver bromide that arrests growth of the silver particle surfaces. This strong binding of bromide ions can be rationalized in terms of the low K_{sp} of silver bromide (5.4×10^{-13}) and that silver nanoparticles always have some Ag^+ on their surface (20). Therefore, using different concentrations of bromide in the reaction media enables variation of the size of silver nanoprisms and, as a result, the colors of their dispersion. Typical UV-vis absorption

Hydrogen peroxide – etching agent to facilitate formation of shaped selected nanoparticles

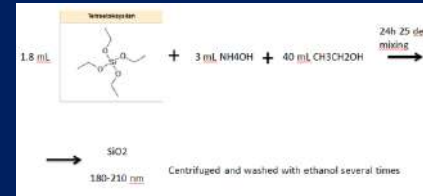
Hydrogen peroxide is employed to facilitate formation of shape-selected nanoparticles. It serves as an etching agent. Less stable newly formed silver nanoparticles are etched by hydrogen peroxide, establishing equilibrium between sodium borohydride reduction and hydrogen peroxide oxidation of silver:



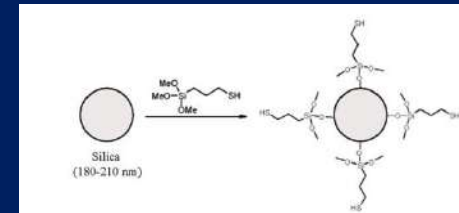
In the absence of peroxide, uncontrolled growth of all the nuclei results in yellow quasi-spherical nanoparticles with large number of structural defects, as commonly observed in most silver nanoparticle formations. Borohydride is an anion, so it reacts with silver cations quickly. On the other hand, hydrogen peroxide molecules are neutral and their reaction with silver nanoparticles is appreciably slower, so larger peroxide concentrations are required. Using peroxide as an etching agent ensures that only the least reactive (or faster growing) of nanoparticle shapes survive and grow at the expense of more reactive shapes (10, 14). Under the conditions outlined in this

SERS nanoparticles

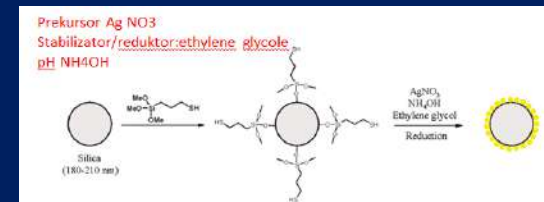
1) preparation of silica nanoparticles



2) functionalization with MPTS 3-mercaptopropyltrimethoxysilane

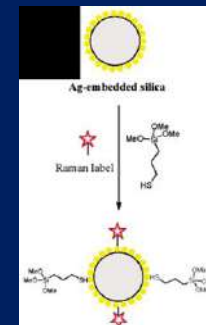


3) preparation of Silver nanoparticles covering silica spheres



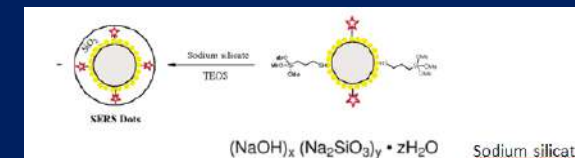
4) Attachment of Raman label

a) Functionalization with MPTS



4-mercaptotoluene (4-MT),
2-naphthalenethiol (2-NT),
thiophenol (TP)

5) These Raman-labeled silica spheres were encapsulated by a silica shell in two steps.



SERS nanoparticles

6) Immobilization of Antibodies on SERS Dots.

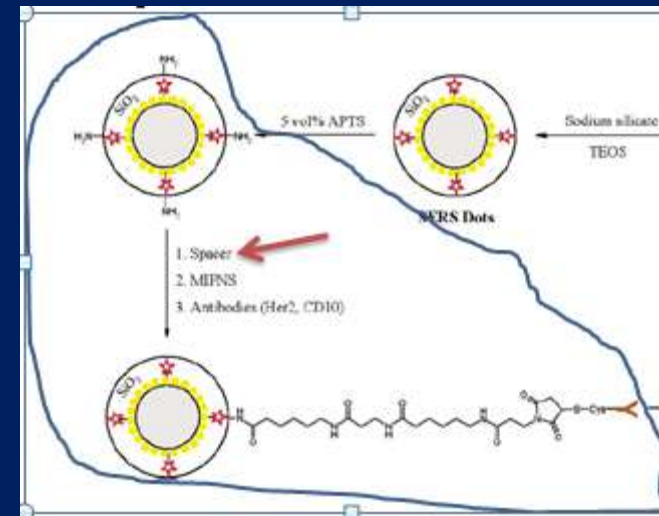
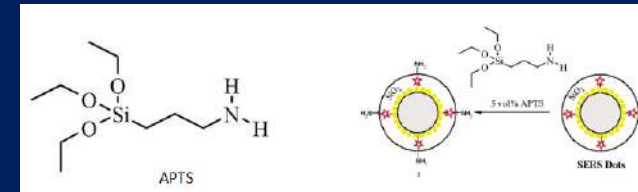
a) A 1-mg portion of SERS dots was added into 1 mL of 3-aminopropyltriethoxysilane (APTS) solution (5 vol % in ethanol), and then 10 *mikro*L of ammonium hydroxide was added.

b) *Spacer* : *N*-(9-fluorenylmethoxycarbonyl)-*-*aminocaproic acid (Fmoc-ACA-OH) was added into the APTS-treated SERS dot dispersion, followed by of (benzotriazol-1-yloxy) tris(dimethylamino) phosphonium hexafluorophosphate (BOP), 1-hydroxybenzotriazole (HOBt), and *N,N*diisopropyl ethylamine (DIEA)

c) After removing the Fmoc protecting group with piperidine, Fmoc-ACA-OH was coupled to amine on SERS dots again by using BOP and HOBt.

d) 3-maleimidopropionic acid N-hydroxysuccinimide ester (MIPNS)

6) Functionalization with antibody



J. Phys. Chem. B **2003**, *107*, 5723-5727

A New Method for Fast Preparation of Highly Surface-Enhanced Raman Scattering (SERS)

Active Silver Colloids at Room Temperature by Reduction of Silver Nitrate with

Hydroxylamine Hydrochloride

Nicolae Leopold^{†,‡} and Bernhard Lendl^{*,‡}

- Lee-Meisel silver colloid, the concentration of silver nitrate in the prepared reaction mixtures was set to 10^{-3} M. The concentration of hydroxylamine hydrochloride was chosen to
- obtain a concentration of $1.5 \cdot 10^{-3}$ M in the final reaction mixture. When using hydroxylamine hydrochloride for reduction of silver nitrate, an initial alkaline pH of the hydroxylamine hydrochloride solution is required. The actual reaction sequence
- that takes place during reduction is complex and involves most likely complex formation between the hydroxylamine and the silver ions, in addition to the observed silver reduction. Gaseous reaction products are observed too. Recently, it has been reported
- that reduction of silver using hydrazine⁵ produces N_2 whereas when studying the oxidation products released upon reduction of iron(III) with hydroxylamine N_2O and again N_2 were found.¹² In our experiments, a decrease in pH was observed, which indicates the release of protons during the reaction. The final pH of the colloidal solution can be adjusted by varying the amount of sodium hydroxide added to the hydroxylamine solution. In the silver sols reported here, a final pH of 7 was measured. The overall reaction was completed within a few seconds in any case with a preparation success rate greater than 90% as revealed by the recorded SERS spectra. **UV-Visible Spectroscopy and Transmission Electron**
- **Microscopy (TEM).** To characterize the morphology of the produced colloids, UV-vis spectroscopy and TEM were used. The absorption maximum of the measured UV-vis spectrum of the colloidal solution provides information on the average particle size, whereas its full width at half-maximum (fwhm) can be used to estimate particle dispersion.¹³ It was found that colloids with different particle size and dispersion could be

Tissue preparation

Frozen Tissue Blocks

Frozen Tissue Arrays

Frozen Tissue Sections

Frozen Tissue Section Panels

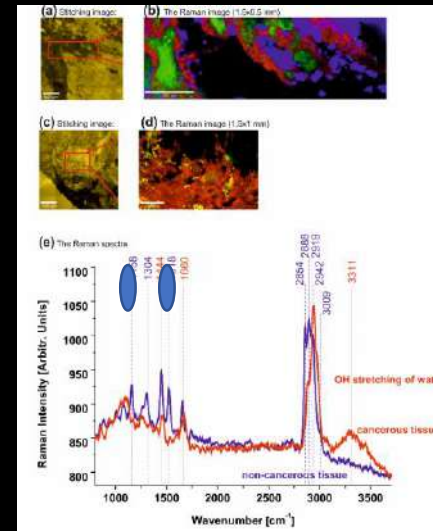
Matched Pair Tissue Frozen Sections

Paraffin Tissue Blocks

Paraffin Tissue Arrays

Paraffin Tissue Sections

Paraffin Tissue Section Panels **deparafinization**



Do not waste valuable information!!!!

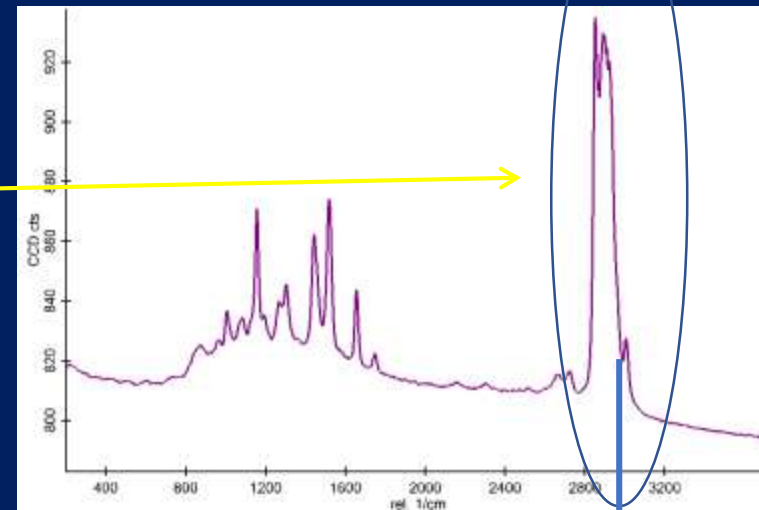
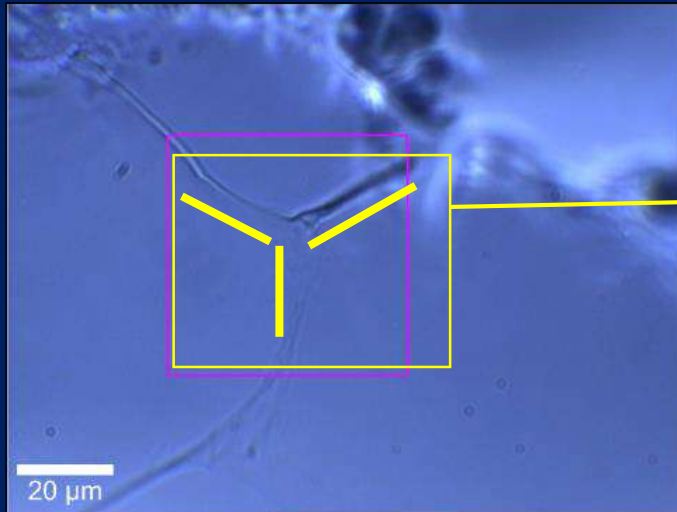
An essential role in spectroscopic methods is played by the preprocessing of tissues, as they naturally occur at the expense of introducing some fixatives, matrices, adhesives, which may generate their own vibrational spectra overlapping the signals from the native tissue. To obtain reliable results one must be sure that the method of tissue processing does not distort the vibrational spectra of the studied tissue.

FRESH TISSUE – the best solution

B. Brozek-Pluska, J. Musial, R. Kordek, E. Bailo, T. Dieing, H. Abramczyk, *Raman spectroscopy and imaging: Applications in human breast cancer diagnosis*. Analyst, 137, 2012, 3773. (IF=4.2)

P80 crio sample

Figure 4 shows the Raman image (a) (150 μm x 100 μm) and the averaged spectra (b). The average spectrum was achieved from the region marked in (a).



P80 Sample after deparafinization

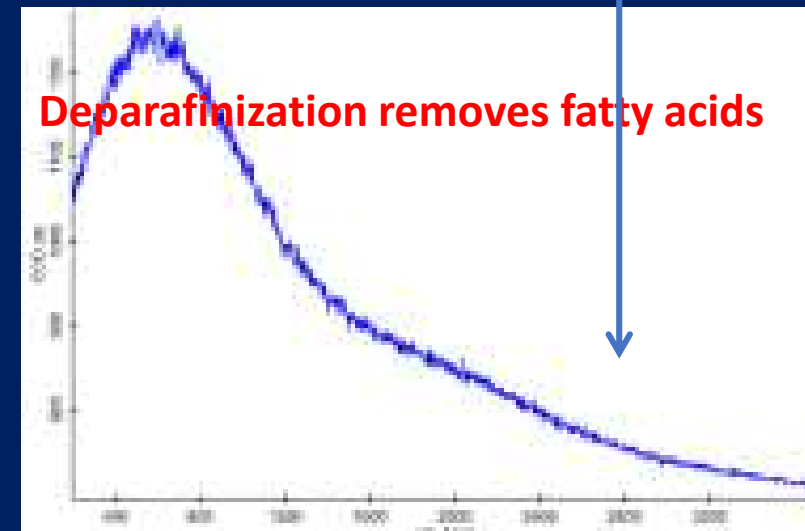
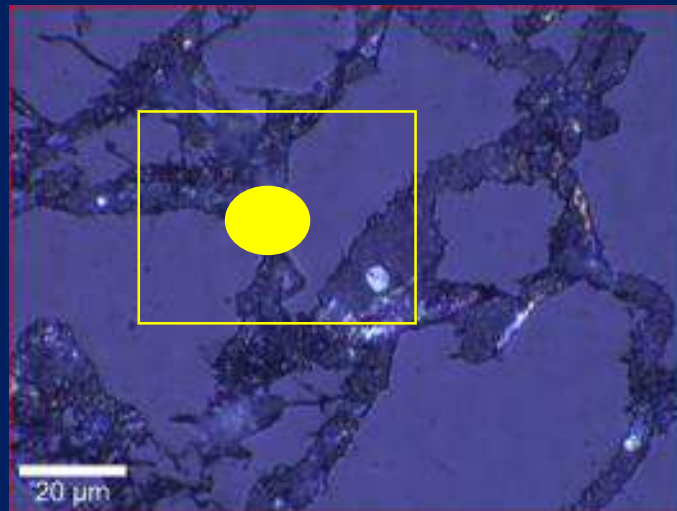
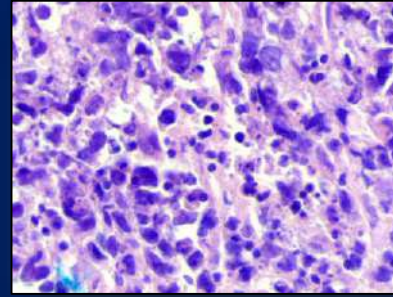


Figure 7 shows the stitching image recorded for a overview of the sample; width [μm]: 150.00 height [μm]: 100.00; objective 5x 0.10NA , the Raman image (b) (x:150 μm ; z:50 μm) objective 50x 0.50NA. (c) The single spectra correspond to the image, the colors of the spectra correspond to the colors in the image; spectra were achieved with a integration time of 0.3 s

The lipid phenotype was ignored for many years by the Raman scientific community that has focused almost exclusively on the biosynthesis of proteins and the proteome profile.

To avoid the proteome pitfalls and to obtain biochemical information in a realistically crowded environment it is necessary to analyze signals from all molecules present in the cells: proteins, fatty acids and lipids, DNA, RNA, saccharides, primary metabolites - which can be obtained only from the fresh tissue

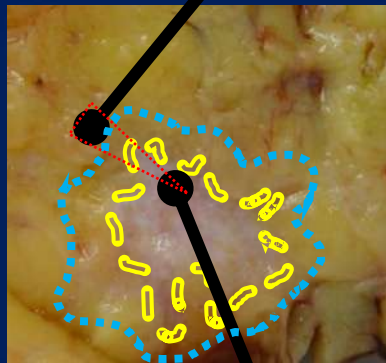
Tissue Preparation



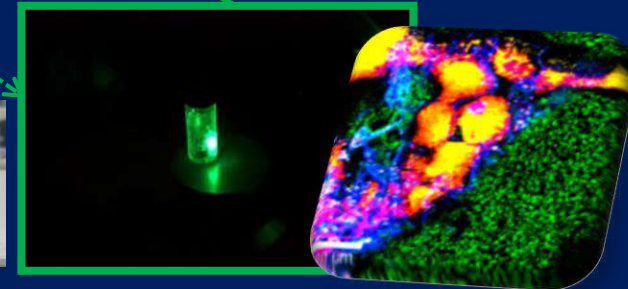
histopathological analysis



healthy tissue

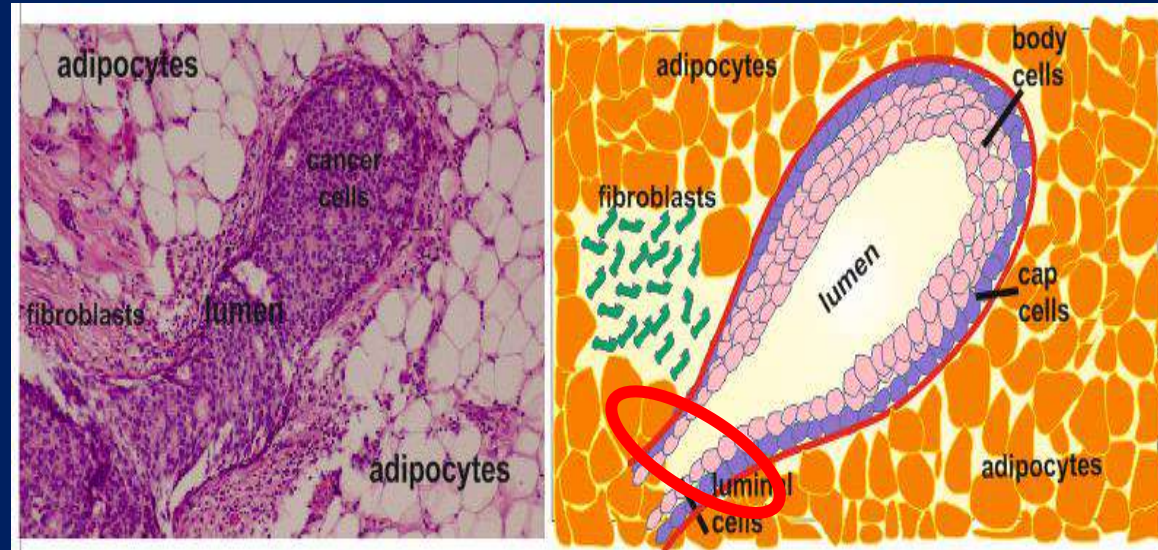
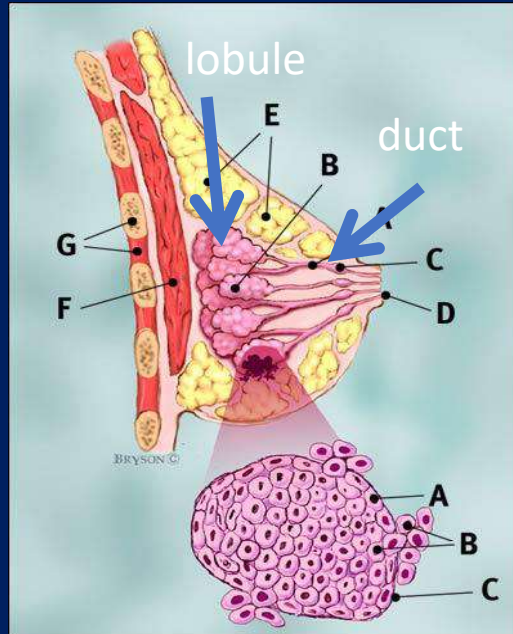


cancerous tissue



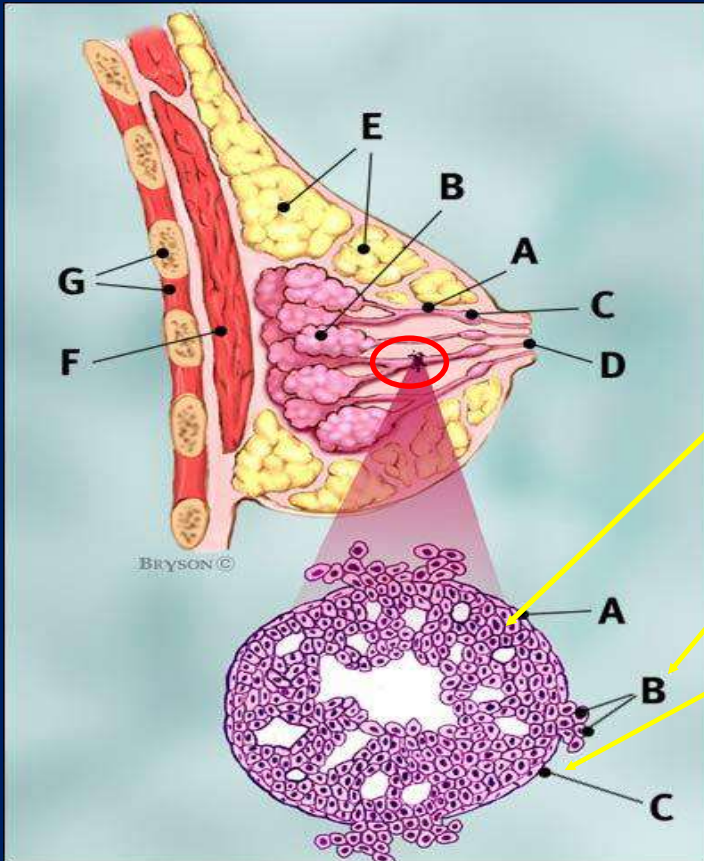
Raman spectroscopy and imaging in LLMS

Breast morphology (P94)



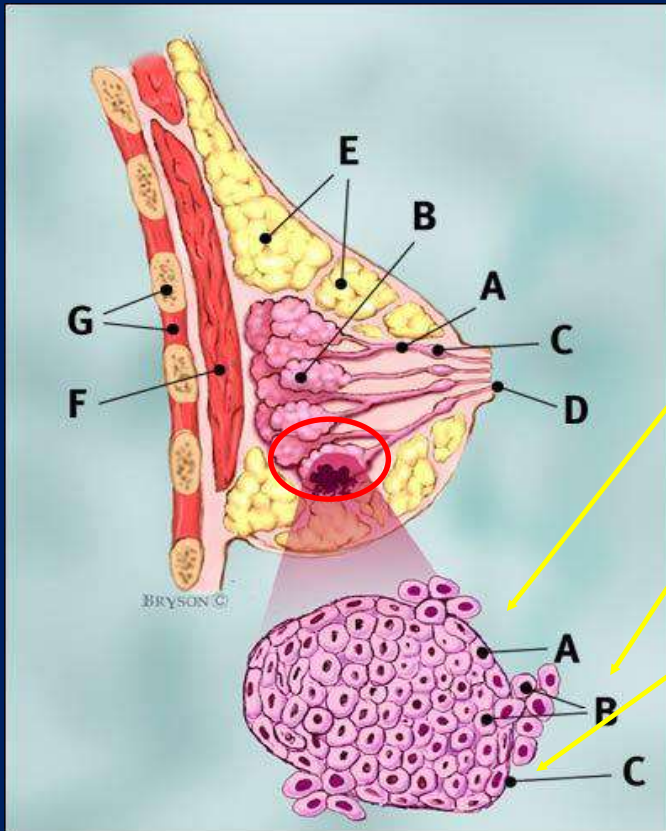
One can see that the cross section through the normal organization of ducts and lobules in the human breast demonstrates luminal epithelial cells aligned in a polar manner so their apical side faces and surrounds the lumen. These cells are surrounded the basement membrane. Fibroblasts align the basement membrane and this entire structure is surrounded by the stroma, which is predominantly, but not exclusively, composed of type I collagen and adipose tissue. During ductal carcinoma in situ (DCIS), the normal polar organization of the luminal epithelial cells is lost, as these cells proliferate. The cross-section shows the epithelial cells completely filling the lumen. In invasive, or infiltrating, carcinoma, the epithelial cells migrate and invade through the basement membrane and into the surrounding stroma.

infiltrating ductal carcinoma (IDC)



- **A** normal duct cells
- **B** ductal cancer cells breaking through the basement membrane
- **C** basement membrane

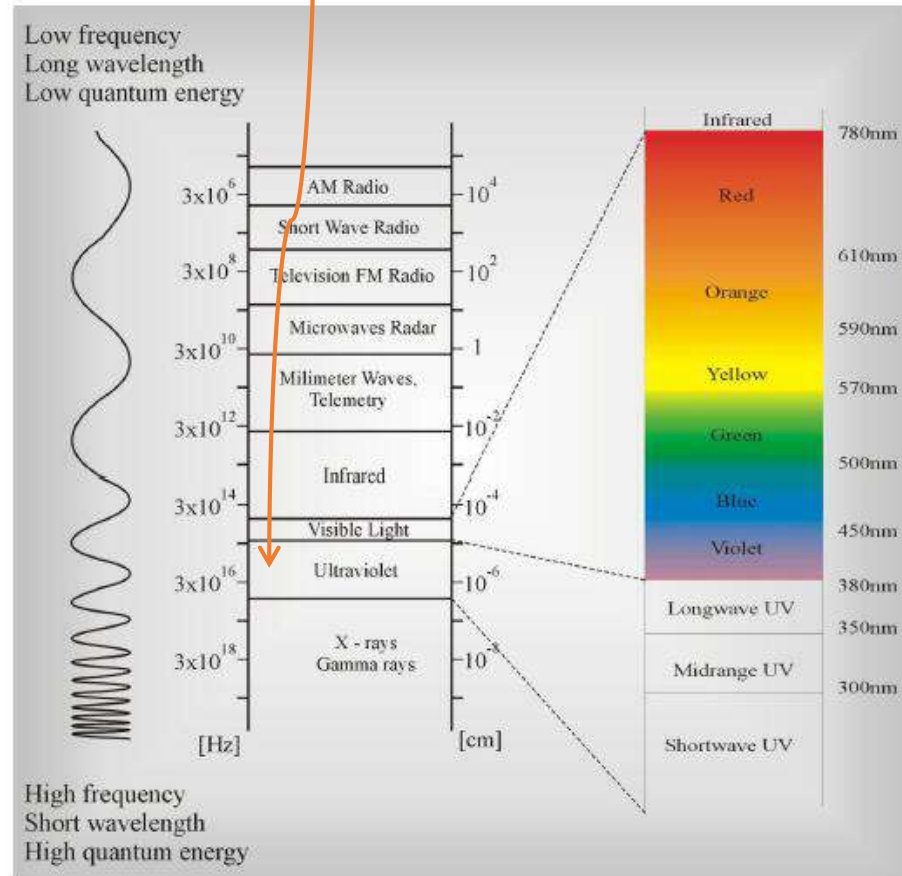
infiltrating lobular carcinoma (ILC)



- A normal cells
- B lobular cancer cells breaking through the basement membrane
- C basement membrane

<http://www.breastcancer.org/pictures/>

VIS-UV spectroscopy electron spectroscopy



Energy levels

n, l, m, s

$$|\vec{l}| = \hbar\sqrt{l(l+1)}$$

$$l \leq n-1$$

$$\mu_e^{\text{orb}} = \sqrt{l(l+1)}\mu_B$$

Bohr magneton



$$\mu_B = \frac{e\hbar}{2m_e c}$$

The projection of the orbital momentum $|\vec{l}|$ on the direction of the electric or magnetic field is $m\hbar$

$$L = \sum \vec{l}_i \quad S = \sum s_i$$

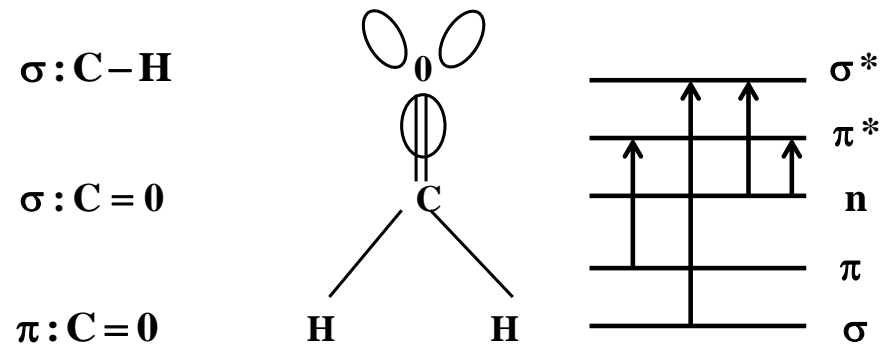
$$2S + 1$$

multiplicities

$S = 0$ $\uparrow\downarrow$ \Rightarrow 1-singlet

$S = \frac{1}{2}$ \uparrow \Rightarrow 2-dublet

$S = 1$ $\uparrow\uparrow$ \Rightarrow 3-triplet



$\sigma \rightarrow \sigma^*$ vacuum ultraviolet (120 nm)

$n \rightarrow \sigma^*$

$\pi \rightarrow \pi^*$

} medium UV

$n \rightarrow \pi^*$ near ultraviolet

Rules of electron spectroscopy

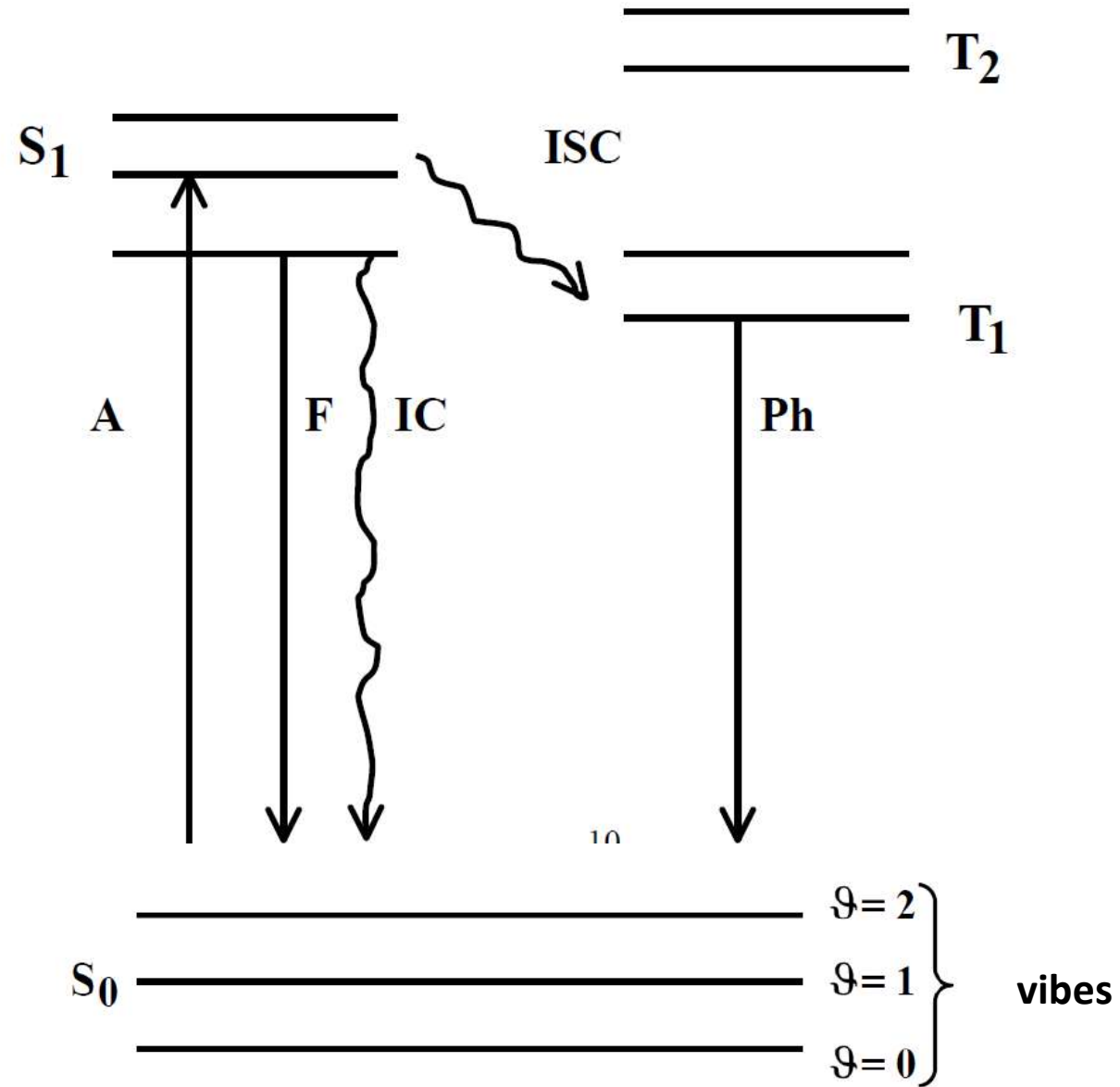
$$\Delta E = h\nu$$

$$\int \Psi_n^* \mu \Psi_k d\tau = \mu_{nk} \neq 0$$

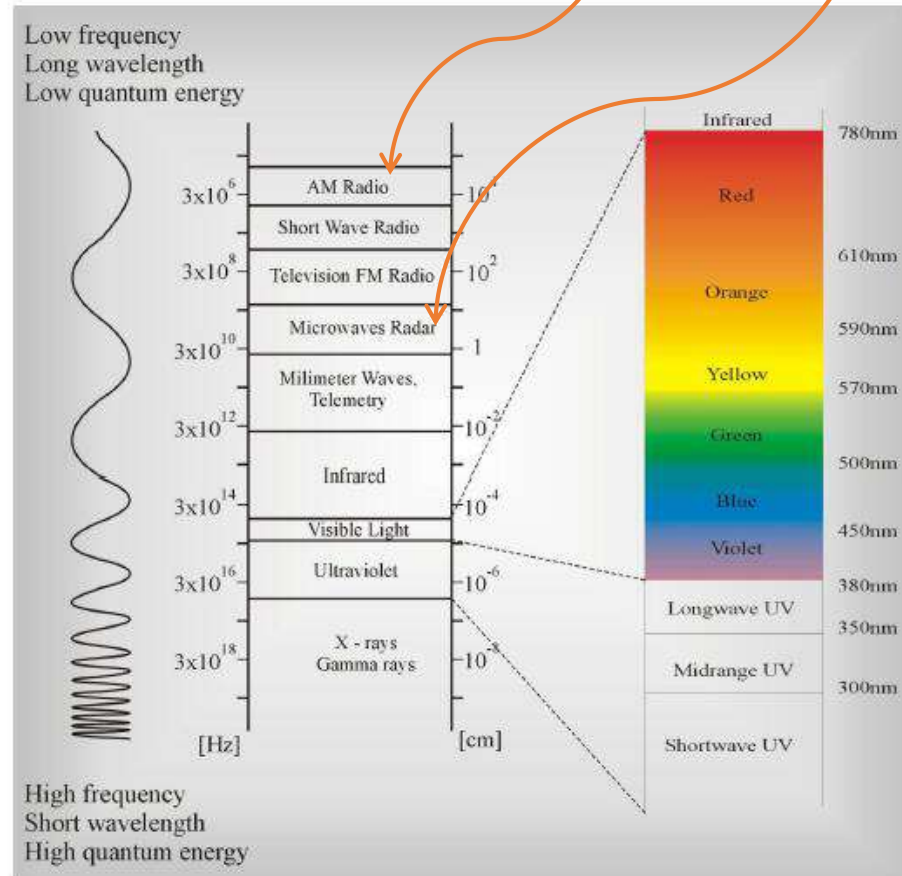
μ_{nk} dipole moment of transition $n \rightarrow k$

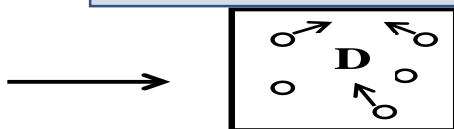
$$\Delta S = 0$$

Jabłoński diagram



NMR and EPR spectroscopy





$$\mathbf{D} = \epsilon \mathbf{E}$$

ϵ - dielectric permittivity

$$\epsilon > 1$$

$$\mathbf{D} > \mathbf{E}$$

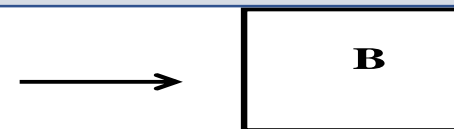
$$\mathbf{D} = \mathbf{E} + 4\pi\mathbf{P}$$

\mathbf{P} - polarization

$$\mathbf{P} = \frac{N\mu^2}{3kT} \mathbf{E} + N\alpha\mathbf{E}$$

α - coefficient of polarization

$$\alpha > 0$$



$$\mathbf{B} = \kappa \mathbf{H}$$

κ - magnetic permeability

$\kappa < 1$ diamagnets

$\kappa > 1$ paramagnetic

$\kappa \gg 1$ ferromagnetic

$$\mathbf{B} = \mathbf{H} + 4\pi\mathbf{M}$$

\mathbf{M} magnetization

$$\mathbf{M} = \frac{N\mu^2}{3kT} \mathbf{H} + N\chi\mathbf{H}$$

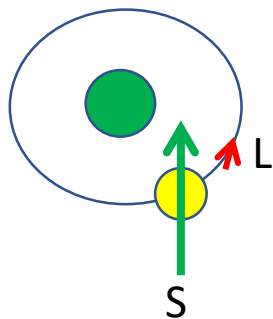
χ - magnetic susceptibility

$$\chi^{\text{or}} = \frac{\mu^2}{3kT} > 0$$

$\chi^{\text{ind}} < 0$ diamagnets

$\chi^{\text{ind}} > 0$ paramagnetic

$\chi^{\text{ind}} \gg 0$ ferromagnetic



EPR

$$\mathbf{L} = \sum \mathbf{L}_i$$

$$\vec{\mathbf{J}} = \vec{\mathbf{L}} + \vec{\mathbf{S}}$$

$\vec{\mathbf{L}}$ - electron orbital moment

$\vec{\mathbf{S}}$ - electron spin

$$m_J = -J, \dots, 0, \dots, +J$$

magnetic quantum number for the electron spin

$$|\vec{\mu}|_J = g \sqrt{J(J+1)} \mu_B$$

magnetic moment

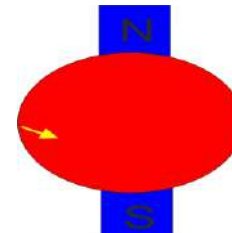
g - magnetogyric coefficient of the electron

μ_B - Bohr magneton

$$\mu_B = \frac{e\hbar}{2m_e c}$$

m_e - mass of the electron

Wartości spinów niektórych jąder - kliknij



$$m_I = -I, \dots, 0, \dots, +I$$

the magnetic quantum number for the spin of the nucleus

$$|\vec{\mu}|_I = \gamma \sqrt{I(I+1)} \mu_N$$

γ - magnetogyric coefficient of the nucleus

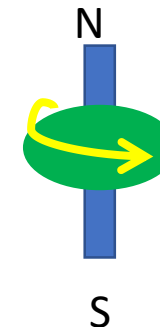
μ_N - nuclear magneton

$$\mu_N = \frac{e\hbar}{2m c}$$

magnetogyric factor

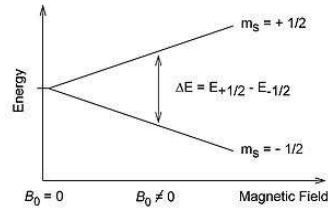
m - mass of the nucleus

$$g = 1 + \frac{J(J+1) + S(S+1) - L(L+1)}{2J(J+1)}$$



Rules in EPR and NMR spectroscopy

The Energy of interaction of the magnetic moment $\vec{\mu}$ with the magnetic induction vector is:



$$\mathbf{E} = - \vec{\mu} \cdot \mathbf{B}$$

$$\mu_{\mathbf{J}} = -g m_{\mathbf{J}} \mu_{\mathbf{B}}$$

$$\mu_{\mathbf{I}} = -\gamma m_{\mathbf{I}} \mu_{\mathbf{N}}$$

The magnetic moment is directed opposite to angular momentum

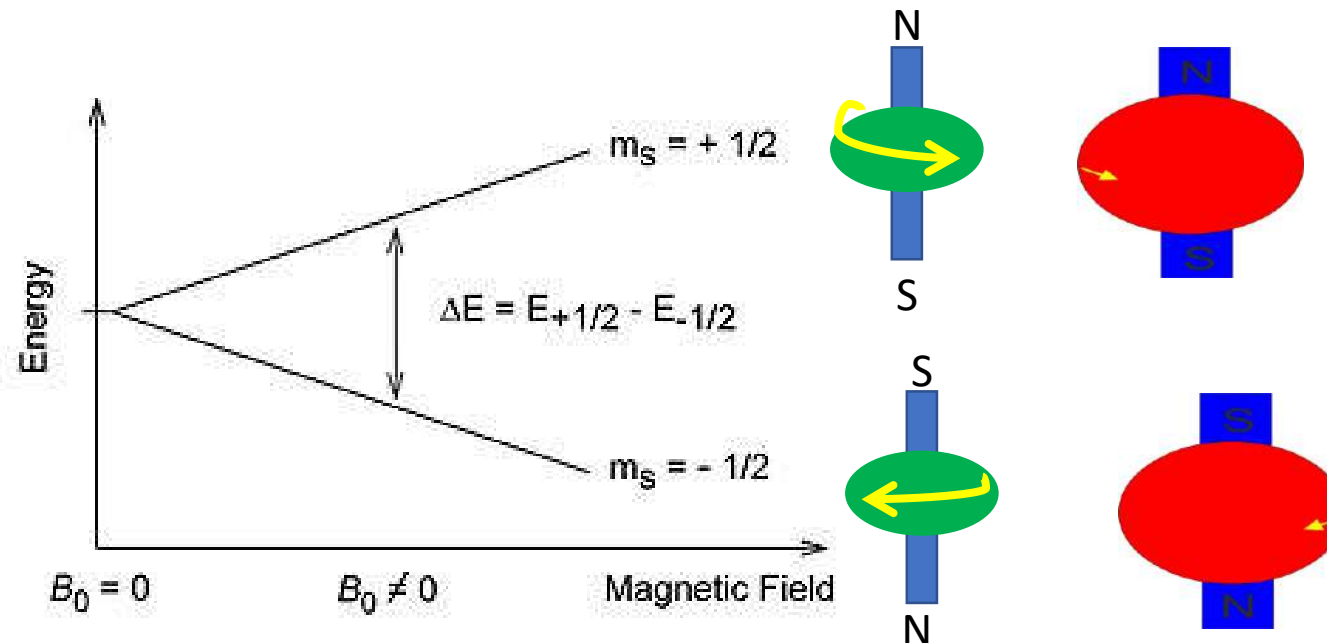
EPR	NMR
$\mathbf{E} = g m_{\mathbf{J}} \mu_{\mathbf{B}} \mathbf{B}$	$\mathbf{E} = \gamma m_{\mathbf{I}} \mu_{\mathbf{N}} \mathbf{B}$
$\left. \begin{aligned} \Delta \mathbf{E} &= g \mu_{\mathbf{B}} \mathbf{B} \\ h\nu &= g \mu_{\mathbf{B}} \mathbf{B} \end{aligned} \right\}$	$\left. \begin{aligned} \Delta \mathbf{E} &= \gamma \mu_{\mathbf{N}} \mathbf{B} \\ h\nu &= \gamma \mu_{\mathbf{N}} \mathbf{B} \end{aligned} \right\}$
$\Delta \mathbf{J} = 1$	$\Delta \mathbf{I} = 1$

The electron has a magnetic moment, because it has a spin with the value $s = 1/2$. The magnetic quantum number m_J assumes the values of $m_s = + 1/2$ and $m_s = -1 / 2$ (because $J = S$). In the presence of the magnetic field $B = B_0$, the magnetic moment is set in parallel ($m_s = -1 / 2$) or antiparallel ($m_s = + 1/2$) to the magnetic field. The energy of the electron in the magnetic field therefore also takes two different values compared to the energy when $B = 0$. The splitting of energy levels is called Zeeman's effects. Parallel spin and B settings have lower energy than antiparallel settings

The Energy difference is:

$$\Delta E = g_e \mu_B B_0$$

where g_e is called the constant g (or the constant Landé or the magnetogyric factor)



Which is the Energy of photons inducting in Epr and NMR?

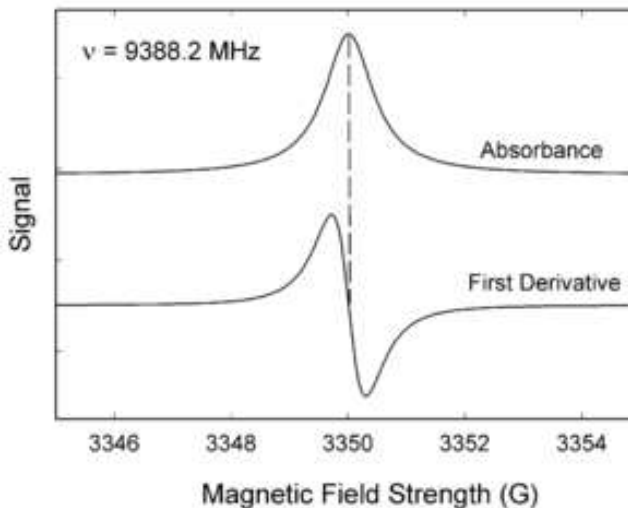
An unpaired electron can move to a lower or higher level by absorbing or emitting electromagnetic radiation with energy $\epsilon = h\nu$, when the condition $\epsilon = h\nu$ is fulfilled

$$\epsilon = \Delta E$$

Substituting $\epsilon = h\nu$ and $\Delta E = g_e \mu_B B_0$ we get

$$h\nu = g_e \mu_B B_0$$

This condition determines what radiation we should use, to fulfill the resonance condition $h\nu = g_e \mu_B B_0$. As you can see, many combinations of frequency and magnetic field can be used, but usually in microwave experiments microwaves in the range 9000-10000 MHz (9-10 GHz) and magnetic field 3500 G (0.35 T) are used.



Boltzmann's distribution describes the method of planting energy states by atoms, molecules and other chemical entities in a state of thermal equilibrium.

If you want to know more, click here Boltzmann's distribution the method of planting Energy states by atoms, molecules

[ROZKŁAD
BOLTZMANN – WYKŁAD 6](#)

Boltzmann distribution

EPR

$$\frac{n_w}{n_n} = e^{-\left(\frac{\Delta E}{kT}\right)} = e^{-\left(\frac{g\mu_B B}{kT}\right)}$$

NMR

$$\frac{n_w}{n_n} = e^{-\left(\frac{\gamma\mu_N B}{kT}\right)}$$

n_w number of molecules at a higher level

n_n number of molecules at a lower level